

# Synthesis, Characterization, Properties, and Applications of Nanosized Ferroelectric, Ferromagnetic, or Multiferroic Materials

Guest Editors: Debasis Dhak, Seungbum Hong, Soma Das, and Prasanta Dhak





---

**Synthesis, Characterization, Properties,  
and Applications of Nanosized Ferroelectric,  
Ferromagnetic, or Multiferroic Materials**

Journal of Nanomaterials

---

**Synthesis, Characterization, Properties,  
and Applications of Nanosized Ferroelectric,  
Ferromagnetic, or Multiferroic Materials**

Guest Editors: Debasis Dhak, Seungbum Hong, Soma Das,  
and Prasanta Dhak



---

Copyright © 2015 Hindawi Publishing Corporation. All rights reserved.

This is a special issue published in "Journal of Nanomaterials." All articles are open access articles distributed under the Creative Commons Attribution License, which permits unrestricted use, distribution, and reproduction in any medium, provided the original work is properly cited.

## Editorial Board

Domenico Acierno, Italy  
Katerina Aifantis, USA  
Sheikh Akbar, USA  
Nageh K. Allam, USA  
Margarida Amaral, Portugal  
Jordi Arbiol, Spain  
Raul Arenal, Spain  
Ilaria Armentano, Italy  
Lavinia Balan, France  
Thierry Baron, France  
Andrew R. Barron, USA  
Hongbin Bei, USA  
Stefano Bellucci, Italy  
Enrico Bergamaschi, Italy  
D. Bhattacharyya, New Zealand  
Giovanni Bongiovanni, Italy  
Theodorian Borca-Tasciuc, USA  
Mohamed Bououdina, Bahrain  
Torsten Brezesinski, Germany  
C. Jeffrey Brinker, USA  
Christian Brosseau, France  
Yibing Cai, China  
Chuanbao Cao, China  
Victor M. Castao, Mexico  
Albano Cavaleiro, Portugal  
Bhanu P. S. Chauhan, USA  
Wei Chen, China  
Tupei Chen, Singapore  
Yuan Chen, Singapore  
Shafiul Chowdhury, USA  
Kwang-Leong Choy, UK  
Jin-Ho Choy, Korea  
Yu-Lun Chueh, Taiwan  
Elisabetta Comini, Italy  
Giuseppe Compagnini, Italy  
David Cornu, France  
Miguel A. Correa-Duarte, Spain  
P. Davide Cozzoli, Italy  
Majid Darroudi, Iran  
Shadi A. Dayeh, USA  
Luca Deseri, USA  
Yong Ding, USA  
Bin Dong, China  
Zehra Durmus, Turkey  
Joydeep Dutta, Oman

Ali Eftekhari, USA  
Samy El-Shall, USA  
Farid El-Tantawy, Egypt  
Ovidiu Ersen, France  
Claude Estourns, France  
Andrea Falqui, Saudi Arabia  
Xiaosheng Fang, China  
Bo Feng, China  
Matteo Ferroni, Italy  
Wolfgang Fritzsche, Germany  
Alan Fuchs, USA  
Peng Gao, China  
Miguel A. Garcia, Spain  
Siddhartha Ghosh, Singapore  
P. K. Giri, India  
Russell E. Gorga, USA  
Jihua Gou, USA  
Alexander Govorov, USA  
Jean M. Greneche, France  
Changzhi Gu, China  
Lin Guo, China  
John Z. Guo, USA  
Smrati Gupta, Germany  
Kimberly Hamad-Schifferli, USA  
Michael Harris, USA  
Jr-Hau He, Taiwan  
Nguyen D. Hoa, Vietnam  
Michael Z. Hu, USA  
Qing Huang, China  
Nay Ming Huang, Malaysia  
Shaoming Huang, China  
David Hui, USA  
Zafar Iqbal, USA  
Balachandran Jeyadevan, Japan  
Xin Jiang, Germany  
Rakesh Joshi, Australia  
Myung-Hwa Jung, Korea  
Jeong-won Kang, Korea  
Hassan Karimi-Maleh, Iran  
Antonios Kelarakis, UK  
Alireza Khataee, Iran  
Ali Khorsand Zak, Iran  
Dojin Kim, Korea  
Wonbaek Kim, Korea  
Jang-Kyo Kim, Hong Kong

Philippe Knauth, France  
Ralph Krupke, Germany  
Christian Kübel, Germany  
Sanjeev Kumar, India  
Sushil Kumar, India  
Prashant Kumar, UK  
Subrata Kundu, India  
Michele Laus, Italy  
Eric Le Bourhis, France  
Burtrand Lee, USA  
Jun Li, Singapore  
Meiyong Liao, Japan  
Silvia Licoccia, Italy  
Wei Lin, USA  
Jun Liu, USA  
Zainovia Lockman, Malaysia  
Songwei Lu, USA  
Jue Lu, USA  
Ed Ma, USA  
Malik Maaza, South Africa  
Lutz Mädler, Germany  
Gaurav Mago, USA  
Morteza Mahmoudi, Iran  
Mohammad A. Malik, UK  
Devanesan Mangalaraj, India  
Sanjay R. Mathur, Germany  
Paulo Cesar Morais, Brazil  
Mahendra A. More, India  
Paul Munroe, Australia  
Jae-Min Myoung, Korea  
Rajesh Naik, USA  
Albert Nasibulin, Russia  
Toshiaki Natsuki, Japan  
Koichi Niihara, Japan  
Sherine Obare, USA  
Won-Chun Oh, Republic of Korea  
Atsuto Okamoto, Japan  
Abdelwahab Omri, Canada  
Ungyu Paik, Republic of Korea  
Edward A. Payzant, USA  
Ton Peijs, UK  
Oscar Perales-Prez, Puerto Rico  
Wenxiu Que, China  
Peter Reiss, France  
Orlando Rojas, USA



---

Marco Rossi, Italy  
Cengiz S. Ozkan, USA  
Vladimir Šepelák, Germany  
Huaiyu Shao, Japan  
Prashant Sharma, USA  
Donglu Shi, USA  
Bhanu P. Singh, India  
Surinder Singh, USA  
Vladimir Sivakov, Germany  
Yanlin Song, China  
Ashok Sood, USA  
Marinella Striccoli, Italy  
Jing Sun, China  
Xuping Sun, Saudi Arabia  
Ashok K. Sundramoorthy, USA

Sabine Szunerits, France  
Nyan-Hwa Tai, Taiwan  
Bo Tan, Canada  
Ion Tiginyanu, Moldova  
Valeri P. Tolstoy, Russia  
Muhammet S. Toprak, Sweden  
Ramon Torrecillas, Spain  
Takuya Tsuzuki, Australia  
Tamer Uyar, Turkey  
Bala Vaidhyanathan, UK  
Luca Valentini, Italy  
Rajender S. Varma, USA  
Antonio Villaverde, Spain  
Ajayan Vinu, Australia  
Shiren Wang, USA

Yong Wang, USA  
Ruibing Wang, Macau  
Magnus Willander, Sweden  
Ping Xiao, UK  
Zhi Li Xiao, USA  
Yangchuan Xing, USA  
Doron Yadlovker, Israel  
Piaoping Yang, China  
Yoke K. Yap, USA  
Ramin Yousefi, Iran  
Kui Yu, Canada  
William W. Yu, USA  
Renyun Zhang, Sweden

## Contents

**Synthesis, Characterization, Properties, and Applications of Nanosized Ferroelectric, Ferromagnetic, or Multiferroic Materials**, Debasis Dhak, Seungbum Hong, Soma Das, and Prasanta Dhak  
Volume 2015, Article ID 723145, 2 pages

**Characterization of Multiferroic Domain Structures in Multiferroic Oxides**, Lizhi Liang, Heng Wu, Lei Li, and Xinhua Zhu  
Volume 2015, Article ID 169874, 8 pages

**Ferroelectric and Dielectric Properties of  $\text{ZnFe}_2\text{O}_4$ - $\text{Pb}(\text{ZrTi})\text{O}_3$  Multiferroic Nanocomposites**, Shrabanee Sen, Sk. Md. Mursalin, and M. Maharajan  
Volume 2015, Article ID 526249, 5 pages

**Growth of  $\text{BiFeO}_3$  Microcylinders under a Hydrothermal Condition**, L. J. Di, H. Yang, T. Xian, J. Y. Ma, H. M. Zhang, J. L. Jiang, Z. Q. Wei, and W. J. Feng  
Volume 2015, Article ID 175605, 5 pages

**Fabrication, Characterization, Properties, and Applications of Low-Dimensional  $\text{BiFeO}_3$  Nanostructures**, Heng Wu, Jun Zhou, Lizhi Liang, Lei Li, and Xinhua Zhu  
Volume 2014, Article ID 471485, 14 pages

**Enhanced Magnetization of Sol-Gel Synthesized Pb-Doped Strontium Hexaferrites Nanocrystallites at Low Temperature**, Shahid M. Ramay, Shahid Atiq, Murtaza Saleem, Asif Mahmood, Saadat A. Siddiqi, Shahzad Naseem, Yousef Al-Zeghayer, Nasser S. Alzayed, and Mohammed Shahabuddin  
Volume 2014, Article ID 452468, 7 pages

## Editorial

# Synthesis, Characterization, Properties, and Applications of Nanosized Ferroelectric, Ferromagnetic, or Multiferroic Materials

Debasis Dhak,<sup>1</sup> Seungbum Hong,<sup>2</sup> Soma Das,<sup>3</sup> and Prasanta Dhak<sup>4</sup>

<sup>1</sup>Department of Chemistry, Sidho-Kanho-Birsha University, Purulia, West Bengal 723101, India

<sup>2</sup>Materials Science Division, Argonne National Laboratory, Lemont, IL 60439, USA

<sup>3</sup>Electronics & Communication Engineering, Institute of Technology, Guru Ghasidas Vishwavidyalaya, Bilaspur 495009, India

<sup>4</sup>Department of Materials Science and Engineering, Seoul National University, Seoul 151-744, Republic of Korea

Correspondence should be addressed to Debasis Dhak; [debasisdhak@yahoo.co.in](mailto:debasisdhak@yahoo.co.in)

Received 28 December 2014; Accepted 28 December 2014

Copyright © 2015 Debasis Dhak et al. This is an open access article distributed under the Creative Commons Attribution License, which permits unrestricted use, distribution, and reproduction in any medium, provided the original work is properly cited.

Recently, there has been an enormous increase in research activity in the field of ferroelectrics and ferromagnetics especially in multiferroic materials which possess both ferroelectric and ferromagnetic properties simultaneously. However, the ferroelectric, ferromagnetic, and multiferroic properties should be further improved from the utilitarian and commercial viewpoints.

Nanostructural materials are central to the evolution of future electronics and information technologies. Ferroelectrics and ferromagnetics have already been established as a dominant branch in electronics sector because of their diverse applications. The ongoing dimensional downscaling of materials to allow packing of increased numbers of components into integrated circuits provides the momentum for evolution of nanostructural devices. Nanoscaling of the above materials can result in a modification of their functionality. Furthermore, nanoscaling can be used to form high density arrays of nanodomain nanostructures, which is desirable for miniaturization of devices.

In the paper “Characterization of Multiferroic Domain Structures in Multiferroic Oxides,” L. Liang et al. have reviewed the recent progress in the characterizations of multiferroic domain structures in multiferroic oxides. Due to the existence of two or three primary ferroic order parameters simultaneously in the same phase multiferroics and intricately coupling each other, new amazing multiferroic properties and/or phenomena are realized by combinations of distinct nanometer-scale charge-ordered domains,

cloverleaf domain structures, and topological defects such as multiferroic vortex-antivortex pairs. Recent development of spherical aberration correction is revolutionizing the performance of HRTEM/STEM instruments, which allows one to achieve a spatial resolution better than 0.08 nm and an energy resolution better than 100 MeV. Such breakthrough would bring us to see and thoroughly explore the multiferroic domain structures at subangstrom scale.

In the paper “Enhanced Magnetization of Sol-Gel Synthesized Pb-Doped Strontium Hexaferrites Nanocrystallites at Low Temperature,” S. M. Ramay et al. have shown the influence of Pb doping on the structural and low temperature magnetic behavior of  $\text{SrPb}_x\text{Fe}_{12-x}\text{O}_{19}$ . Saturation magnetization was found to decrease while coercivity was increased with the increase of Pb contents in the series at 300 K. When temperature was reduced to 200 K, the saturation magnetization of the relevant samples was increased, credited to the preferred individual spin alignments at low temperature. Remanence was also decreased but the corresponding effect was less prominent as the  $M_r/M_s$  and consequently the energy product were found to increase, corroborating the use of these ferrite compositions where hard magnetic characteristics are required.

In the paper “Fabrication, Characterization, Properties, and Applications of Low-Dimensional  $\text{BiFeO}_3$  Nanostructures,” H. Wu et al. also have reviewed the recent research progress of low-dimensional BFO nanostructures, including their fabrication, property, structural characterization, and

applications. Perovskite-type BFO as one of the few known single-phase multiferroics possesses ferroelectricity and anti-ferromagnetism at room temperature. Its low-dimensional nanostructures are much attractive in the applications of multistate storage, magnetoelectric sensor, and spintronic devices.

In the paper “Ferroelectric and Dielectric Properties of  $\text{ZnFe}_2\text{O}_4\text{-Pb}(\text{ZrTi})\text{O}_3$  Multiferroic Nanocomposites,” S. Sen et al. have synthesized  $\text{ZnFe}_2\text{O}_4\text{-Pb}(\text{ZrTi})\text{O}_3$  by sol-gel technique and have characterized them by XRD, TEM, and SEM for structural and microstructural analysis. The dielectric constant along with the P-E hysteresis loops was also studied for the mentioned samples.

In the paper “Growth of  $\text{BiFeO}_3$  Microcylinders under a Hydrothermal Condition,” L. J. Di et al. demonstrated the hydrothermal synthesis of cylinder-like BFO microcylinders, size of which is dependent on hydrothermal reaction time. Photocatalytic experimental results demonstrate that the BFO microcylinders exhibit an appreciable photocatalytic activity toward the degradation of “acid orange 7” under simulated sunlight irradiation. Magnetic hysteresis loop measurement reveals an antiferromagnetic behavior in the  $\text{BiFeO}_3$  microcylinders at room temperature.

As the sizes of the microelectronics enter into nanoscale, there are still some problems that need to be solved in fabrication, characterization, and application of  $\text{BiFeO}_3$  and other low-dimensional nanostructures. For instance, in BFO nanostructures there exists quantum size effect (ferroelectric and magnetoelectric), size effect, and surface/interface effect; all these effects must be considered together from experimental and theoretical researches, which are the fundamental to develop the new generation of revolutionary electronic nanodevices. Although the BFO has good ferroelectricity, its weak ferromagnetism is highly required to be enhanced, which could be achieved in low-dimensional nanostructures. Therefore, deeper understanding of the fundamentals of the low-dimensional nanostructures with the development of advanced technology and exploring the coexistence of ferroelectricity and ferromagnetism with strong coupling between them will be the future direction of multiferroic nanomaterials researches.

Another fascinating task is to combine the measurements of multiferroic physical properties (e.g., ferroelectric, magnetic, and magnetoelectric coupling properties) with the multiferroic domain analysis as focused on here in this special issue. This type of simultaneous measurements will be necessary for further understanding of the ferroelectric, magnetic, and/or magnetoelectric coupling between the small domains. An exciting new era for multiferroic domain characterizations in multiferroic oxides is on the horizon.

In summary, as reflected by its content this special issue provides a broad panorama for research in this specific field and will benefit the readers, especially those working in this field.

## Acknowledgments

We would like to thank our reviewers for their time and comments and thank the authors for their contributions to this

special issue. This special issue could not have been successful without their contribution and support. The work at Argonne (Seungbum Hong was responsible for paper writing) was supported by the US Department of Energy, Office of Science, Materials Sciences and Engineering Division.

*Debasis Dhak  
Seungbum Hong  
Soma Das  
Prasanta Dhak*

## Review Article

# Characterization of Multiferroic Domain Structures in Multiferroic Oxides

Lizhi Liang, Heng Wu, Lei Li, and Xinhua Zhu

National Laboratory of Solid State Microstructures, School of Physics, Nanjing University, Nanjing 210093, China

Correspondence should be addressed to Xinhua Zhu; xhzhu1967@aliyun.com

Received 25 April 2014; Accepted 27 September 2014

Academic Editor: Debasis Dhak

Copyright © 2015 Lizhi Liang et al. This is an open access article distributed under the Creative Commons Attribution License, which permits unrestricted use, distribution, and reproduction in any medium, provided the original work is properly cited.

Multiferroic oxides have been received much attention due to that these materials exhibit multiple ferroic order parameters (e.g., electric polarization in ferroelectrics, magnetization in ferromagnetics, or spontaneous strain in ferroelastics) simultaneously in the same phase in a certain temperature range, which offer an exciting way of coupling between the ferroic order parameters. Thus, this provides a possibility for constructing new type of multifunctional devices. The multiferroic domain structures in these materials are considered to be an important factor to improve the efficiency and performance of future multiferroic devices. Therefore, the domain structures in multiferroic oxides are widely investigated. Recent developments in domain characterization techniques, particularly the aberration-corrected transmission electron microscopy (TEM), have enabled us to determine the domain structures at subangstrom scale, and the recent development of *in situ* TEM techniques allows ones to study the dynamic behaviors of multiferroic domains under applied fields or stress while the atomic structure is imaged directly. This paper provides a review of recent advances on the characterization of multiferroic domain structures in multiferroic oxides, which have been achieved by the notable advancement of aberration-corrected TEM.

## 1. Introduction

In recent years multiferroic materials have attracted much interest because they possess more than one type of ferroic order parameters in the same phase, which brings out novel physical phenomena and offers the possibilities for developing new multiferroic devices [1–3]. The defining characteristic of a ferroic material is ferroic order parameter (e.g., electric polarization in ferroelectrics, magnetization in ferromagnets, or spontaneous strain in ferroelastics) that has different, energetically equivalent orientations; the orientation of which can be selected using an applied field. For example, in the magnetoelectric multiferroics there exists a coupling between the electric and magnetic fields, or named as magnetoelectric effect, which describes the induction of magnetization ( $M$ ) by an electric field ( $E$ ) or polarization ( $P$ ) generated by a magnetic field ( $H$ ). The multiferroic materials may have domains with differently oriented regions, separated by domain walls, coexisting in a sample. In the magnetoelectric multiferroics, both ferroelectric and magnetic domains exist simultaneously. In addition,

“ferroelectric domain switching controlled by magnetic field” and “magnetic domain switching controlled by electric field” are also available, which lead to the possibilities for designing new multiferroic devices [4]. In the multiferroic oxides, the possible domain structures are much more complex than that in either ferroelectric or ferroelastic materials due to the multiple coupling between the primary ferroic order parameters. Aizu [5] analyzed the numbers of ferroic domain states in multiferroics, and found that the possible domain walls, was given by the ratio of the point group orders of the high- and low-symmetry phases, although Shuvalov et al. [6] argued that a higher number of domains (super-orientational states) could be permissible than given by the Aizu rule, as indeed observed in ferroelastic  $\text{YBa}_2\text{Cu}_3\text{O}_{7-\delta}$  [7]. The multiferroic domain structures in these multiferroic oxides are considered to be important factors to improve the efficiency and performance of future magnetoelectric devices. Therefore, multiferroic domain structures in multiferroic oxides have been extensively investigated. Meanwhile, both the techniques and instruments of transmission electron microscopy (TEM), which is one of the most powerful

tools of the domain analysis, have been much improved in the last decade. As advances in aberration-corrected TEM have enabled ones to determine three-dimensional structures of materials with subangstrom resolution, the recent development of *in situ* TEM techniques also allows ones to study the dynamic behaviors of multiferroic domains under applied fields or stress while the atomic structure is directly imaged simultaneously [8–10]. Therefore, the new generation high-resolution TEM (HRTEM) and scanning transmission electron microscopy (STEM) facilities equipped with Cs-corrector will benefit for the characterizations of multiferroic domain structures in multiferroic oxides. Recently, much progress in this direction has been achieved by the notable advancement of aberration-corrected TEM. In this paper, an overview of the characterizations of multiferroic domain structures in multiferroic oxides is presented, and the future challenges of the characterizations on the domain structures of multiferroic oxides are also discussed.

## 2. Multiferroic Domain Structures in Multiferroic Oxides

Multiferroic oxides can be classified four categories based on their different microscopic nature for multiferroic behaviors [1]. The first type is lone pair multiferroics (examples such as BiFeO<sub>3</sub>, BiMnO<sub>3</sub>, and PbVO<sub>3</sub>, in which the A-site cation (Bi<sup>3+</sup>, Pb<sup>2+</sup>) has a stereochemically active 6s<sup>2</sup> lone-pair electrons, distorting the geometry of the BO<sub>3</sub> anion, resulting in ferroelectricity); the second one is charge-ordered multiferroics (certain “noncentrosymmetric” arrangements of ions induce ferroelectricity in magnetic materials, one prominent example is LuFe<sub>2</sub>O<sub>4</sub>); the third one is magnetic-ordered multiferroics (as exemplified in DyMnO<sub>3</sub>, TbMnO<sub>3</sub>, and TbMn<sub>2</sub>O<sub>4</sub>, ferroelectricity is induced by magnetic long-range order in which the arrangement of magnetic dipoles lacks reflection symmetry); and the fourth one is geometrical frustration multiferroics (as exemplified in REMnO<sub>3</sub> (RE = Y, Dy, Tb, etc.), in which long-range dipole-dipole interactions and rotations of oxygen atoms generate a stable ferroelectric state). In multiferroics, the possible domain structures are much more complex than that in either ferroelectric or ferroelastic materials due to the multiple coupling between the primary ferroic order parameters. In this work, we will focus on the multiferroic domain structures in multiferroics revealed by TEM and aberration-corrected HRTEM/STEM.

*2.1. Multiferroic Domain Structures in BiFeO<sub>3</sub> Thin Films.* Perovskite-type BiFeO<sub>3</sub>, as one of the few known single-phase magnetoelectric multiferroics, exhibits a coexistence of simultaneous ferroelectric and magnetic order parameters above room temperature. Thus, it offers exciting potential for room temperature device integration and has been the topic of intensive studies as an interesting model multiferroics [11]. Structurally, BiFeO<sub>3</sub> crystallizes in a rhombohedrally distorted perovskite structure with *R3c* space group at room temperature, of which the lattice constants were determined as  $a_h = 5.587 \text{ \AA}$ ,  $c_h = 13.867 \text{ \AA}$  in the hexagonal unit cell containing six formula or  $a_R = 5.638 \text{ \AA}$ ,  $\alpha = 59.348^\circ$  in

the rhombohedral unit cell containing two formula units [11]. Three main distortions are responsible for the existence of spontaneous polarization along the  $[001]_{\text{hex}}$  direction (i.e.,  $[111]_{\text{cub}}$ ). Therefore, in the BiFeO<sub>3</sub> with a rhombohedral structure, there exists eight different polar domains, and three possible types of ferroelectric domain walls, namely as 71°, 109°, and 180° domain walls. Recently, a new kind of vortex-like nanodomain arrays (toroidal domain patterns) were reported in the epitaxial BiFeO<sub>3</sub> thin films grown on TbScO<sub>3</sub> substrates, which were revealed by aberration-corrected STEM [12]. Figure 1(a) is dark-field TEM image of the vortex nanodomain arrays formed at the interface between the BiFeO<sub>3</sub> film and TbScO<sub>3</sub> substrate, and Figure 1(b) is the plotting of the  $D_{\text{FB}}$  vectors ( $D_{\text{FB}}$  defined as the atomic displacement in the image plane of the Fe cation from the center of the unit cell formed by its four Bi neighbors) for a 109° domain wall which forms a vortex domain by addition of a pair of 180° triangle domains, where the polarization rotates about the intersection of two 109° and two 180° domain walls to form a vortex domain structure. The formation of such complex domain structures tends to reduce the depolarization fields produced at the surface of the TbScO<sub>3</sub> insulator substrates. And along with the interface epitaxy constraints, a local broadening of the walls is produced, which makes the polarization rotation quasicontinuous.

*2.2. Multiferroic Domain Structures in Hexagonal YMnO<sub>3</sub> Single Crystals.* Hexagonal YMnO<sub>3</sub> is the representative geometrical frustrated multiferroics, which has received much attention not only from a fundamental but also a technological point of view because of its large coupling between the two (magnetic and electric) ferroic orders. The magnetic and electric coupling can be utilized for higher density data storage or highly sensitive sensor devices. The ferroelectric and magnetic domain structures in this multiferroic material are considered to be an important factor for improving the efficiency and performance of future multiferroic devices. Therefore, multiferroic domain structures in multiferroic hexagonal YMnO<sub>3</sub> are extremely studied. In the past years, domain structures in YMnO<sub>3</sub> have been studied by various methods, such as surface etching [13], SEM [13], second-harmonic near-field imaging [14], piezo-response force microscopy [15, 16], and conventional TEM [17, 18]. In recent years, a characteristic cloverleaf domain structure and topologically protected multiferroic vortex-antivortex pairs have been revealed by conventional dark-field TEM images [19, 20], as shown in Figure 2. Figure 2(a) shows a combination of dark-field TEM image (bottom grey-scale layer) and conductive atomic force microscopy (top colored layer) image of cloverleaf domain pattern, which shows six crystallographic domains joining at a defect line with positive and negative polarization (+ and – signs in the conductive atomic force microscopy image, resp.) alternating around the defect. The TEM dark-field image was obtained by using the  $1\bar{3}1$  diffraction spot (the Miller index is based on P63cm), in which six antiphase domains ( $\alpha$ - $\beta$ - $\gamma$ - $\alpha$ - $\beta$ - $\gamma$ ) form 60° wedges and merge from one central point. These six structural domains represent the minima of free energy of

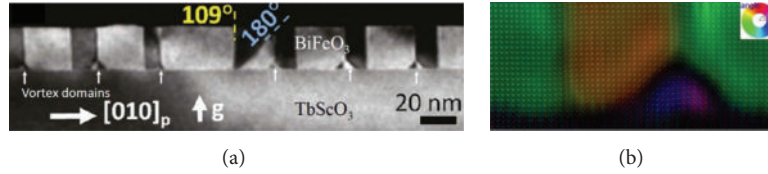


FIGURE 1: (a) Dark-field TEM images of the vortex nanodomain arrays formed at the interface between the  $\text{BiFeO}_3$  film and  $\text{TbScO}_3$  substrate. (b) Plotting of the  $D_{\text{FB}}$  vectors (defined as the atomic displacement in the image plane of the Fe cation from the center of the unit cell formed by its four Bi neighbors) for a  $109^\circ$  domain wall which forms a vortex domain by addition of a pair of  $180^\circ$  triangle domains, where the polarization rotates about the intersection of two  $109^\circ$  and two  $180^\circ$  domain walls [12].

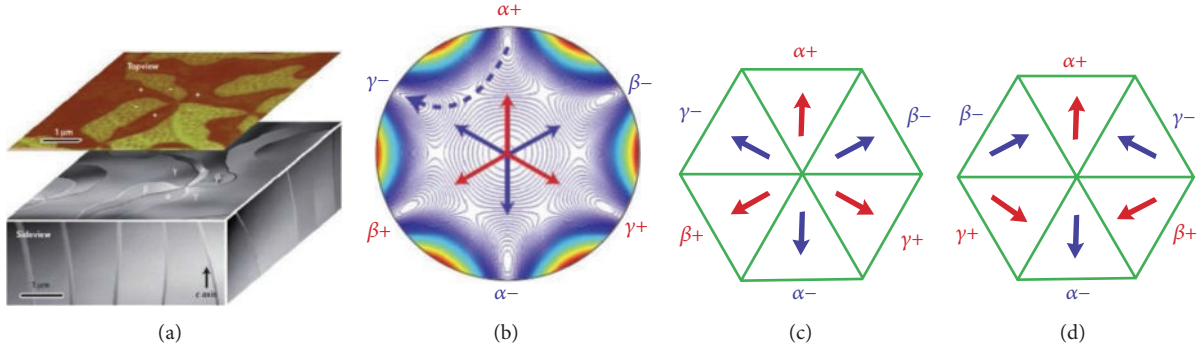


FIGURE 2: (a) Cloverleaf domain patterns in ferroelectric  $\text{YMnO}_3$  [19, 20]. The combination of TEM (bottom grey-scale layer) and conductive atomic force microscopy (top colored layer) images shows six crystallographic domains joining at a defect line with positive and negative polarization (+ and - signs in the conductive atomic force microscopy image, resp.) alternating around the defect. The TEM dark-field image is obtained by using the  $1\bar{3}1$  diffraction spot. (b) Contour plot of the free energy of hexagonal  $\text{YMnO}_3$ , where the six minima correspond to six structural domains. The arrows in the direction of the minima (colored blue and red) indicate the direction describing these states. The red and blue arrows also encode the sign of electric polarization. The dashed arrow connecting two neighboring minima is a lowest-energy domain wall. (c) and (d) Vortex and antivortex configurations correspond to the cloverleaf defect, respectively. The  $\alpha$ ,  $\beta$ , and  $\gamma$  antiphase domains correspond to the three options for the origin of trimerization.

the system, rotated by  $60^\circ$  angles, as depicted in Figure 2(b). The domain walls separating the structural domains are trajectories beginning in one minimum and ending in another. The lowest-energy domain walls connecting two neighboring minima are depicted by the dashed line in Figure 2(b). As is evident from the cloverleaf defects are therefore vortices where around the defect the phase angle goes successively through all six phases. This leaves only two possible domain sequences:  $\alpha+$ ,  $\beta-$ ,  $\gamma+$ ,  $\alpha-$ ,  $\beta+$ , and  $\gamma-$  (vortex) and  $\alpha+$ ,  $\gamma-$ ,  $\beta+$ ,  $\alpha-$ ,  $\gamma+$ , and  $\beta-$  (antivortex). Therefore, the electric alternating sign of polarization of neighboring domains, such domain walls flip the electric polarization. The polarization changes sign at each domain wall (Figures 2(c) and 2(d)).

Such vortices are stable topological defects that cannot be unwound by local lattice distortions. The  $60^\circ$  rotation of spins at domain boundaries implies that the cloverleaf defects are also magnetic vortices where lattice distortions and spins rotate together. It would be interesting to find out whether this amazingly complex interplay between structural, electric and magnetic properties of defects can lead to new magneto-electric phenomena. Similarly, the cloverleaf domain patterns in  $\text{YMnO}_3$  thin films are also reported by Matsumoto et al. [21], as shown in Figure 3. In a low-magnification dark-field TEM image (Figure 3(a)), the multiferroic cloverleaf domains are elongated along the  $c$ -axis of the specimen as indicated

with an arrow. Some vortices can be observed in the field-of-view and an enlargement of a vortex as designated by a white rectangle is shown in Figure 3(b) (as a false-color image). After numerous TEM observations, it is found that vortices with at least two domain boundaries along the  $c$ -axis (transverse domain wall, TDW) are stable during TEM observations. Along with TDW, no charge is exposed whereas a small amount of charge is exposed at the longitudinal domain boundary (LDW) at the core. In contrast, an unstable vortex is shown in the center of Figure 3(c), which appears as a four-leaves-like vortex. The contrast appeared to be blurred near the vortex and all of the boundaries were found to be mostly perpendicular to the  $c$ -axis. A fair amount of charges are exposed along the LDW making such a vortex structure unstable under the electron irradiation. The ferroelectric and antiferromagnetic domains have been confirmed to be interlocked with each other by a simultaneous observation by contact AFM and low temperature MFM [22]. Anisotropic conduction through the domain boundary was also observed, which could lead to tunable and flexible design of multiferroic devices [23]. To better understand the physical and chemical mechanism of multiferroicity in multiferroic hexagonal  $\text{YMnO}_3$ , a visualization technique based on spherical aberration-corrected STEM with atomic resolution has been employed to characterize the charge and

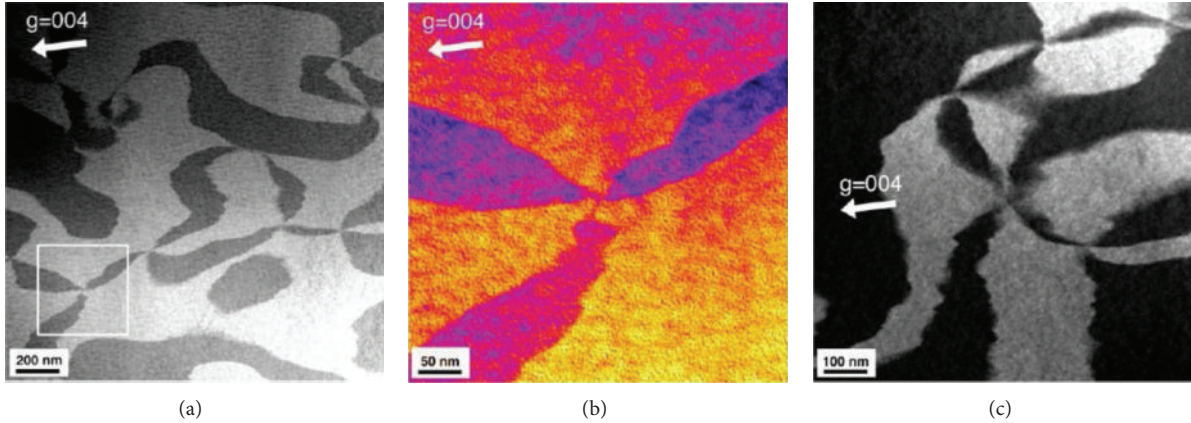


FIGURE 3: (a) A conventional dark-field TEM image of the multiferroic cloverleaf domains in the  $\text{YMnO}_3$  crystal near the  $[110]$  zone axis [21]. Note that the domains are elongated along the  $c$ -axis as indicated with an arrow. (b) An enlargement of the vortex designated by a white rectangle is shown as a pseudocolor representation. (c) An instable vortex observed in some field of view.

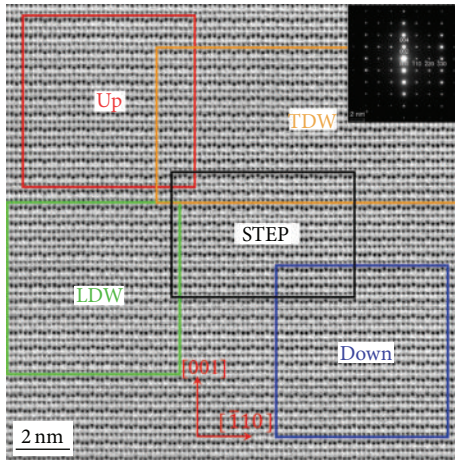


FIGURE 4: High-resolution ABF-STEM image of the  $\text{YMnO}_3$  single crystal recorded along the  $[110]$  direction, where five different kinds of domain structures (marked as Up, Down, TDW, LDW, and STEP in the figure) are observed [21].

uncharged domain walls in multiferroic hexagonal  $\text{YMnO}_3$ , where the annular bright-field (ABF) imaging technique is also used to reveal the light atomic element of oxygen. To further reduce the residual and statistical noises in the STEM images, multivariate statistical analysis (MSA) technique is also used [24]. Figure 4 demonstrates a high-resolution ABF-STEM image recorded along the  $[110]$  direction from a part of the field-of-view shown in Figure 3(b), where five different kinds of domain structures (marked as Up, Down, TDW, LDW, and STEP in the figure) are observed in the same field of view in the image [21]. The MSA reconstructed score images from the LDW region and TDW region with color obtained from the HAADF (a, c) and ABF (b, d) images are shown in Figure 5, respectively. It is clear that the transition between the two opposite polarization is atomically sharp in both images. The separation was found to be as good as that for an artificial image group constructed from

upward only and downward only region (Up and Down in Figure 4). Therefore, with the aid of MSA technique, unbiased and quantitative maps of ferroelectric domain structures with atomic resolution have been obtained. Such a statistical image analysis of the transition region between opposite polarizations has confirmed the atomically sharp transitions of ferroelectric polarization both in antiparallel (uncharged) and tail-to-tail  $180^\circ$  (charged) domain boundaries. Based on these analyses, a correlated subatomic image shift of the Mn–O layers with that of Y layers, exhibiting a double-arc shape of reversed curvatures, has been elucidated. The amount of image shift in Mn–O layers along the  $c$ -axis is statistically significant as small as 0.016 nm, roughly one-third of the evident image shift of 0.048 nm in Y layers. In addition, such a subatomic image shift in Mn–O layers vanishes at the tail-to-tail  $180^\circ$  domain boundaries. By using aberration-corrected high-angle annular-dark-field (HAADF) imaging technique the domain configurations and atomic structures of the vortex in multiferroic hexagonal  $\text{YMnO}_3$  has been directly identified along the  $[100]$  direction, as shown in Figure 6 [25]. Due to the Z-contrast characteristics of the HAADF imaging, the big bright spots correspond to Y atoms and the small bright spots correspond to Mn atoms. Note that  $[100]$  direction is the most suitable for imaging the DWs and identifying the location of the vortex core, where the shift of Y ions can be observed without overlapping. The different configurations of  $Y_{\text{up}}$  and  $Y_{\text{down}}$  atoms comparing to the  $\text{MnO}_5$  polyhedra, which appears wavy-like, indicate that  $\text{YMnO}_3$  has two opposite polarized states, which are indicated by the yellow upward and blue downward arrows, respectively. Since the HAADF contrast is generally less affected by small variation of specimen thickness, therefore, mapping the atomic position of heavier ions using HAADF approach is a reliable method to measure ion displacements and to further calculate the polarization. Six ferroelectric domains can be distinguished clearly by the up-down-down and down-up-up arrangements of Y ions and their polarizations are marked by upward arrows and downward arrows, respectively, as shown in Figure 6. It is found the six DWs can

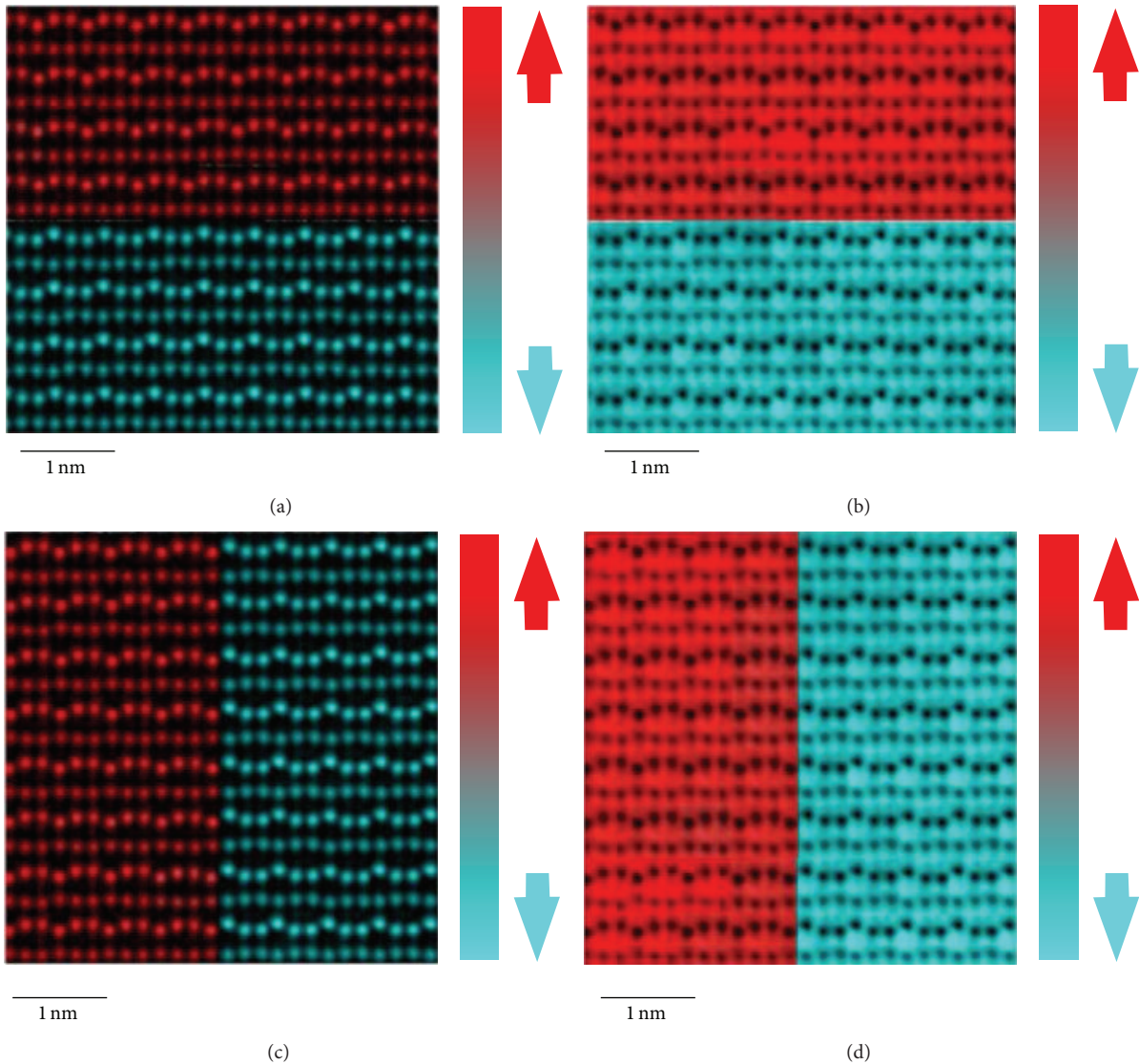


FIGURE 5: MSA (multivariate statistical analysis) reconstructed score images from the LDW region and TDW region with color obtained by from (a, c) the HAADF and (b, d) ABF images [21].

be classified into two types by their displacements across the DWs: type-I  $1/6$  [210] and type-II  $1/3$  [210]. Six translation-ferroelectric domains denoted by  $\alpha+$ ,  $\gamma-$ ,  $\beta+$ ,  $\alpha-$ ,  $\gamma+$ , and  $\beta-$ , respectively, were recognized, demonstrating interlocking nature of the antivortex domain. The core region of nearly zero polarization was found to be about four unit cells width. These results demonstrated that the polarization reverse can be realized efficiently by the adjustments of displacements of Y ions within several unit cells at both DWs and the antivortex core, demonstrating the trimerization nature of improper ferroelectricity of  $\text{YMnO}_3$ . These findings provide a solid evidence for the understanding of topological behaviors and intriguing physics of the vortex in  $\text{RMnO}_3$  and pave the way for further theoretical calculation.

**2.3. Multiferroic Domains in Charge-Ordered  $\text{LuFe}_2\text{O}_4$  Multiferroics.** Recently multiferroicity is observed in  $\text{LuFe}_2\text{O}_4$ , which is due to ferroelectricity originating from  $\text{Fe}^{2+}/\text{Fe}^{3+}$

charge order at the ferromagnetic transition temperature. The crystal structure of  $\text{LuFe}_2\text{O}_4$  consists of the alternate stacking of triangular lattices of rare-earth elements, iron and oxygen. An equal amount of  $\text{Fe}^{2+}$  and  $\text{Fe}^{3+}$  coexists at the same site in the triangular lattice. Compared with the average iron valence of  $\text{Fe}^{2.5+}$ ,  $\text{Fe}^{3+}$ , and  $\text{Fe}^{2+}$  are considered as having an excess and a deficiency of half an electron, respectively. The Coulombic preference for pairing of “oppositely” signed charges ( $\text{Fe}^{2+}$  and  $\text{Fe}^{3+}$ ) is considered to cause the degeneracy in the lowest energy for the charge configuration in the triangular lattice, similarly to the triangular antiferromagnetic Ising spins. Thus,  $\text{RFe}_2\text{O}_4$  is considered to be a charge-frustrated system of triangular lattices, where ferroelectricity is originated from the electron distribution. It is expected that real-space observations of the charge-ordered domains will provide crucial information for a deeper understanding of the process of frustrated charge ordering in the triangular lattice. Since frustrated charge ordering gives rise to only weak

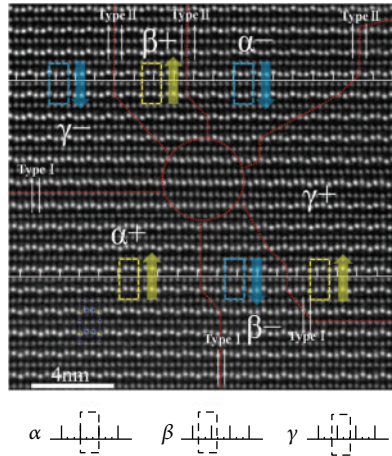


FIGURE 6: HAADF image of the antivortex domains in multiferroic  $\text{YMnO}_3$  [25]. Yellow and blue rectangles are used to mark the upward and downward polarized unit cells, respectively. The yellow upward and blue downward arrows indicate the different direction of polarization, respectively. Two white horizontal lines are superposed on the image to identify the relative translation relationship among  $\alpha$ ,  $\beta$ , and  $\gamma$  domains. The DWs are marked by red dotted lines and the red circle is used to mark the region of the vortex core. The types of six DWs are also outlined by the white vertical lines, labeled by type-I and type-II. The schematics of the three translation domains are presented at the bottom. The broken rectangles are used to indicate the same polarized unit cells. The black ruler are scaled by the lattice periodicity projected along the  $[100]$  direction. The positions of the broken rectangles relative to the short vertical lines in the black ruler reflect their translation relationship.

satellite reflections (i.e., diffuse scattering), so the technique of energy-filtered TEM is employed to significantly improve the visibilities of electron diffraction patterns and the dark-field images obtained using such weak reflections. Figure 7 shows the morphology of charge-ordered domains in  $\text{LuFe}_2\text{O}_4$  [26]. Figure 7(a) is the selected area electron diffraction pattern of  $\text{LuFe}_2\text{O}_4$  recorded at 299 K, which exhibits a feature of a characteristic diffuse scattering caused by charge ordering in  $\text{LuFe}_2\text{O}_4$ , as marked by the black arrows in Figure 7(a). The diffuse scattering is accompanied by streaks in the direction of  $c^*$  axis due to suppression of interlayer correlation between Fe double layers, which are separated by Lu–O sheets. The trace of diffuse scattering is not linear; instead, it has a slightly zigzag shape. This modulation can be explained by a small peak shift perpendicular to the  $c^*$  axis whose magnitude depends on the index  $l$ . X-ray diffraction patterns of the  $\text{LuFe}_2\text{O}_4$  single crystals reveal that the diffuse scattering has intensity maxima at approximately  $(h/3, h/3, l + 3/2)$  in reciprocal space, where  $h$  and  $l$  are the Miller indices [27, 28]. Based on the full width at half maximum (FWHM) of the diffuse scattering pattern measured perpendicular to the  $c^*$  axis at the position of the intensity maxima, the sizes of charge ordering domains are estimated to be  $\sim 4.7$  nm at 299 K. To determine the charge-ordered domain structure in real space, a dark-field image (Figure 7(b)) was obtained by using the diffuse scattering indicated by the circle in the inset. That reveals the

nanometer-scale charge-ordered domains, which exhibit as the bright dots in Figure 7(b). The size of bright dots seems smaller than the correlation length ( $\sim 4.7$  nm) deduced from the FWHM. It appears likely that the bright dots represent the portions which show a significant degree of charge ordering, for example, the inner portions of charge-ordered domains. In other words, the outskirts regions having a lower degree of charge ordering than the inner portions do not provide sufficient brightness in the dark-field image. To determine the average spacing between the bright dots observed by dark-field imaging at 299 K, the number of nanometer-scale dots ( $N$ ), such as those indicated by red points in Figure 7(c) is calculated. With respect to agglomerations observed in the dark-field image, it was difficult to determine the true positions of individual charge-ordered domains. Because of these uncertainties, the observations of  $N$  were dispersed from 132 to 190.

Based on the above results it can be concluded that dark-field imaging revealed a spot-like contrast of the charge-ordered domains. Although electron diffraction patterns demonstrated the development of charge ordering upon cooling, the observable domain size remained on a nanometer scale (i.e., smaller than 10 nm) over a wide temperature range between  $T_{\text{CO}}$  ( $\sim 310$  K) and 88 K. These findings indicate that the charge ordering is constrained by the geometric aspects of the crystal structure, such as the triangular lattice and the discreteness of the Fe double layers. An average spacing between neighboring domains (spacing between domain centers) of was determined to be 5–7 nm at 299 K. This value was comparable with the in-plane ( $c$  plane) correlation length ( $\sim 4.7$  nm) deduced from the FWHM of the diffuse scattering. It is conjectured that there are only small charge-disordered regions separating neighboring charge-ordered regions. Such small ferroelectric domains are free from the lattice distortion as observed by dark-field TEM, which can assist the realization of an extremely small ferroelectric element in high density ferroelectric random access memory. Such a fascinating potential for electron-ordered ferroelectricity will be pioneered in future research.

### 3. Concluding Remarks

In this paper, we have reviewed the recent progress in the characterizations of multiferroic domain structures in multiferroic oxides. Due to the existence of two or three primary ferroic order parameters simultaneously in the same phase multiferroics and intricately coupling each other, new amazing multiferroic properties and/or phenomena are realized by combinations of distinct nanometer-scale charge-ordered domains, cloverleaf domain structures, and topological defects such as multiferroic vortex-antivortex pairs. Therefore, the importance of multiferroic domain analyses will be enhanced in the future. However, in order to explore these complex and nano-scaled structures with high precision, improvements on the microscopic methods should be sustained. Recent development of spherical aberration correction is revolutionizing the performance of HRTEM/STEM instruments, which allows ones to achieve a spatial resolution

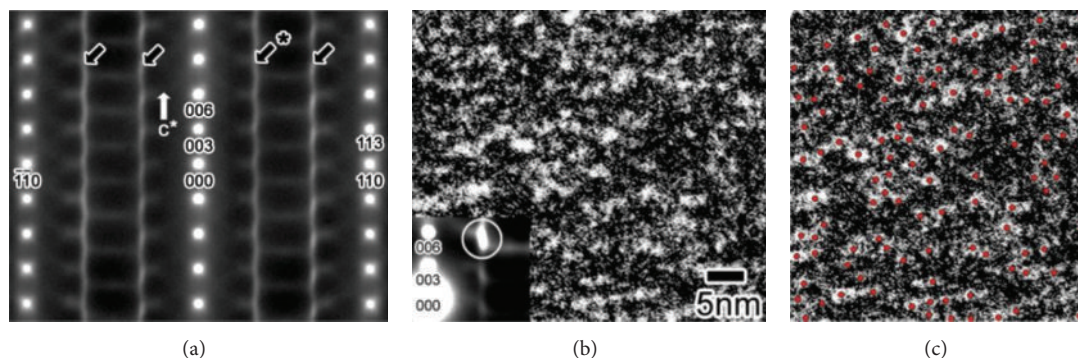


FIGURE 7: Morphology of charge-ordered domains in  $\text{LuFe}_2\text{O}_4$  [26]. (a) SAED pattern of  $\text{LuFe}_2\text{O}_4$  recorded at 299 K. (b) Dark-field TEM image of the charge-ordered domains obtained by using the diffuse scattering indicated by the circle in the inset. The charge-ordered domains are imaged as bright dots. (c) Nanometer-scale bright dots (indicated in red) representing the charge-ordered domains, which are used to determine the average spacing between the neighboring charge-ordered domains.

better than 0.08 nm and an energy resolution better than 100 meV. Such breakthrough would bring us to see and thoroughly explore the multiferroic domain structures at subangstrom scale. Another fascinating task is to combine the measurements of multiferroic physical properties (e.g., ferroelectric, magnetic, and magnetoelectric coupling properties) with the multiferroic domain analysis as performed here. This type of simultaneous measurements will be necessary for further understanding of the ferroelectric, magnetic and/or magnetoelectric coupling between the small domains. An exciting new era for multiferroic domain characterizations in multiferroic oxides is on the horizon!

### Conflict of Interests

The authors declare that there is no conflict of interests regarding the publication of this paper.

### Acknowledgments

This work was partially supported by National Natural Science Foundation of China (Grant nos. 11174122 and 11134004), National Basic Research Program of China (Grant nos. 2015CB654900 and 2012CB619400), and the open project from National Laboratory of Solid State Microstructures, Nanjing University.

### References

- [1] N. A. Spaldin, S.-W. Cheong, and R. Ramesh, "Multiferroics: past, present, and future," *Physics Today*, vol. 63, no. 10, pp. 38–43, 2010.
- [2] S. W. Cheong and M. Mostovoy, "Multiferroics: a magnetic twist for ferroelectricity," *Nature Materials*, vol. 6, no. 1, pp. 13–20, 2007.
- [3] J. F. Scott, "Data storage: multiferroic memories," *Nature Materials*, vol. 6, no. 4, pp. 256–257, 2007.
- [4] K. F. Wang, J.-M. Liu, and Z. F. Ren, "Multiferroicity: the coupling between magnetic and polarization orders," *Advances in Physics*, vol. 58, no. 4, pp. 321–448, 2009.
- [5] K. Aizu, "Possible species of ferromagnetic, ferroelectric, and ferroelastic crystals," *Physical Review B*, vol. 2, no. 3, pp. 754–772, 1970.
- [6] L. A. Shuvalov, E. F. Dudnik, and S. V. Wagin, "Domain-structure geometry of real ferroelastics," *Ferroelectrics*, vol. 65, no. 1, pp. 143–152, 1985.
- [7] H. Schmid, E. Burkhardt, E. Walker et al., "Polarized light and X-ray precession study of the ferroelastic domains of  $\text{YBa}_2\text{Cu}_3\text{O}_{7-\delta}$ ," *Zeitschrift für Physik B: Condensed Matter*, vol. 72, no. 3, pp. 305–322, 1988.
- [8] K. W. Urban, "Studying atomic structures by aberration-corrected transmission electron microscopy," *Science*, vol. 321, no. 5888, pp. 506–510, 2008.
- [9] K. W. Urban, C.-L. Jia, L. Houben, M. Lentzen, S.-B. Mi, and K. Tillmann, "Negative spherical aberration ultrahigh-resolution imaging in corrected transmission electron microscopy," *Philosophical Transactions of the Royal Society A: Mathematical, Physical and Engineering Sciences*, vol. 367, no. 1903, pp. 3735–3753, 2009.
- [10] P. Gao, J. Britson, J. R. Jokisaari et al., "Atomic-scale mechanisms of ferroelastic domain-wall-mediated ferroelectric switching," *Nature Communications*, vol. 4, article 2791, 9 pages, 2013.
- [11] G. Catalan and J. F. Scott, "Physics and applications of bismuth ferrite," *Advanced Materials*, vol. 21, no. 24, pp. 2463–2485, 2009.
- [12] C. T. Nelson, B. Winchester, Y. Zhang et al., "Spontaneous vortex nanodomain arrays at ferroelectric heterointerfaces," *Nano Letters*, vol. 11, no. 2, pp. 828–834, 2011.
- [13] J. Li, H. X. Yang, H. F. Tian et al., "Scanning secondary-electron microscopy on ferroelectric domains and domain walls in  $\text{YMnO}_3$ ," *Applied Physics Letters*, vol. 100, no. 15, Article ID 152903, 2012.
- [14] C. C. Neacsu, B. B. Van Aken, M. Fiebig, and M. B. Raschke, "Second-harmonic near-field imaging of ferroelectric domain structure of  $\text{YMnO}_3$ ," *Physical Review B*, vol. 79, no. 10, Article ID 100107, 2009.
- [15] T. Jungk, Á. Hoffmann, M. Fiebig, and E. Soergel, "Electrostatic topology of ferroelectric domains in  $\text{YMnO}_3$ ," *Applied Physics Letters*, vol. 97, no. 1, Article ID 012904, 2010.
- [16] S. C. Chae, N. Lee, Y. Horibe et al., "Direct observation of the proliferation of ferroelectric loop domains and vortex-antivortex pairs," *Physical Review Letters*, vol. 108, no. 16, Article ID 167603, 5 pages, 2012.

- [17] T. Katsufuji, S. Mori, M. Masaki, Y. Moritomo, N. Yamamoto, and H. Takagi, "Dielectric and magnetic anomalies and spin frustration in hexagonal  $\text{RMnO}_3$  ( $\text{R}=\text{Y}$ ,  $\text{Yb}$ , and  $\text{Lu}$ )," *Physical Review B: Condensed Matter and Materials Physics*, vol. 64, no. 10, Article ID 104419, 6 pages, 2001.
- [18] T. Asaka, K. Nemoto, K. Kimoto, T. Arima, and Y. Matsui, "Crystallographic superstructure of Ti-doped hexagonal  $\text{YMnO}_3$ ," *Physical Review B: Condensed Matter and Materials Physics*, vol. 71, no. 1, Article ID 014114, 2005.
- [19] T. Choi, Y. Horibe, H. T. Yi, Y. J. Choi, W. Wu, and S.-W. Cheong, "Insulating interlocked ferroelectric and structural antiphase domain walls in multiferroic  $\text{YMnO}_3$ ," *Nature Materials*, vol. 9, no. 3, pp. 253–258, 2010.
- [20] S. C. Chae, Y. Horibe, D. Y. Jeong, S. Rodan, N. Lee, and S.-W. Cheong, "Self-organization, condensation, and annihilation of topological vortices and antivortices in a multiferroic," *Proceedings of the National Academy of Sciences of the United States of America*, vol. 107, no. 50, pp. 21366–21370, 2010.
- [21] T. Matsumoto, R. Ishikawa, T. Tohei et al., "Multivariate statistical characterization of charged and uncharged domain walls in multiferroic hexagonal  $\text{YMnO}_3$  single crystal visualized by a spherical aberration-corrected STEM," *Nano Letters*, vol. 13, no. 10, pp. 4594–4601, 2013.
- [22] M. Fiebig, T. Lottermoser, D. Fröhlich, A. V. Goltsev, and R. V. Pisarev, "Observation of coupled magnetic and electric domains," *Nature*, vol. 419, no. 6909, pp. 818–820, 2002.
- [23] D. Meier, J. Seidel, A. Cano et al., "Anisotropic conductance at improper ferroelectric domain walls," *Nature Materials*, vol. 11, no. 4, pp. 284–288, 2012.
- [24] M. Watanabe, *X-Ray Energy-Dispersive Spectrometry in Scanning Transmission Electron Microscopes*, edited by S. J. Pennycook, P. D. Nellist, Springer, New York, NY, USA, 2011.
- [25] Q. Zhang, G. Tan, L. Gu et al., "Direct observation of multiferroic vortex domains in  $\text{YMnO}_3$ ," *Scientific Reports*, vol. 3, article 2741, 5 pages, 2013.
- [26] T. Maruyama, Y. Murakami, D. Shindo, N. Abe, and T. Arima, "Observations of charge-ordered and magnetic domains in  $\text{LuFe}_2\text{O}_4$  using transmission electron microscopy," *Physical Review B—Condensed Matter and Materials Physics*, vol. 86, no. 5, Article ID 054202, 2012.
- [27] M. Angst, R. P. Hermann, A. D. Christianson et al., "Charge order in  $\text{LuFe}_2\text{O}_4$ : antiferroelectric ground state and coupling to magnetism," *Physical Review Letters*, vol. 101, no. 22, Article ID 227601, 2008.
- [28] Y. Yamada, K. Kitsuda, S. Nohdo, and N. Ikeda, "Charge and spin ordering process in the mixed-valence system  $\text{LuFe}_2\text{O}_4$ : charge ordering," *Physical Review B*, vol. 62, no. 18, pp. 12167–12174, 2000.

## Research Article

# Ferroelectric and Dielectric Properties of $\text{ZnFe}_2\text{O}_4$ - $\text{Pb}(\text{ZrTi})\text{O}_3$ Multiferroic Nanocomposites

Shrabanee Sen, Sk. Md. Mursalin, and M. Maharajan

Sensor & Actuator Division, Central Glass and Ceramics Research Institute, 196 Raja SC Mullick Road, Kolkata 700032, India

Correspondence should be addressed to Shrabanee Sen; [shrabanee@cgcrici.res.in](mailto:shrabanee@cgcrici.res.in)

Received 8 April 2014; Accepted 3 September 2014

Academic Editor: Debasis Dhak

Copyright © 2015 Shrabanee Sen et al. This is an open access article distributed under the Creative Commons Attribution License, which permits unrestricted use, distribution, and reproduction in any medium, provided the original work is properly cited.

Magnetolectric composites of zinc ferrite and soft lead zirconate titanate (PZT) having formula  $0.5 \text{ZnFe}_2\text{O}_4$ - $0.5 \text{PZT}$  were synthesized by sol-gel technique. X-ray diffraction analysis was carried out to confirm the coexistence of individual phase. TEM micrographs were taken to confirm the formation of nanosized powders and SEM micrographs were taken to study the morphology of the sintered pellets. Dielectric and P-E hysteresis loops were recorded, respectively, to confirm the ferroelectric properties of the composites.

## 1. Introduction

The multiferroics are functional materials combining several ferroic properties in the same material. They usually exhibit simultaneously magnetic and ferroelectric order and a coupling between them. In recent years much attention has been given for the development of magnetolectric materials due to their possible applications as sensors, memories, transducers, and actuators. One of the important classes of magnetolectric materials includes ferrite piezoelectric composites. In such materials the magnetolectric effect is a product property that depends on the piezoelectric and piezomagnetic coefficients, volume fraction of composite components, and magnetic, dielectric properties of composite components. The suitable combination of two phases such as piezomagnetic or magnetostrictive and piezoelectric phase can yield a desirable ME property [1–3]. Till date various ME composites have been prepared consisting of ferroelectric materials like  $\text{BaTiO}_3$ ,  $\text{Pb}(\text{Zr})\text{TiO}_3$ ,  $\text{BaPbTiO}_3$ , and so forth and Ni, Co, Mg, Zn ferrites as magnetic phase [4–6]. The main advantage of synthesizing sintered ME composites is related to the easy and cheap fabrication and the possibility to control the molar ratios of phases, grain size, and densification.

For the present work, nanocomposites of  $0.5 \text{ZnFe}_2\text{O}_4$ - $0.5$  soft  $\text{Pb}(\text{ZrTi})\text{O}_3$  were prepared by the sol-gel method and

the structural, microstructural, and dielectric properties were studied and compared with the parent compound, that is, PZT.

## 2. Experiment

**2.1. Material Synthesis.** The nanocomposites were prepared by a two-step technique. In the first step  $\text{ZnFe}_2\text{O}_4$  nanopowders were prepared by a sol-gel technique. The precursor materials for  $\text{ZnFe}_2\text{O}_4$  were  $\text{Zn}(\text{NO}_3)_2 \cdot 6\text{H}_2\text{O}$  (Aldrich) and  $\text{Fe}(\text{NO}_3)_3 \cdot 9\text{H}_2\text{O}$  (Aldrich). At first, the stoichiometric amount of  $\text{Zn}(\text{NO}_3)_2 \cdot 6\text{H}_2\text{O}$  and  $\text{Fe}(\text{NO}_3)_3 \cdot 9\text{H}_2\text{O}$  was taken in a beaker, and a complete homogeneous solution was prepared in 200 mL of distilled water. This prepared solution was then stirred for 1 h. During the stirring, equimolar amount of citric acid was added to the solution. To that solution, soft lead zirconate titanate, that is, PZT (Sparkler ceramics), dissolved in nitric acid was added and the stirring was continued for more than 4 h, keeping the temperature in the range of 100 to 110°C. After that, finally a heavily dense form of the sol has been obtained. The sol was then put into the oven at 110°C and was left for 10 h to form a hard gel. The precursor powders were calcined for ~8 h at 500°C.

The powders were further reground thoroughly, pelletized, and sintered at 1250°C (2 h) in presence of excess

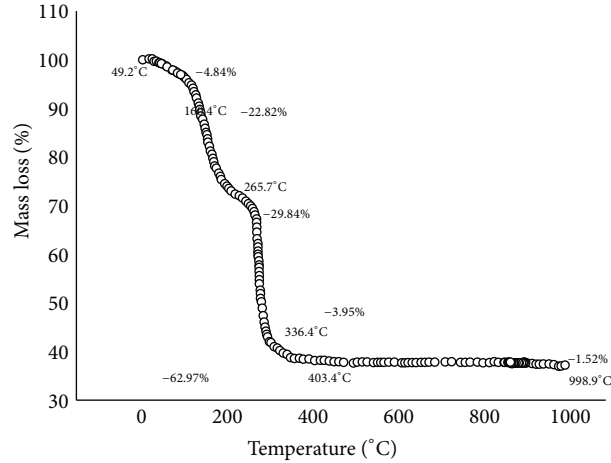


FIGURE 1: TGA of  $\text{ZnFe}_2\text{O}_4$ -PZT gel.

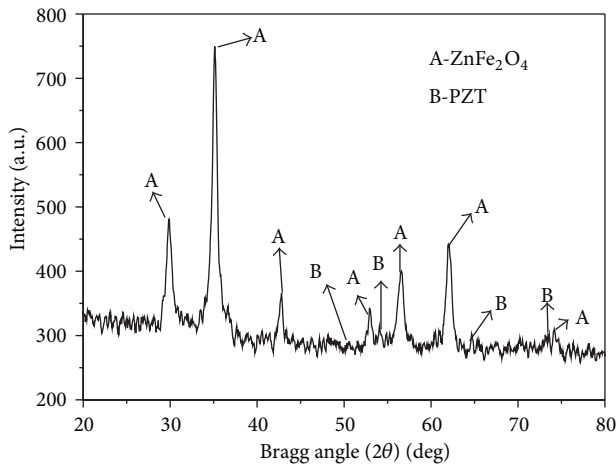


FIGURE 2: XRD of  $\text{ZnFe}_2\text{O}_4$ -PZT nanopowders.

lead oxide to obtain pellets required for characterization of electrical properties.

**2.2. Characterization.** Thermal analysis of the dried gel in air was done using Perkin Elmer Thermal Analyzer from 30°C to 1000°C at the heating rate of 10°C/min. The powder X-ray diffraction of synthesized  $\text{ZnFe}_2\text{O}_4$  powder was carried out using Bruker AXS D8 Advance system ( $\lambda = 1.5406 \text{ \AA}$ , with a step size of 0.05°). The morphology of the nanopowders was observed by Transmission Electron Microscope (Techno G<sup>2</sup>30 STWin) and the pellets were observed on a Field Emission Scanning Electron Microscope (SUPRA 35 VP) at different magnifications. For electrical measurements the pellets were polished and electroded with silver paint. The dielectric properties were measured by a LCR meter (Hioki 3532) as a function of frequency and temperature and the ferroelectric properties as a function of voltage were measured with Aixact Test Bench.

### 3. Results and Discussion

Figure 1 shows the thermal plot of  $\text{ZnFe}_2\text{O}_4$ -PZT gel. Since commercial PZT powder (Sparkler ceramics) was used and mixed, the plot is more or less identical to that of  $\text{ZnFe}_2\text{O}_4$  reported [7, 8]. The weight loss in the range 200°C–250°C in the TGA curve attributed to the liberation of surface adsorbed water. The drastic weight loss corresponds to the conventional oxidative decomposition of citric acid and nitrates. The redox reaction between citric acid, metal nitrates, and PZT mixture has completed above 400°C, indicating the completion of the decomposition of citric acid and nitrate salts. No weight loss above 400°C suggests the formation of crystalline 0.5  $\text{ZnFe}_2\text{O}_4$ -0.5 PZT as the decomposition product.

The XRD pattern of  $\text{ZnFe}_2\text{O}_4$ -PZT calcined at 500°C/8 h is shown in Figure 2. The formation of  $\text{ZnFe}_2\text{O}_4$ -PZT powder was confirmed by matching the peak position with the JCPDS file  $\text{ZnFe}_2\text{O}_4$  (PDF-821042) and soft PZT which is given in the inset. Hence formation of multiferroic composite was confirmed from structural characterization. The mean crystallite size of the powder was calculated using Scherrer formula and was found to be ~28 nm.

Figure 3(a) shows the TEM micrographs of 0.5  $\text{ZnFe}_2\text{O}_4$ -0.5 PZT nanocomposite. The average particle size estimated was ~35 nm. HRTEM micrographs (Figure 3(b)) show the perfect orientation of the lattice spacing and SAED pattern (Figure 3(c)) depicts the formation of distinct rings which confirms the formation of crystalline nature of the sample. The EDAX micrograph (Figure 3(d)) confirms that both the ferroelectric compound (PZT) and the ferromagnetic  $\text{ZnFe}_2\text{O}_4$  nanocrystals are present in the composite. Hence formation of multiferroic composite was confirmed. The atomic percentages of all the elements are given in Table 1.

FESEM micrographs of 0.5  $\text{ZnFe}_2\text{O}_4$ -0.5 PZT pellet at different magnifications (5 and 10 KX) and at different selected areas are shown in Figures 4(a) and 4(b). The homogeneous distribution of the grains of average size of 6–8  $\mu\text{m}$  with hexagonal shape having distinct grain boundaries is confirmed from the micrographs. Densely packed grains

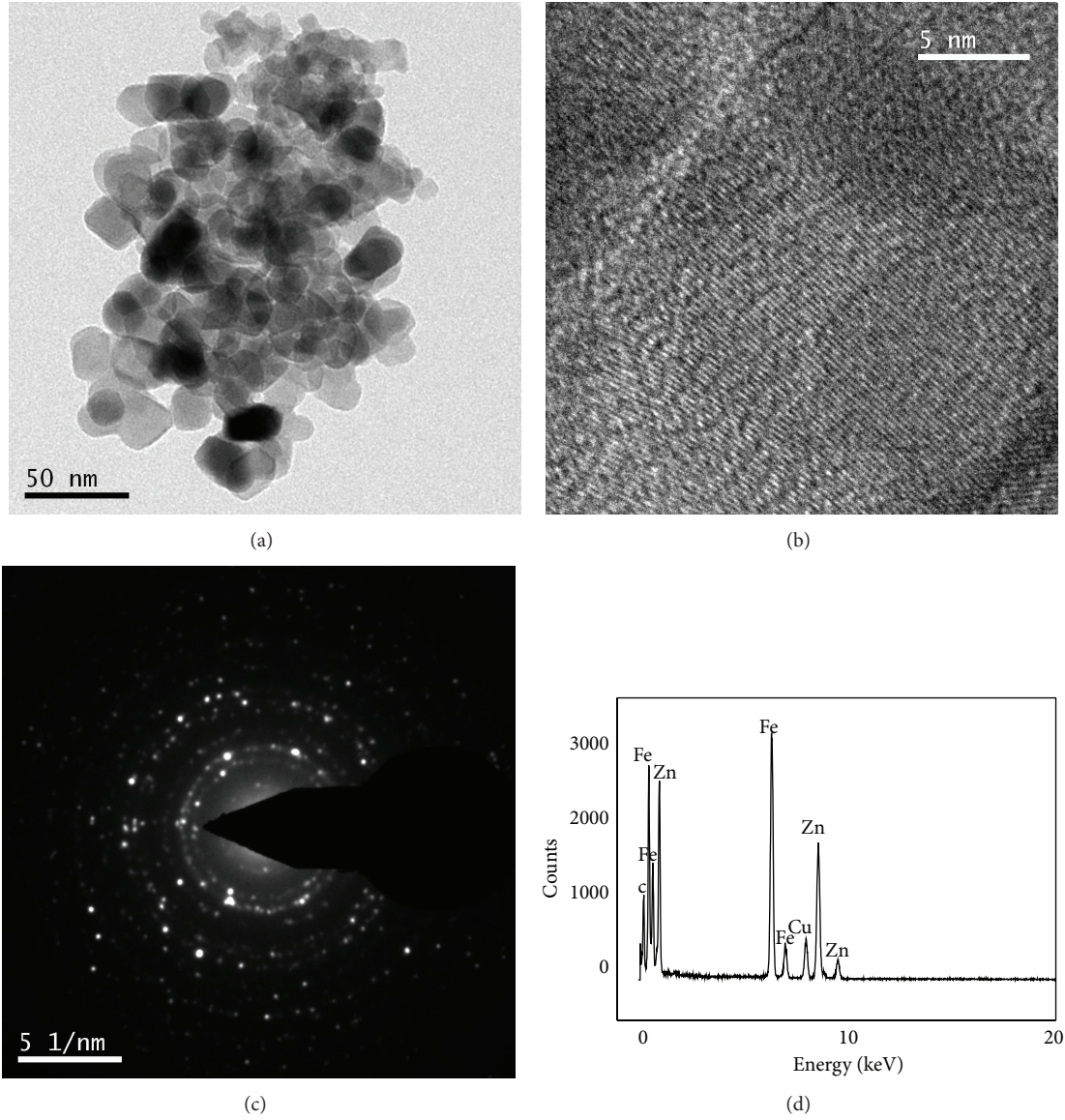


FIGURE 3: (a) TEM micrographs. (b) HRTEM micrographs. (c) SAED micrographs. (d) EDAX micrographs.

TABLE 1: Elemental analysis of  $\text{ZnFe}_2\text{O}_4$ -PZT composite.

Element	Weight %	Atomic %	Uncert. %	Correction	<i>k</i> -factor
O(K)	29.40	63.56	0.32	0.49	1.973
Ti(K)	0.09	0.06	0.01	0.98	1.193
Fe(K)	34.13	21.14	0.24	0.99	1.348
Zn(K)	23.75	12.56	0.23	0.99	1.671
Zr(K)	2.60	0.98	0.10	0.99	3.439
Pb(L)	10.00	1.67	0.23	0.75	5.806

with relative high density (>95%) were observed from these micrographs.

The variation of dielectric constant ( $\epsilon$ ) and dielectric loss ( $\tan \delta$ ) from 50 Hz to 5 MHz with variation from RT to 300°C

is shown in Figures 5(a) and 5(b). It has been observed that, with the increase of frequency,  $\epsilon$  value decreases and further remains almost constant. At lower frequencies all the polarization (i.e., electronic, ionic, dipolar, and interfacial) is present but at higher frequencies only the electronic polarization contributes to the dielectric constant. The value of the dielectric constant was less compared to that of the soft PZT which shows the effect of addition of  $\text{ZnFe}_2\text{O}_4$ . The dielectric loss decreased with the increase in frequency which is the general characteristics of a ferroelectric material. The variation of dielectric constant and tangent loss with temperature of the composite is shown in Figures 6(a) and 6(b). It is observed that the compounds do not exhibit phase transition up to the possible measurable temperature, that is, 300°C. There is a linear increase in both values within the measured temperature range. The dielectric constant value

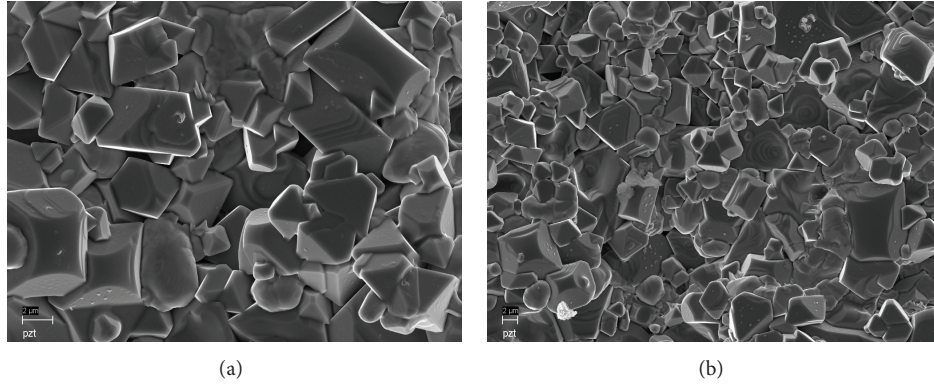


FIGURE 4: (a) FESEM micrographs at 10 KX magnification of  $ZnFe_2O_4$ -PZT pellet. (b) FESEM micrographs at 5 KX magnification of  $ZnFe_2O_4$ -PZT pellet.

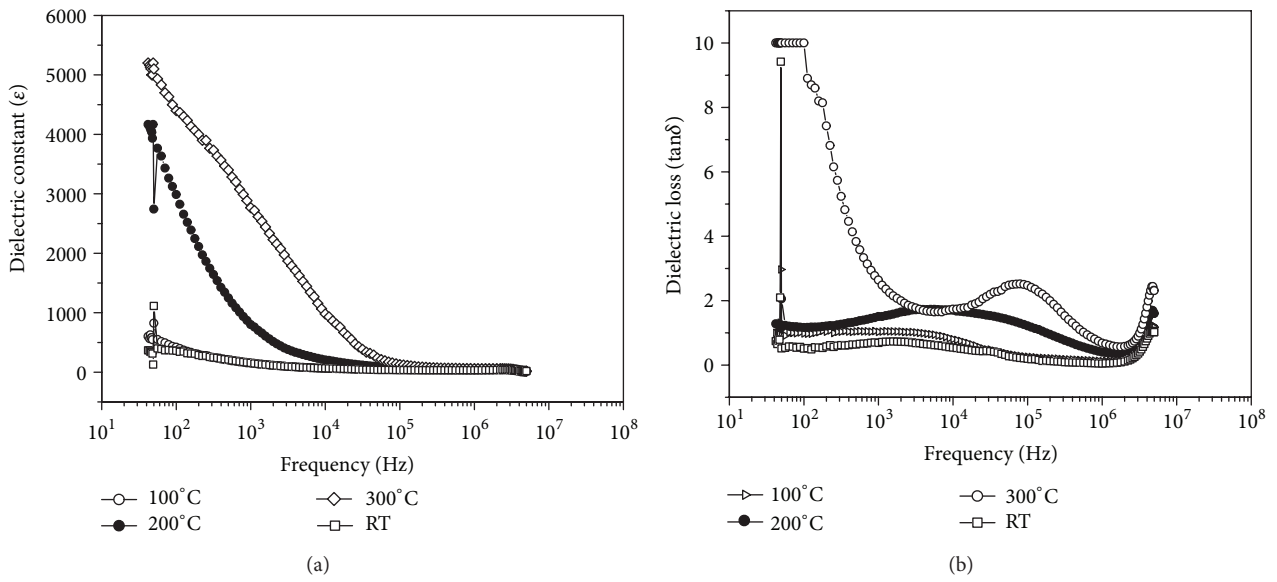


FIGURE 5: (a) Variation of dielectric constant with frequency at different temperatures. (b) Variation of dielectric loss with frequency at different temperatures.

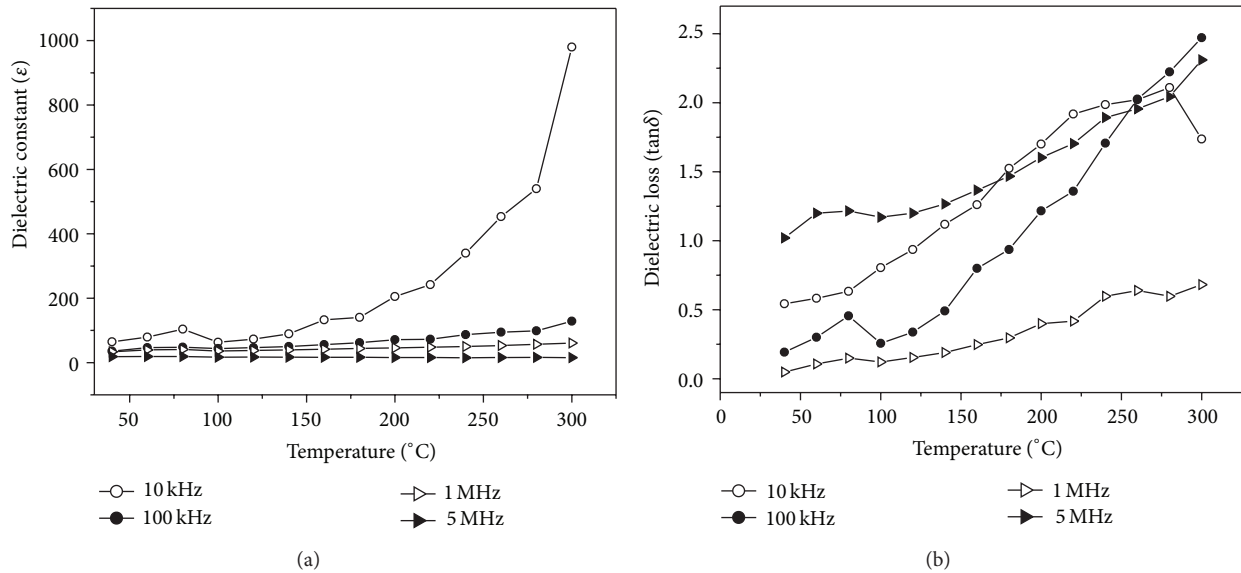


FIGURE 6: (a) Variation of dielectric constant with temperature at different frequencies. (b) Variation of dielectric loss with temperature at different frequencies.

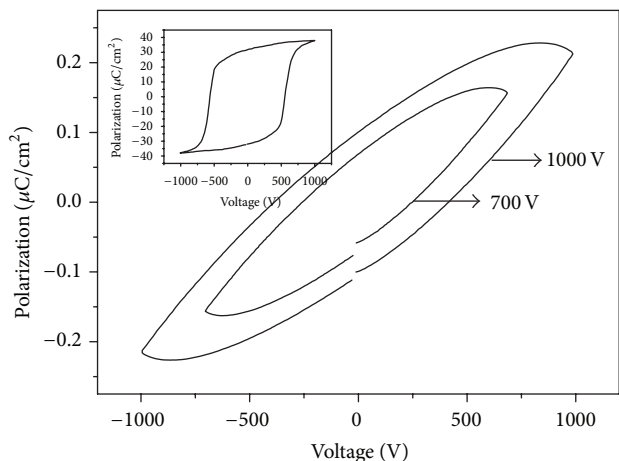


FIGURE 7: P-E loops of  $\text{ZnFe}_2\text{O}_4$ -PZT pellet compared with PZT pellet.

has decreased in comparison to soft PZT (PZT (RT) at 10 kHz = 1800).

Figure 7 shows the P-E hysteresis curve of the composite at room temperature. The remanent polarization ( $P_r$ ) nanocomposite was  $4 \mu\text{C}/\text{cm}^2$  applied voltage of 1 Kv while that of soft PZT was  $25 \mu\text{C}/\text{cm}^2$ . The similar loop of PZT sample is shown in the inset. The high reduction in the polarization value may be due to the interaction of the  $\text{ZnFe}_2\text{O}_4$  grains which results in the pinning effect of the ferroelectric domains.

#### 4. Conclusions

ZF-PZT composites were synthesized by sol-gel technique and were characterized by XRD, TEM, and SEM for structural and microstructural analysis. The dielectric constant decreased with respect to PZT. The observation of P-E hysteresis loops indicates the presence of ordered ferroelectric behaviour.

#### Conflict of Interests

The authors declare that there is no conflict of interests regarding the publication of this paper.

#### Acknowledgments

The authors would like to acknowledge Dr. K. Dasgupta (Director at CGCRI-CSIR) and Dr. A. Sen (Head at Sensor and Actuator Division) for giving permission for publishing this paper.

#### References

- [1] R. F. Gibson, *Principles of Composite Material Mechanics*, McGraw-Hill, 1994.
- [2] M. Taya, *Electronic Composites: Modeling, Characterization, Processing, MEMS Applications*, Cambridge University Press, Cambridge, UK, 2007.
- [3] J. Van Suchetelene, "Product properties: a new application of composite materials," *Philips Research Reports*, vol. 27, pp. 28–37, 1972.
- [4] R. Rani, J. K. Juneja, S. Singh, K. K. Raina, and C. Prakash, "Study of  $0.1\text{Ni}_{0.8}\text{Zn}_{0.2}\text{Fe}_2\text{O}_4-0.9\text{Pb}_{1-3x/2}\text{La}_x\text{Zr}_{0.65}\text{Ti}_{0.35}\text{O}_3$  magnetoelectric composites," *Journal of Magnetism and Magnetic Materials*, vol. 325, pp. 47–51, 2013.
- [5] H.-F. Zhang, S. W. Or, and H. L. W. Chan, "Electrical, magnetic, and magnetoelectric characterization of fine-grained  $\text{Pb}(\text{Zr}_{0.53}\text{Ti}_{0.47})\text{O}_3-(\text{Ni}_{0.5}\text{Zn}_{0.5})\text{Fe}_2\text{O}_4$  composite ceramics," *Journal of Alloys and Compounds*, vol. 509, no. 21, pp. 6311–6316, 2011.
- [6] C. E. Ciomaga, M. Airimioaei, V. Nica et al., "Preparation and magnetoelectric properties of  $\text{CoFe}_2\text{O}_4$ - $\text{Pb}(\text{ZrTi})\text{O}_3$  composites obtained in-situ by gel combustion method," *Journal of the European Ceramic Society*, vol. 32, p. 3325, 2013.
- [7] M. Maharajan, M. D. Mursalin, M. Narjinary, P. Rana, S. Sen, and A. Sen, "Synthesis, characterization and vapour sensing properties of nanosized  $\text{ZnFe}_2\text{O}_4$ ," *Transactions of the Indian Ceramic Society*, vol. 73, no. 2, pp. 102–104, 2014.
- [8] M. Veith, M. Haas, and V. Huch, "Single source precursor approach for the sol-gel synthesis of nanocrystalline  $\text{ZnFe}_2\text{O}_4$  and zinc-iron oxide composites," *Chemistry of Materials*, vol. 17, no. 1, pp. 95–101, 2005.

## Research Article

# Growth of BiFeO<sub>3</sub> Microcylinders under a Hydrothermal Condition

L. J. Di,<sup>1</sup> H. Yang,<sup>1,2</sup> T. Xian,<sup>1</sup> J. Y. Ma,<sup>2</sup> H. M. Zhang,<sup>1</sup> J. L. Jiang,<sup>1</sup>  
Z. Q. Wei,<sup>1</sup> and W. J. Feng<sup>1</sup>

<sup>1</sup>School of Science, Lanzhou University of Technology, Lanzhou 730050, China

<sup>2</sup>State Key Laboratory of Advanced Processing and Recycling of Non-Ferrous Metals, Lanzhou University of Technology, Lanzhou 730050, China

Correspondence should be addressed to H. Yang; [hyang@lut.cn](mailto:hyang@lut.cn)

Received 22 April 2014; Revised 26 September 2014; Accepted 26 September 2014

Academic Editor: Debasis Dhak

Copyright © 2015 L. J. Di et al. This is an open access article distributed under the Creative Commons Attribution License, which permits unrestricted use, distribution, and reproduction in any medium, provided the original work is properly cited.

BiFeO<sub>3</sub> microcylinders were synthesized via a hydrothermal condition. SEM observation reveals that with increasing the hydrothermal reaction time from 6 to 15 h, the microcylinders grow from ~0.7 to ~4.1 μm in height, whereas their diameter remains to be 3.7–3.8 μm with a minor change. The microcylinders are mainly made up of sphere-like grains of 100–150 nm in size. A possible growth mechanism of the BiFeO<sub>3</sub> microcylinders is proposed. The photocatalytic activity of the as-prepared BiFeO<sub>3</sub> samples was evaluated by the degradation of acid orange 7 under simulated sunlight irradiation, revealing that they possess an appreciable photocatalytic activity. Magnetic hysteresis loop measurement shows that the BiFeO<sub>3</sub> microcylinders exhibit a typical antiferromagnetic behavior at room temperature.

## 1. Introduction

Bismuth ferrite (BiFeO<sub>3</sub>) with a rhombohedrally distorted perovskite structure has been extensively studied as one of single-phase multiferroic materials in the past few years [1, 2]. BiFeO<sub>3</sub> exhibits ferroelectricity with a Curie temperature ( $T_C$ ) of ~830°C and antiferromagnetism with a Néel temperature ( $T_N$ ) of ~380°C, making it a promising candidate for room-temperature multiferroic applications [3, 4]. Furthermore, BiFeO<sub>3</sub> is an important semiconductor with bandgap energy of about 2.2 eV and has a pronounced photocatalytic activity for the degradation of various organic dyes under visible-light irradiation [5–11]. Generally, the physical and chemical properties of a functional material depend highly on its morphologies, dimensions, sizes, defects, and so forth. To tailor or enhance the properties of the material, it is especially interesting to create nano/microstructures with various morphologies. Up to now, a large number of nano/microstructures of BiFeO<sub>3</sub> have been synthesized including microplatelets, microcubes, nanotubes, nanofibers, microflowers, microspheres, micro-rods, thick film, microoctahedron, and nanoparticles [5–19].

Various wet chemical methods have been widely used to achieve those nano/microstructures of BiFeO<sub>3</sub>. Among them, the hydrothermal route has special advantages in tailoring the product morphology. The variation of any parameter in the hydrothermal reaction process, such as reaction temperature and time, mineralizer type and its concentration, pH value, metal ion concentration, and organic additive, could result in morphologically different products. In this work, we report the synthesis of BiFeO<sub>3</sub> microcylinders under a hydrothermal route and a possible growth mechanism of the microcylinders is proposed. The photocatalytic activity of as-prepared samples was evaluated by the degradation of acid orange 7 (AO7) under simulated sunlight irradiation.

## 2. Experimental

0.005 mol of Bi(NO<sub>3</sub>)<sub>3</sub>·5H<sub>2</sub>O and 0.005 mol of Fe(NO<sub>3</sub>)<sub>3</sub>·9H<sub>2</sub>O were dissolved in 20 mL of dilute nitric acid solution. Then to the mixture solution was added 60 mL KOH solution with a concentration of 9 mol·L<sup>-1</sup> drop by drop under magnetic stirring, and immediately a dark

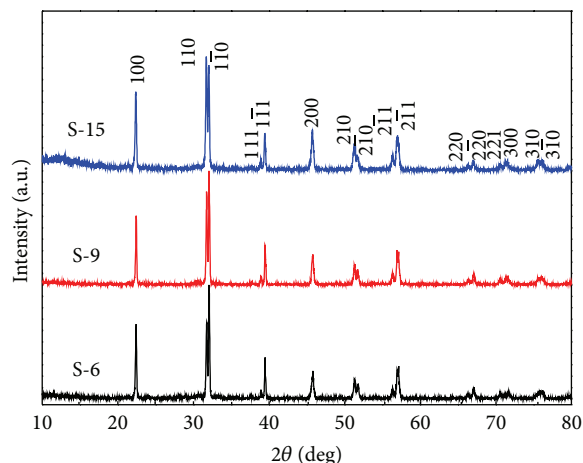


FIGURE 1: XRD patterns of  $\text{BiFeO}_3$  samples prepared at the reaction time of 6, 9, and 15 h (the corresponding samples are termed S-6, S-9, and S-15, resp.).

brown suspension solution was formed. The suspension was ultrasonically treated for 8 min and subsequently stirred vigorously with a magnetic stirrer for 30 min to create a highly uniform mixture. The resulted mixture was sealed in a Teflon-lined stainless steel autoclave of 100 mL capacity and submitted to hydrothermal treatment at  $200^\circ\text{C}$ . After different reaction time, the autoclave was cooled naturally to room temperature. The resulting brown precipitate was collected and washed several times with distilled water and absolute ethanol and then dried in a thermostat drying oven at  $80^\circ\text{C}$  for 12 h to obtain final  $\text{BiFeO}_3$  product. By varying the reaction time from 6 to 15 h, several  $\text{BiFeO}_3$  samples were prepared.

The phase purity of the samples was examined by means of X-ray powder diffraction (XRD) with  $\text{Cu K}\alpha$  radiation. The morphology of the samples was observed by field-emission scanning electron microscope (SEM). The ultraviolet- (UV-) visible diffuse reflectance spectra were measured using a UV-visible spectrophotometer with an integrating sphere attachment. A vibrating sample magnetometer (VSM) was used to measure the magnetic hysteresis loops of the samples at room temperature.

The photocatalytic activity of the products was evaluated by degrading AO7 in aqueous solution under simulated sunlight irradiation from a 200 W xenon lamp. The initial AO7 concentration was  $5 \text{ mg}\cdot\text{L}^{-1}$  and the  $\text{BiFeO}_3$  loading was 0.1 g in 200 mL of AO7 solution. Before illumination, the mixed solution was ultrasonically treated for 15 min in the dark to make  $\text{BiFeO}_3$  particles uniformly dispersed. During the photocatalysis process, the water-jacketed reactor was cooled with water-cooling system to keep the solution at room temperature. After irradiation for 8 h, the reaction solution was centrifuged for 10 min at  $3000 \text{ r}\cdot\text{min}^{-1}$  to remove  $\text{BiFeO}_3$  particles. The AO7 concentration was determined by measuring the absorbance of the solution at a fixed wavelength of 484 nm using an UV-visible spectrophotometer. The percentage degradation is defined as  $(C_0 - C_t)/C_0 \times 100\%$ , where  $C_0$  and  $C_t$  are the AO7 concentrations before and after irradiation, respectively.

### 3. Results and Discussion

Figure 1 shows the XRD patterns of  $\text{BiFeO}_3$  samples prepared at the reaction time of 6, 9, and 15 h (the corresponding samples are termed S-6, S-9, and S-15, resp.). For these samples, all the diffraction peaks can be indexed in terms of the rhombohedral structure of  $\text{BiFeO}_3$  with space group  $R3m$  (PDF card number 74-2016). No traces of other phases are detected in the XRD patterns, revealing high purity of the as-prepared products. The widths of the diffraction peaks undergo no obvious change between the samples, indicating that they have nearly the same grain or subgrain size.

Figure 2 shows the SEM images of the as-prepared  $\text{BiFeO}_3$  samples, revealing the synthesis of cylinder-like microparticles. When the hydrothermal reaction time is 6 h, the resulting sample consists of microcylinders with an average diameter of  $\sim 3.7 \mu\text{m}$  and height of  $\sim 0.7 \mu\text{m}$  (Figure 2(a)). When the reaction time is increased to 9 h, the obtained microcylinders have a diameter of  $\sim 3.8 \mu\text{m}$  and height of  $\sim 1.7 \mu\text{m}$  (Figure 2(b)). Further prolonging of the reaction time up to 15 h leads to the formation of microcylinders with a diameter of  $\sim 3.8 \mu\text{m}$  and height of  $\sim 4.1 \mu\text{m}$  (Figure 2(c)). This implies the continuous growth of  $\text{BiFeO}_3$  microcylinders along the direction of height with increasing the reaction time, whereas their diameter undergoes minor change. Figure 2(d) shows an enlarged view of the SEM image of Figure 2(b), revealing that the microcylinders are mainly made up of sphere-like grains of 100–150 nm in size.

Figure 3 shows a possible growth mechanism of the cylinder-like  $\text{BiFeO}_3$  particles. Initially,  $\text{Bi}^{3+}$  and  $\text{Fe}^{3+}$  ions react with  $\text{OH}^-$  ions to produce amorphous  $\text{Bi}(\text{OH})_3$  and  $\text{Fe}(\text{OH})_3$  precipitates, and then the hydroxides undergo an attack of the mineralizer, KOH, to dissolve and form ion groups. These species undergo nucleation and growth when critical supersaturation is reached, leading to the formation of  $\text{BiFeO}_3$  nanocrystals. The nascent nanocrystals come together or self-assemble to form cylinder-like aggregates. This self-organization process can be understood according to the oriented-attachment growth mechanism, where the

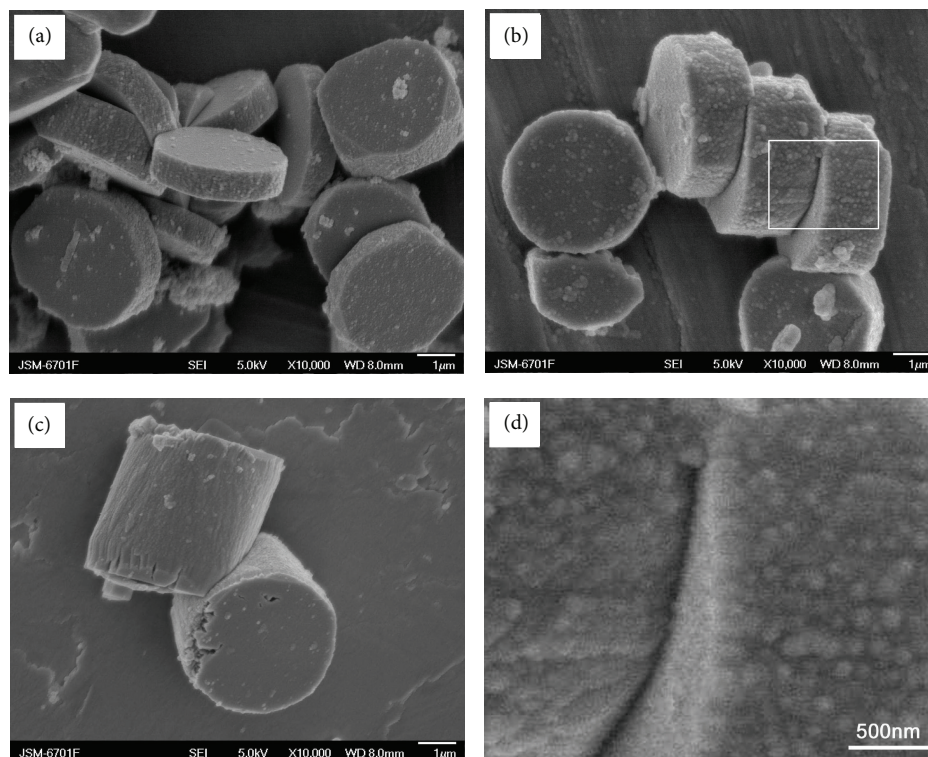


FIGURE 2: SEM images of  $\text{BiFeO}_3$  samples. (a) S-6, (b) S-9, (c) S-15, and (d) enlarged image of sample S-9.

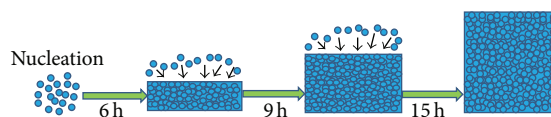


FIGURE 3: Schematic illustration of the growth mechanism for cylinder-like  $\text{BiFeO}_3$  particles.

driving force is the reduction of overall surface energy [20, 21]. At the initial stage of the self-organization, thin or disk-like microcylinders with a diameter of about  $3.7\text{--}3.8\ \mu\text{m}$  are constructed from  $\text{BiFeO}_3$  nanocrystals. With increasing the reaction time,  $\text{BiFeO}_3$  nanocrystals are continuously attracted to attach on the surface of the microcylinders, leading to their continuous growth along the height direction, whereas their diameter undergoes minor change.

Figure 4(a) shows the UV-visible diffuse reflectance spectra of  $\text{BiFeO}_3$  samples and Figure 4(b) gives the corresponding first derivative of the reflectance ( $R$ ) with respect to wavelength  $\lambda$  (i.e.,  $dR/d\lambda$ ). It is seen that the samples have a similar absorption edge at  $\sim 568\ \text{nm}$ , which is assigned to the electron transition from valence band to conduction band according to the theoretical results [22]. From the absorption edge, the bandgap energy of the samples is obtained to be  $2.18\ \text{eV}$ .

Figure 5 shows the photocatalytic degradation of AO7 over  $\text{BiFeO}_3$  samples as a function of irradiation time ( $t$ ), along with the blank experimental result. AO7 appears to be stable under simulated sunlight irradiation in the absence of photocatalyst, and its degradation percentage is less than

7% after 8 h of exposure. When  $\text{BiFeO}_3$  samples are used as the photocatalyst, the degradation of AO7 is obviously enhanced, indicating an appreciable photocatalytic activity of the samples. The degradation percentage of AO7 after 8 h irradiation with samples S-6, S-9, and S-15 is about 56%, 28%, and 19%, respectively. The sample S-6 exhibits the highest photocatalytic activity, which is mainly ascribed to its relatively small particle size. Generally small particle size and large surface area to volume ratio is required to achieve good photocatalytic activity since the photocatalytic reaction occurs dominantly on the catalyst surface [23].

Figure 6 shows the magnetic hysteresis loops of  $\text{BiFeO}_3$  samples measured at room temperature, revealing a nearly linear dependence of the magnetization on applied magnetic field. This indicates that all the samples exhibit an antiferromagnetic behavior at room temperature. It is well known that  $\text{BiFeO}_3$  has a helical antiferromagnetic spin structure with a period of  $\sim 62\ \text{nm}$  [24]. This helimagnetic structure will be destroyed in nanosized  $\text{BiFeO}_3$ , making the spin compensation incomplete. As a result, weak ferromagnetism is generally observed for nanosized  $\text{BiFeO}_3$  and exhibits an increasing trend with reducing the grain size [10, 25].

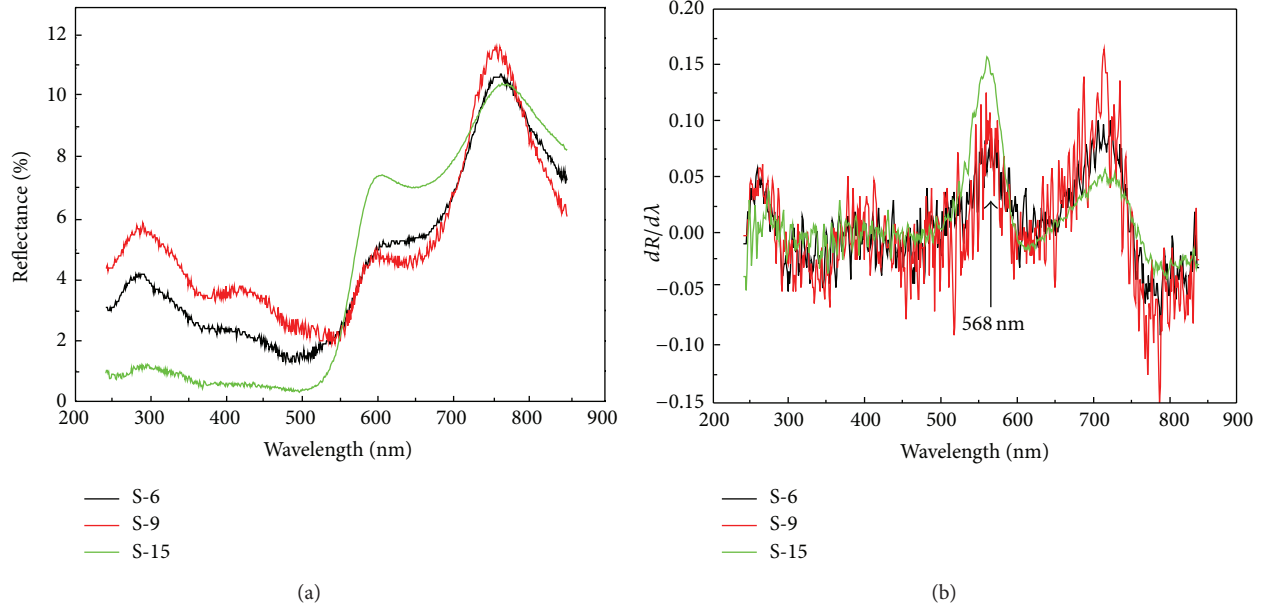


FIGURE 4: (a) UV-visible diffuse reflectance spectra of  $\text{BiFeO}_3$  samples and (b) the corresponding first derivative of the diffuse reflectance spectra.

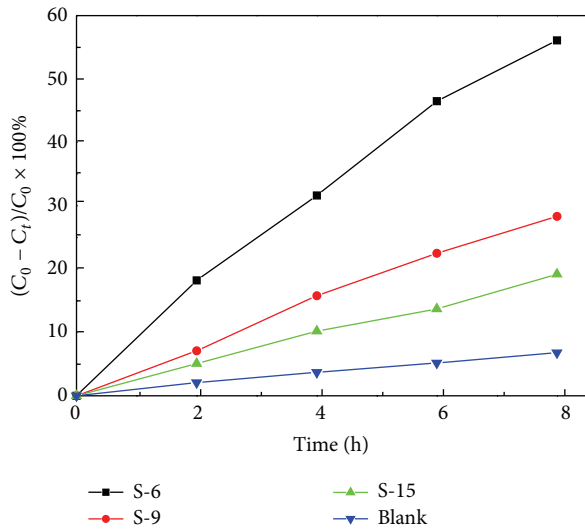


FIGURE 5: Photocatalytic degradation of AO7 over  $\text{BiFeO}_3$  samples as a function of irradiation time along with the blank experiment result.

However,  $\text{BiFeO}_3$  samples synthesized in this work crystallize in relatively large-sized microcrystals, which inhibits the observation of macroscopic magnetization.

#### 4. Conclusions

Cylinder-like  $\text{BiFeO}_3$  particles were successfully prepared by a hydrothermal method. It is found that the height of the resulted  $\text{BiFeO}_3$  microcylinders has a dependence on the hydrothermal reaction time. With prolonging the

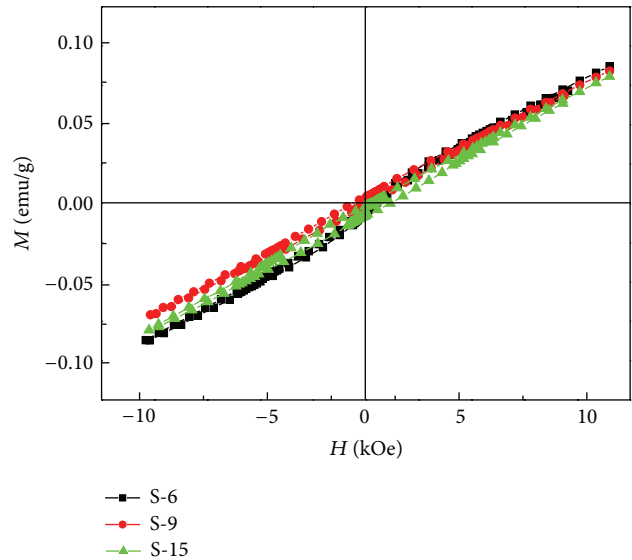


FIGURE 6: Magnetic hysteresis loops of  $\text{BiFeO}_3$  samples measured at room temperature.

reaction time from 6 to 15 h, the height of the microcylinders increases from  $\sim 0.7$  to  $\sim 4.1 \mu\text{m}$ , whereas their diameter undergoes a minor change ( $3.7\text{--}3.8 \mu\text{m}$ ). The microcylinders are constructed from sphere-like  $\text{BiFeO}_3$  nanocrystals of  $100\text{--}150 \text{ nm}$  in size. Photocatalytic experimental results demonstrate that the  $\text{BiFeO}_3$  microcylinders exhibit an appreciable photocatalytic activity toward the degradation of AO7 under simulated sunlight irradiation. Magnetic hysteresis loop measurement reveals an antiferromagnetic behavior in the  $\text{BiFeO}_3$  microcylinders at room temperature.

## Conflict of Interests

The authors declare that there is no conflict of interests regarding the publication of this paper.

## Acknowledgments

This work was supported by the National Natural Science Foundation of China (Grant nos. 51262018 and 11264023) and the Hongliu Outstanding Talents Foundation of Lanzhou University of Technology (Grant no. J201205).

## References

- [1] J. Wang, J. B. Neaton, H. Zheng et al., "Epitaxial BiFeO<sub>3</sub> multiferroic thin film heterostructures," *Science*, vol. 299, no. 5613, pp. 1719–1722, 2003.
- [2] M. Fiebig, T. Lottermoser, D. Fröhlich, A. V. Goltsev, and R. V. Pisarev, "Observation of coupled magnetic and electric domains," *Nature*, vol. 419, no. 24, pp. 818–820, 2002.
- [3] C. Tabares-Munoz, J. P. Rivera, A. Monnier, and H. Schmid, "Measurement of the quadratic magnetoelectric effect on single crystalline BiFeO<sub>3</sub>," *Japanese Journal Physics of Applied Physics*, vol. 24, no. 2, pp. 1051–1053, 1985.
- [4] P. Fischer, M. Polomska, I. Sosnowska, and M. Szymanski, "Temperature dependence of the crystal and magnetic structures of BiFeO<sub>3</sub>," *Journal of Physics C: Solid State Physics*, vol. 13, no. 10, pp. 1931–1940, 1980.
- [5] X. Lü, J. Xie, Y. Song, and J. Lin, "Surfactant-assisted hydrothermal preparation of submicrometer-sized two-dimensional BiFeO<sub>3</sub> plates and their photocatalytic activity," *Journal of Materials Science*, vol. 42, no. 16, pp. 6824–6827, 2007.
- [6] T. Soltani and M. H. Entezari, "Photolysis and photocatalysis of methylene blue by ferrite bismuth nanoparticles under sunlight irradiation," *Journal of Molecular Catalysis A: Chemical*, vol. 377, pp. 197–203, 2013.
- [7] J. Wei, C. Zhang, and Z. Xu, "Low-temperature hydrothermal synthesis of BiFeO<sub>3</sub> microcrystals and their visible-light photocatalytic activity," *Materials Research Bulletin*, vol. 47, no. 11, pp. 3513–3517, 2012.
- [8] X. Yang, Y. Zhang, G. Xu et al., "Phase and morphology evolution of bismuth ferrites via hydrothermal reaction route," *Materials Research Bulletin*, vol. 48, no. 4, pp. 1694–1699, 2013.
- [9] S. Mohan and B. Subramanian, "A strategy to fabricate bismuth ferrite (BiFeO<sub>3</sub>) nanotubes from electrospun nanofibers and their solar light-driven photocatalytic properties," *RSC Advances*, vol. 3, no. 45, pp. 23737–23744, 2013.
- [10] X. Zhang, H. Liu, B. Zheng, Y. Lin, D. Liu, and C.-W. Nan, "Photocatalytic and magnetic behaviors observed in BiFeO<sub>3</sub> nanofibers by electrospinning," *Journal of Nanomaterials*, vol. 2013, Article ID 917948, 7 pages, 2013.
- [11] T. Xian, H. Yang, J. F. Dai, Z. Q. Wei, J. Y. Ma, and W. J. Feng, "Photocatalytic properties of BiFeO<sub>3</sub> nanoparticles with different sizes," *Materials Letters*, vol. 65, no. 11, pp. 1573–1575, 2011.
- [12] X. Chen, Y. Tang, L. Fang, H. Zhang, C. Hu, and H. Zhou, "Self-assembly growth of flower-like BiFeO<sub>3</sub> powders at low temperature," *Journal of Materials Science: Materials in Electronics*, vol. 23, no. 8, pp. 1500–1503, 2012.
- [13] H. Zheng, X. Liu, C. Diao, Y. Gu, and W. Zhang, "A separation mechanism of photogenerated charges and magnetic properties for BiFeO<sub>3</sub> microspheres synthesized by a facile hydrothermal method," *Physical Chemistry Chemical Physics*, vol. 14, no. 23, pp. 8376–8381, 2012.
- [14] L. Zhang, X.-F. Cao, Y.-L. Ma, X.-T. Chen, and Z.-L. Xue, "Polymer-directed synthesis and magnetic property of nanoparticles-assembled BiFeO<sub>3</sub> microrods," *Journal of Solid State Chemistry*, vol. 183, no. 8, pp. 1761–1766, 2010.
- [15] H.-Y. Si, W.-L. Lu, J.-S. Chen, G.-M. Chow, X. Sun, and J. Zhao, "Hydrothermal epitaxial multiferroic BiFeO<sub>3</sub> thick film by addition of the PVA," *Journal of Alloys and Compounds*, vol. 577, no. 15, pp. 44–48, 2013.
- [16] L. J. Di, H. Yang, T. Xian, R. S. Li, Y. C. Feng, and W. J. Feng, "Influence of precursor Bi<sup>3+</sup>/Fe<sup>3+</sup> ion concentration on hydrothermal synthesis of BiFeO<sub>3</sub> crystallites," *Ceramics International*, vol. 40, no. 3, pp. 4575–4578, 2014.
- [17] M. Muneeswaran, P. Jegatheesan, and N. V. Giridharan, "Synthesis of nanosized BiFeO<sub>3</sub> powders by co-precipitation method," *Journal of Experimental Nanoscience*, vol. 8, no. 3, pp. 341–346, 2013.
- [18] A. Perejón, N. Murafa, P. E. Sánchez-Jiménez et al., "Direct mechano-synthesis of pure BiFeO<sub>3</sub> perovskite nanoparticles: reaction mechanism," *Journal of Materials Chemistry C*, vol. 1, no. 22, pp. 3551–3562, 2013.
- [19] A. Hernández-Ramírez, A. Martínez-Luévanos, A. F. Fuentes, A.-G. D. Nelson, R. C. Ewing, and S. M. Montemayor, "Molten salts activated by high-energy milling: a useful, low-temperature route for the synthesis of multiferroic compounds," *Journal of Alloys and Compounds*, vol. 584, no. 25, pp. 93–100, 2014.
- [20] R. L. Penn, G. Oskam, T. J. Strathmann, P. C. Searson, A. T. Stone, and D. R. Veblen, "Epitaxial assembly in aged colloids," *The Journal of Physical Chemistry B*, vol. 105, no. 11, pp. 2177–2182, 2001.
- [21] R. L. Penn and J. F. Banfield, "Imperfect oriented attachment: dislocation generation in defect-free nanocrystals," *Science*, vol. 281, no. 5379, pp. 969–971, 1998.
- [22] S. J. Clark and J. Robertson, "Band gap and Schottky barrier heights of multiferroic BiFeO<sub>3</sub>," *Applied Physics Letters*, vol. 90, no. 1–3, Article ID 132903, 2007.
- [23] Z. Zhang, C.-C. Wang, R. Zakaria, and J. Y. Ying, "Role of particle size in nanocrystalline TiO<sub>2</sub>-based photocatalysts," *Journal of Physical Chemistry B*, vol. 102, no. 52, pp. 10871–10878, 1998.
- [24] I. Sosnowska, T. P. Neumaier, and E. Steichele, "Spiral magnetic ordering in bismuth ferrite," *Journal of Physics C: Solid State Physics*, vol. 15, no. 23, pp. 4835–4846, 1982.
- [25] T.-J. Park, G. C. Papaefthymiou, A. J. Viescas, A. R. Moodenbaugh, and S. S. Wong, "Size-dependent magnetic properties of single-crystalline multiferroic BiFeO<sub>3</sub> nanoparticles," *Nano Letters*, vol. 7, no. 3, pp. 766–772, 2007.

## Review Article

# Fabrication, Characterization, Properties, and Applications of Low-Dimensional BiFeO<sub>3</sub> Nanostructures

Heng Wu, Jun Zhou, Lizhi Liang, Lei Li, and Xinhua Zhu

National Laboratory of Solid State Microstructures, School of Physics, Nanjing University, Nanjing 210093, China

Correspondence should be addressed to Xinhua Zhu; xhzhu1967@aliyun.com

Received 25 April 2014; Revised 25 June 2014; Accepted 25 June 2014; Published 25 August 2014

Academic Editor: Seungbum Hong

Copyright © 2014 Heng Wu et al. This is an open access article distributed under the Creative Commons Attribution License, which permits unrestricted use, distribution, and reproduction in any medium, provided the original work is properly cited.

Low-dimensional BiFeO<sub>3</sub> nanostructures (e.g., nanocrystals, nanowires, nanotubes, and nanoislands) have received considerable attention due to their novel size-dependent properties and outstanding multiferroic properties at room temperature. In recent years, much progress has been made both in fabrications and (microstructural, electrical, and magnetic) in characterizations of BiFeO<sub>3</sub> low-dimensional nanostructures. An overview of the state of art in BiFeO<sub>3</sub> low-dimensional nanostructures is presented. First, we review the fabrications of high-quality BiFeO<sub>3</sub> low-dimensional nanostructures *via* a variety of techniques, and then the structural characterizations and physical properties of the BiFeO<sub>3</sub> low-dimensional nanostructures are summarized. Their potential applications in the next-generation magnetoelectric random access memories and photovoltaic devices are also discussed. Finally, we conclude this review by providing our perspectives to the future researches of BiFeO<sub>3</sub> low-dimensional nanostructures and some key problems are also outlined.

## 1. Introduction

Multiferroics are formally defined as materials that exhibit more than one primary ferroic order parameter simultaneously [1, 2]. The coupling of different order parameters such as magnetoelectric coupling reveals the mutual regulation of magnetic and electric field which has potentially enormous commercial value in the next generation of information technology areas (e.g., multistate storage) [3–7]. Among the single-phase multiferroics, BiFeO<sub>3</sub> (BFO) has high Curie temperature ( $T_C = 850^\circ\text{C}$ ), high Neel temperature ( $T_N = 370^\circ\text{C}$ ), and large residual polarization intensity ( $150 \mu\text{C}/\text{cm}^2$ ) at room temperature, which is widely investigated as model system of single-phase multiferroics. However, as one kind of G-type antiferromagnetic material BFO has spiral spin structure with a periodicity of 62 nm, this weak linear magnetoelectric coupling makes it hard to be used in multifunctional devices [8]. Recently, it is found that the BFO nanoparticles exhibit relatively strong ferromagnetism as their sizes are below 62 nm [9]. Therefore, an enhanced magnetoelectric coupling can be achieved in the nanosized BFO materials, which play an important role in microelectronic

devices [10–12]. Recent advances in science and technology of semiconductor integrated circuit have resulted in the feature sizes of microelectronic devices downscaling into nanoscale dimensions. At nanoscale the BFO materials display novel physical properties that are different from their bulk and film counterparts. Understanding the size effects of the BFO materials at nanoscale is of importance for developing the next generation of revolutionary electronic nanodevices. Due to the size effects being dependent on the structure and finite size, considerable efforts have been made in the controllable synthesis of low-dimensional BFO nanostructures such as nanowires, nanotubes, and their arrays. Much progress has also been achieved in the structure and property characterization. Furthermore, BFO nanostructures are also received extensive attention in the study of heterostructures [13] and domain characterizations [14–16]. This paper provides an overview of recent advances on the fabrication, structural characterization, and physical properties of low-dimensional BFO nanosized materials. Their potential applications are also discussed and some problems that need to be solved in future researches are also pointed out.

## 2. Fabrication of Low-Dimensional BFO Nanostructures

Generally, nanostructured materials can be classified into four classes by their dimensions, which are zero-dimensional (0D) structures such as nanoparticles, one-dimensional (1D) materials such as nanowires, nanorods, and nanotubes, two-dimensional (2D) materials such as thin film and nanoislands, and three-dimensional (3D) materials such as nanowires/tubes arrays, respectively. Up to date, two different approaches have been developed to fabricate nanostructured BFO, one is the bottom-up approach which means synthesizing nanostructures from atoms or molecules by assembling tiny into large, the other one is top-down approach which means dividing, etching or carving thin film or bulk materials into nanostructures as cutting big into small. In this section, we introduce the most used techniques for fabrication of low-dimensional BFO nanostructures and discuss their differences.

**2.1. Sol-Gel Process.** Sol-gel process is a kind of bottom-up approach, which generally involves the use of metal alkoxides and undergoes hydrolysis and condensation polymerization reactions to produce gels. After annealing the gels transform the porous gels into a dense target product. The main processing factors of sol-gel process are the water ratio in solution, pH value of solution, and its temperature. To synthesize BFO nanoparticles by sol-gel process,  $\text{Bi}(\text{NO}_3)_3 \cdot 5\text{H}_2\text{O}$  and  $\text{Fe}(\text{NO}_3)_3 \cdot 9\text{H}_2\text{O}$  are normally used as the raw materials. For example, Kim et al. [17] synthesized the BFO powders (average sizes  $\sim 200$  nm) by dissolving  $\text{Bi}(\text{NO}_3)_3 \cdot 5\text{H}_2\text{O}$  into the mixture of 2-methoxyethanol and acetic acid, and as the solution became transparent they dissolved  $\text{Fe}(\text{NO}_3)_3 \cdot 9\text{H}_2\text{O}$  in it and kept the mixture at room temperature with stirring. Then, the precursor solution was dried at  $80^\circ\text{C}$  for about 12 h to obtain the BFO xerogel powder. They grinded the xerogel powders and annealed them at  $600^\circ\text{C}$  in air or  $\text{N}_2$  atmosphere to obtain the BFO nanosized powders. Gao et al. [18] dissolved the  $\text{Bi}(\text{NO}_3)_3 \cdot 5\text{H}_2\text{O}$  and  $\text{Fe}(\text{NO}_3)_3 \cdot 9\text{H}_2\text{O}$  with stoichiometric proportions into 2-methoxyethanol and adjusted the solution pH value to 4-5 by adding nitric acid subsequently. Then citric acid in 1:1 molar ratio with the metal nitrates and polyethylene glycol as a dispersant was added into the solution, respectively. After stirring the solution at  $50^\circ\text{C}$  for 0.5 h, the solution was kept at  $80^\circ\text{C}$  for 4 days to obtain the dried gel. After calcination at  $500^\circ\text{C}$  for 2 h perovskite-type BFO nanoparticles with average diameter of  $\sim 80$ – $120$  nm were obtained. Similarly, Park et al. [9] also employed the sol-gel process to synthesize single-crystalline BFO nanoparticles and tuned their sizes from less than 15 nm to  $\sim 100$  nm by changing the annealing temperatures. Obviously, the sizes of BFO nanoparticle were increased with the annealing temperature. However, the ideal synthetic pathway for the BFO nanoparticles is to obtain the appropriate size, shape, and crystallinity in the absence of the additional postannealing steps. Therefore, modified sol-gel techniques are developed to synthesize the BFO nanoparticles. Among them, hydrothermal method is one of the examples, in which there is no necessity for high-temperature calcination.

**2.2. Hydrothermal Method.** Hydrothermal method is also called the autoclave method, which involves heating an aqueous suspension of insoluble salts in an autoclave at a moderate temperature and pressure so that the crystallization of a desired phase will take place. The hydrothermal method is very popular method for synthesizing the perovskite nanoparticles because the synergetic effects from solvent, temperature, and pressure can offer stable final products and prevent the formation of impurity phases. The hydrothermal method is used to synthesize the BFO nanoparticles. For example, Chen et al. [19] utilized  $\text{Bi}(\text{NO}_3)_3 \cdot 5\text{H}_2\text{O}$  and  $\text{Fe}(\text{NO}_3)_3 \cdot 9\text{H}_2\text{O}$  as raw materials and adjusted the concentration of KOH at the region 1 M to 9 M to synthesize BFO nanoparticles with different morphologies at  $200^\circ\text{C}$  for 6 h. Han et al. [20] used  $\text{Bi}(\text{NO}_3)_3 \cdot 5\text{H}_2\text{O}$ ,  $\text{Fe}(\text{NO}_3)_3 \cdot 9\text{H}_2\text{O}$  and 8 M KOH to synthesize pure BFO powders at the temperatures of  $175$ – $225^\circ\text{C}$  and the hold time of 6 h, respectively. Wang et al. [21] used  $\text{Bi}(\text{NO}_3)_3 \cdot 5\text{H}_2\text{O}$  and  $\text{Fe}(\text{NO}_3)_3 \cdot 9\text{H}_2\text{O}$  as raw materials and synthesized the different morphologies of BFO nanoparticles by adding  $\text{KNO}_3$  mineralizer or not. All the above results demonstrate that the concentration of KOH determines the phase structure of the synthesized products. The pure BFO nanoparticles with diameters of 100–300 nm were synthesized when the concentration of KOH was 7 M and 12 M. If the concentration of KOH was below, the synthesized products were mainly composed of perovskite-type BFO accompanied with impurity phase of orthorhombic-type  $\text{Bi}_2\text{Fe}_4\text{O}_9$ . In hydrothermal procedure, the growth rate of  $\text{BiFeO}_3$  was decreased by adding the  $\text{KNO}_3$  mineralizer, and thin plate-like  $\text{BiFeO}_3$  could be obtained as increasing the reaction time.

In addition, the solvothermal method is also a popular method to synthesize the BFO nanomaterials, which is similar to the hydrothermal method. The only difference is that the precursor solution for a solvothermal method is usually an organic medium such as ethanol or acetone, while that for a hydrothermal method is usually an aqueous medium such as water. Liu et al. [22] employed solvothermal method to synthesize single-crystalline BFO nanowires (45–200 nm in diameter, several nanometers to several micrometers in length) in acetone solvent. They dissolved  $\text{Bi}(\text{NO}_3)_3 \cdot 5\text{H}_2\text{O}$  and  $\text{Fe}(\text{NO}_3)_3 \cdot 9\text{H}_2\text{O}$  in 1:1 molar ratio then added deionized water and stronger ammonia water to adjust pH value of the solution to 10–11. After washing the sediment by distilled water until it is neutral, 5 M NaOH was added and kept stirring for 30 min. Then they heated the solution at  $180^\circ\text{C}$  for 72 h and obtained the single-crystalline BFO nanowires.

Moreover, the morphology of the final products derived from solvothermal method can be effectively controlled by selecting the types of organics and their amount. For example, Zhang et al. [23] synthesized BFO nanoparticles and nanowires assembled by nanoparticles via changing the amount of the PVP or PEG (polyethylene glycol) polymer.

**2.3. Template Method.** Template method is based on chemical self-organization to synthesize nanostructured materials by the assistance of template which is porous with nanosized pores. By electrochemical deposition, sol-gel or chemical vapor deposition technology, atoms, or ions are deposited on

TABLE 1: Summary of various approaches for fabricating the BFO low-dimensional nanostructures.

Approaches	Advantages	Disadvantages	Structures
Bottom-up			
Sol-gel	Facile regulation Low reaction temperature	Long reaction time	Nanoparticle
Template	Easy process uniform size and array	Limited aspect ratio	Nanowire/tube
Hydrothermal	Easy process high crystallinity low reaction temperature	Harsh reaction condition	Nanoparticle/wire
Top-down			
FIB	High resolution uniform size and array	Surface damage low throughput	Nanoisland/array

the tube walls and form the nanostructure. Template method can be employed to fabricate one-dimensioned materials which have well dispersion and are easy to adjust aspect ratio of nanowires, tubes, and rods by changing the structural parameters of the used templates. Since the nanostructures fabricated by template method have similar structural properties (e.g., sizes, shape) to the templates, therefore, the pore sizes and their aspect ratios of the templates are crucial parameters for controlling the dimensions of the final nanostructures. Park et al. [24] first reported on the synthesis of BFO nanotubes by using porous anodic alumina (AAO) templates with pore-size of 100 or 200 nm. They dissolved  $\text{Bi}(\text{NO}_3)_3 \cdot 5\text{H}_2\text{O}$  and  $\text{Fe}(\text{NO}_3)_3 \cdot 9\text{H}_2\text{O}$  with a molar ratio of 1:1 to ethylene glycol and deposited the sol onto the surface of the AAO template by using a syringe. Finally they obtained BFO nanotubes with outer diameters in the range of 240 to 300 nm (for 200 nm pore-sized template) or 140 to 180 nm (for 100 nm pore-sized template) and lengths ranging from several microns to as much as 50  $\mu\text{m}$ . However, the synthesized BFO nanotubes are polycrystalline because of the random nucleation on the walls of pores. Zhang et al. [25] also employed the similar method to synthesize BFO nanowires array *via* injecting the sol on the template and annealed it subsequently. Gao et al. [26] synthesized polycrystalline BFO nanowires with a diameter of 50 nm and 5  $\mu\text{m}$  in length by the similar method.

Synthesis of the BFO nanostructures by template method provides some advantages such as the structure of the nanoarray subject to the structure of the template, the channels of the template controlling the dimension of the materials, template pore walls preventing the aggregation of the material, and a large amount of nanowires or nanotubes mass produced.

**2.4. Focus Ion Beam (FIB) Milling Method.** The common top-down approach to fabricate nanostructured materials is focused ion beam (FIB) milling method. The typical technology is to utilize focused  $\text{Ga}^+$  ions to bombard the thin film or bulk material to obtain the designed nanostructures. The advantages of FIB milling method are controllable morphology of structure or even patterns, facile operation and, and so forth. However, the disadvantages are high cost and the

resolution of FIB is micron or submicron scale which is larger than the nanostructure.

Recently, Morelli et al. [27] fabricated BFO nanoislands by template-assisted FIB method based on epitaxial BFO thin films grown on  $\text{SrTiO}_3$  (100) substrates. Arrays of 45 nm-thick aluminium dots were first evaporated on BFO thin films through template with aperture diameter of 400 nm. A focused ion beam with gallium ions was used to mill the specimen covered by Al dots. Chemical etching of the remaining Al was performed in 10% aqueous solution of potassium hydroxide (KOH) at room temperature for 90 s. Arrays of epitaxial BFO nanoislands with diameter  $\sim 250$  nm were obtained. The features of top-down approaches are their precisely positioning and controlling the shapes and sizes of the designed BFO nanostructures. However, their time-consuming and low-throughput characters of these processes are the shortcomings of the top-down approaches.

Table 1 summarizes various approaches for fabricating the BFO low-dimensional nanostructures.

### 3. Characterization of BFO Nanostructures

Up to date various approaches including X-ray diffraction (XRD), scanning electron microscopy (SEM), (high-resolution) scanning transmission electron microscopy (HR) STEM, as well as X-ray energy dispersive spectrum (EDS), electron energy loss spectra (EELS), and selected area electron diffraction (SAED) have been developed to probe both the macroscopic and the microscopic details of BFO low-dimensional nanostructures. In this section, we will briefly summarize the recent the atomic-scale microstructural features of BFO low-dimensional nanostructures revealed a number of techniques.

**3.1. BFO Nanoparticles/Nanoislands.** Park et al. [9] first reported the synthesis of pure crystalline BFO nanoparticles by sol-gel method. Figure 1 shows the structural characterizations of BFO nanoparticles with the average diameter of 95 nm by techniques of TEM, SAED, EDS, and HRTEM. Zhu et al. [28] also reported on the microwave-hydrothermal synthesis of spherical BFO nanoparticles, their TEM and

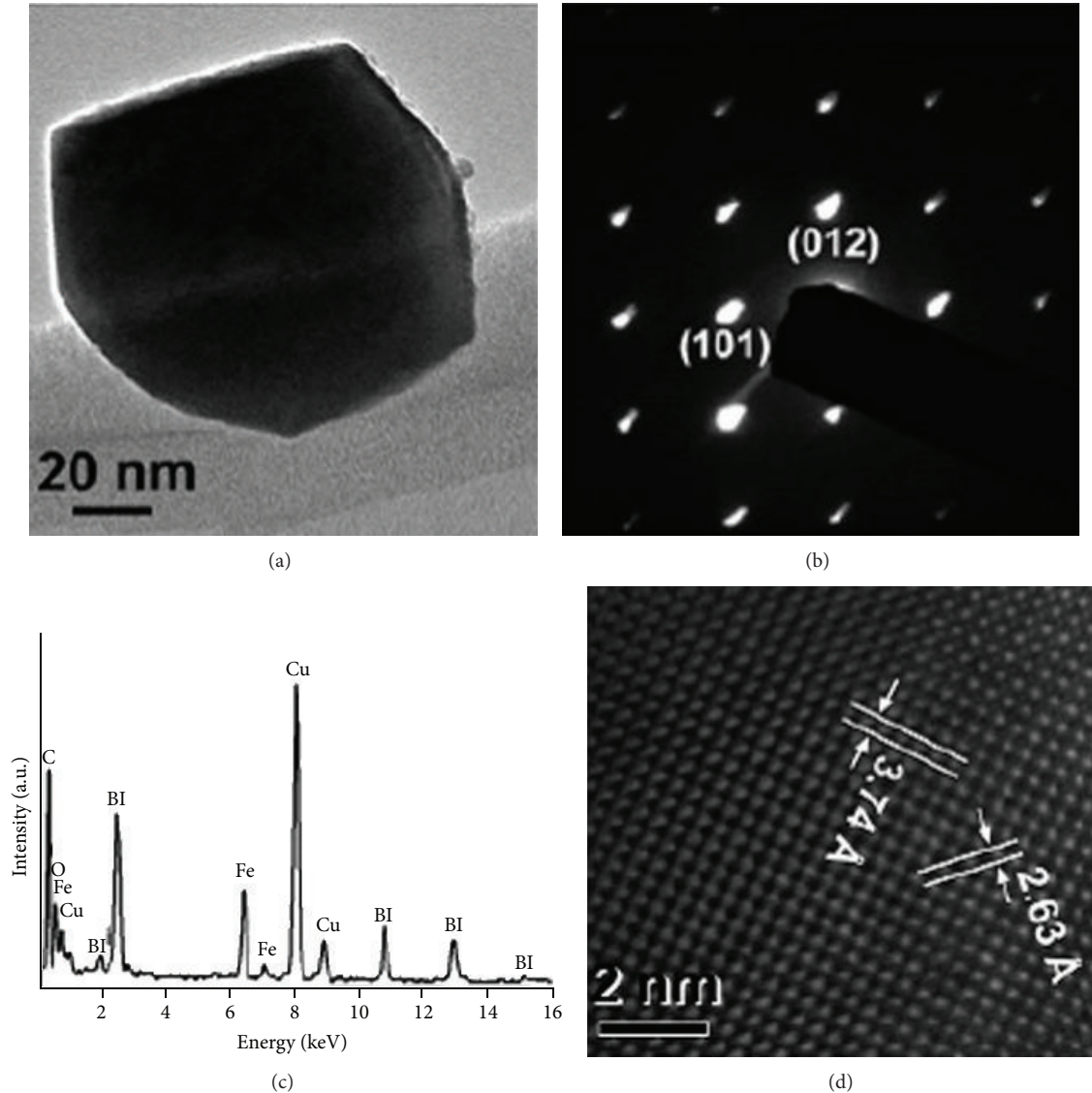


FIGURE 1: (a) TEM image, (b) SAED pattern, (c) EDS, and (d) HRTEM image of an individual  $\text{BiFeO}_3$  nanoparticle (with a diameter of 95 nm) synthesized by sol-gel method.

HRTEM images are shown in Figure 2. The HRTEM pattern demonstrates the well crystallization of as-prepared BFO nanocrystals.

Besides the BFO nanoparticles, epitaxial BFO nanoislands were also synthesized by chemical self-assembled method [29], their phase structure and morphology were characterized by XRD and atomic force microscopy (AFM). Figure 3 shows the XRD patterns of the BFO nanoislands annealed at different temperatures; there is almost no other impurity peaks except the diffraction peaks of single crystalline  $\text{SrTiO}_3$  substrate and the (100) crystal orientation of BFO. The AFM images shown in Figure 4 revealed that with increasing the postannealing temperature from  $600^\circ\text{C}$  to  $800^\circ\text{C}$ , the morphology of BFO nanoislands in the (100) growth plane evolved from triangled to squared, and then to plated shapes. Fractal ferroelectric domains and self-bias polarization were also found in a single BFO

nanoisland, which were revealed by piezoforce microscopy (PFM) images.

Zhou et al. [30] also fabricated the BFO nanoring structure by combing sol-gel, AAO template-assisted, and planar TEM sample preparation methodology. Figure 5(a) shows the STEM image of the nanorings, where the atoms with high atomic numbers (such as Bi, Fe) exhibit bright image contrast; therefore, the BFO nanorings demonstrate high white bright contrast. Figure 5(b) shows the line scan of the intensity distribution of the STEM image contrast of the BFO nanorings, from which the inner diameter of the nanoring was determined to be about 170 nm and its thickness was about 20 nm. Therefore, the BFO nanorings were formed in the walls of the AAO template. The EDS data reveal that the BFO nanorings are composed of Bi, Fe, and O elements and that the chemical composition of the nanorings is close to  $\text{BiFeO}_3$ .

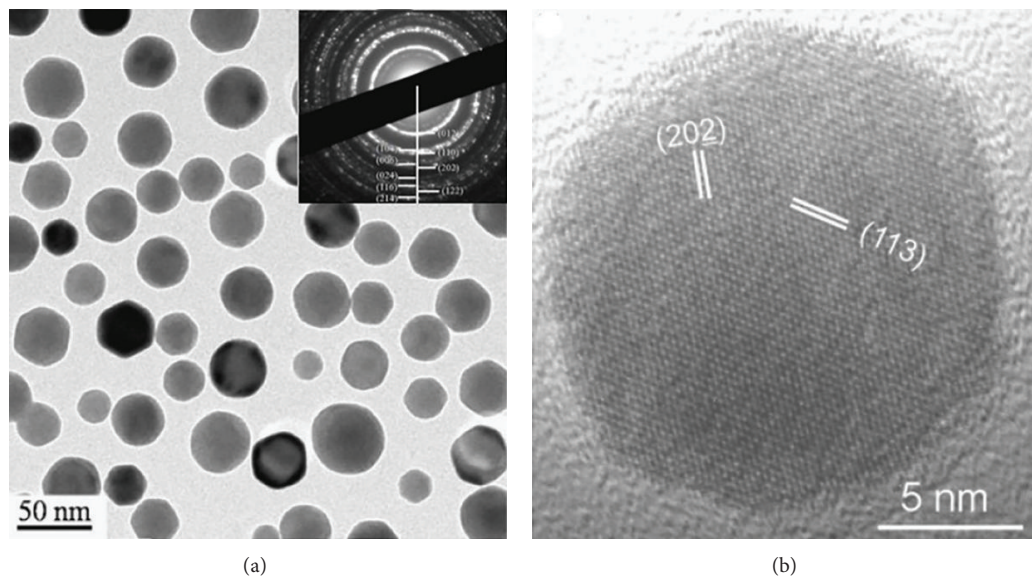


FIGURE 2: (a) TEM image of  $\text{BiFeO}_3$  nanocrystals and the inset is selected area electron diffraction pattern, (b) HRTEM image of a single  $\text{BiFeO}_3$  nanocrystal with a diameter of  $\sim 12$  nm.

**3.2. One-Dimensional BFO Nanostructures and Their Arrays.** Zhang et al. [25, 31] fabricated the BFO nanowire and nanotube arrays by a template synthesis involving the sol-gel technique. Figure 6 shows the SEM images of the BFO nanowire and nanotube arrays, respectively. The TEM image of a single BFO nanotube is shown in Figure 6(c); the corresponding SAED pattern and the EDX spectrum are shown as insets.

**3.3. Domain Structures of BFO Thin Films.** Chu et al. [32] characterized the ferroelectric polarization direction and domain structures of BFO films with different thicknesses (120, 15, and 2 nm) grown on  $\text{SrTiO}_3$  (001) (top) and  $\text{DySrO}_3$  (110) substrates (bottom) by PFM. Due to the competition between the normal strain caused by lattice mismatch and shear strain caused by the rhombohedral symmetry, ferroelectric polarization direction and domain structures are changed with the decrease of the film thickness, as shown in Figure 7. With decreasing the thickness of BFO films deposited on  $\text{SrTiO}_3$  (001), the domain morphology evolved from stripe domain structures (Figure 7(a)) to intricate domain structures with fluctuate mottled contrast (Figures 7(b) and 7(c)). However, the domain size became larger as decreasing the thickness of BFO films deposited on  $\text{DySrO}_3$  (110) substrates. Such a difference arises from the normal strain since it cannot be released at such thicknesses; therefore, BFO films on  $\text{SrTiO}_3$  have larger elastic strain energy, which leads to smaller domain structures.

## 4. Physical Properties of Low-Dimensional BFO Nanostructures

**4.1. BFO Nanoparticles.** Park et al. [9] synthesized the BFO nanoparticles by sol-gel method and investigated the size-driven magnetism of the BFO nanoparticles, as shown in

Figure 8. As the sizes of the BFO nanoparticles were reduced, their magnetism was significantly enhanced. Especially, when the particle size was 14 nm, the magnetization was about 3 times larger than that of the BFO particle with size of 100 nm. This is important for enhancing the magnetic properties of the BFO nanoparticles with antiferromagnetic ground state.

Recently it is reported that low-dimensional nanostructured BFO such as nanoparticles and nanowires exhibit good photocatalytic activities in visible-light region. As a novel visible-light-responsive photocatalysts for degradation of organic compounds BFO nanostructures have been widely investigated. For example, Zhu et al. [28] reported the microwave-hydrothermal synthesis of spherical perovskite-type BFO nanocrystals with diameters of 10–50 nm and hexagonal-shaped sillenite-type ones with sizes of 18–33 nm at low temperatures. They found that the sillenite-type bismuth ferritic nanocrystals exhibit higher photocatalytic ability than the perovskite-type ones, which was ascribed to their small mean particle sizes and the unique hexagonal-shape morphology, and also the structural characteristics of sillenite-type compound. Gao et al. [18] also reported visible-light photocatalytic property of BFO nanocrystals. As compared with the traditional  $\text{TiO}_2$ -based photocatalysts, which are the only response to UV irradiation due to its large band gap (3.2 eV), the BFO nanocrystals exhibit their obvious advantage making use of the visible-light due to their small band gaps. This is invaluable in increasing the photocatalytic reaction by using the visible sunlight.

**4.2. BFO Nanoislands.** Up to date, much work about the low-dimensional BFO nanostructures is mainly focused on the BFO nanoparticles (0D) and nanofilms (2D), and little work is reported on the BFO nanoislands. Geometrically, BFO nanoislands are a class of systems that bridge the gap between the BFO nanoparticles and BFO ultrathin films. Compared

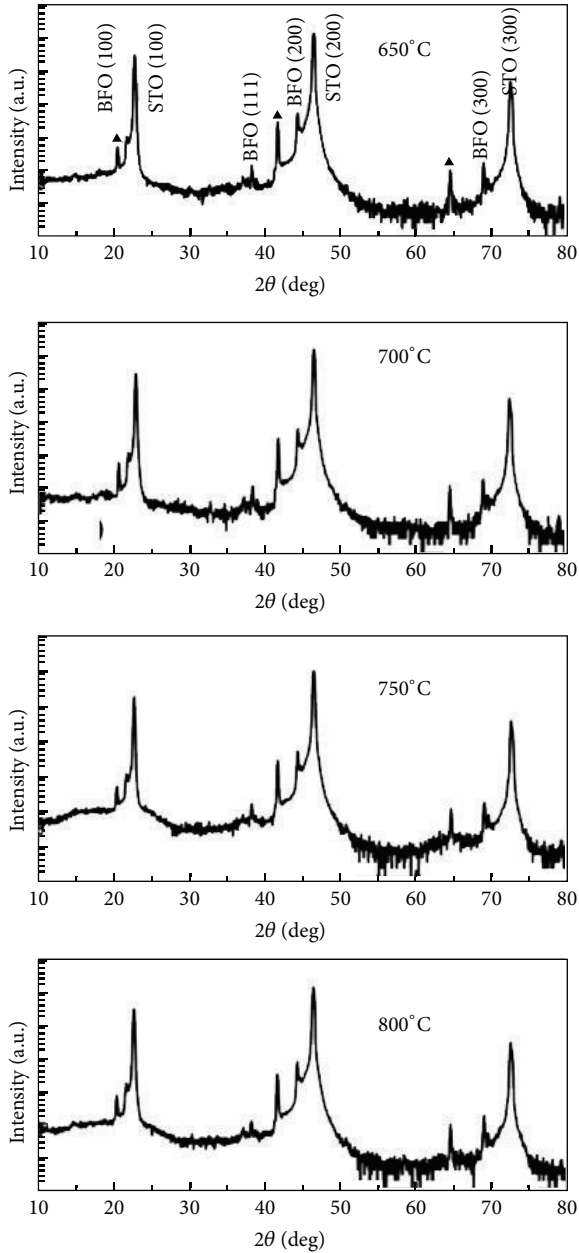


FIGURE 3: XRD patterns of the epitaxial  $\text{BiFeO}_3$  nanoislands fabricated on  $\text{SrTiO}_3$  (100) single crystal substrates by chemical assembled method, and postannealed at  $650^\circ\text{C}$ ;  $700^\circ\text{C}$ ;  $750^\circ\text{C}$ ; and  $800^\circ\text{C}$  for 1 hour. The diffraction peaks labeled by  $\blacktriangle$  were from the  $\text{SrTiO}_3$  (100) single crystal substrates diffracted by the  $\text{Cu-K}\beta$  line due to the remaining  $\text{Cu-K}\beta$  radiation.

with BFO thin films, they have free-standing sidewalls that tend to suppress the formation of a nonuniform in-plane polarization due to the appearance of depolarizing field, similar to the ferromagnetic particles. On the other hand, relative to the (confined in all three dimensions) nanoparticles, the BFO nanoislands have large aspect ratio and likely to behave similarly to thin films when the polarization is out of plane. Therefore, it is expected that multiferroic BFO nanoislands should exhibit some kind of a “particle-to-thin

film” crossover behavior and related novel effects depending on the aspect ratio and the type of bulk polarization ordering. Furthermore, due to the geometrical similarity between the multiferroic BFO nanoislands and microelectronic devices based on the multiferroic BFO nanomaterials, it is useful for simulating working conditions of real microelectronic devices [33, 34].

Recently, Hang et al. [29] reported the epitaxial growth of multiferroic BFO nanoislands on  $\text{SrTiO}_3$  (100) and Nb-doped  $\text{SrTiO}_3$  (100) single crystal substrates by chemical self-assembled method. By this method, they synthesized the epitaxial multiferroic BFO nanoislands *via* postannealing process in the temperature range of  $650\text{--}800^\circ\text{C}$ , and the lateral sizes of the BFO nanoislands were in the range of 50–160 nm and height of 6–12 nm. With increasing the postannealing temperature, the morphology of the BFO nanoislands in the (100) growth plane evolved from triangled to squared, and then to plated shapes. Ferroelectric characteristics of a single epitaxial BFO nanoisland (with lateral size of  $\sim 50$  nm and height of 12 nm) grown on Nb-doped  $\text{SrTiO}_3$  (100) single crystal substrate was characterized by PFM images. The results demonstrated that fractal ferroelectric domains existed in the single BFO nanoisland, and self-biased polarization was also observed within this multiferroic nanoisland. This phenomenon can be ascribed to the interfacial stress caused by the lattice misfit between the BFO nanoisland and the  $\text{SrTiO}_3$  single crystal substrate.

By using the top-down approach such as FIB milling method, Morelli et al. [27] fabricated the arrays of epitaxial BFO islands with flat top surfaces and lateral sizes down to 250 nm by starting from a continuous BFO thin film. PFM images showed that the as-fabricated BFO nanoislands preserved ferroelectric properties with switchable polarization and exhibited retention of polarization state at least for several days. As compared with the parent thin film, the BFO nanoislands exhibit a certain degree of imprint behavior, as shown in Figure 9. That is due to the existence of the defects at the interface between the BFO film and  $\text{SrRuO}_3$  substrate, and on the sidewalls of the islands.

**4.3. BFO Nanowires, Nanotubes, and Their Arrays.** In the last decade low-dimensional BFO nanostructures have received much attention because of their superior physical and chemical properties. Among them, BFO nanowires and nanotubes are especially attractive for nanoscience studies and nanotechnology applications, which are ascribed to that the BFO nanowires and/or nanotubes are not only used as the building blocks of future nanodevices, but also offer fundamental scientific opportunities for investigating the intrinsic size effects of physical properties.

Nowadays BFO nanowires, nanorods, nanotubes, and their arrays have been fabricated by the template-aided synthesis. However, all the products prepared by this method exhibit polycrystalline structures due to the heterogeneous nucleation on the pore walls; there are very few reports on the synthesis of single crystalline nanowires through this method. To better understand the intrinsic size effects of physical properties, high quality of one-dimensional single crystalline BFO nanowires is highly required. Recently,

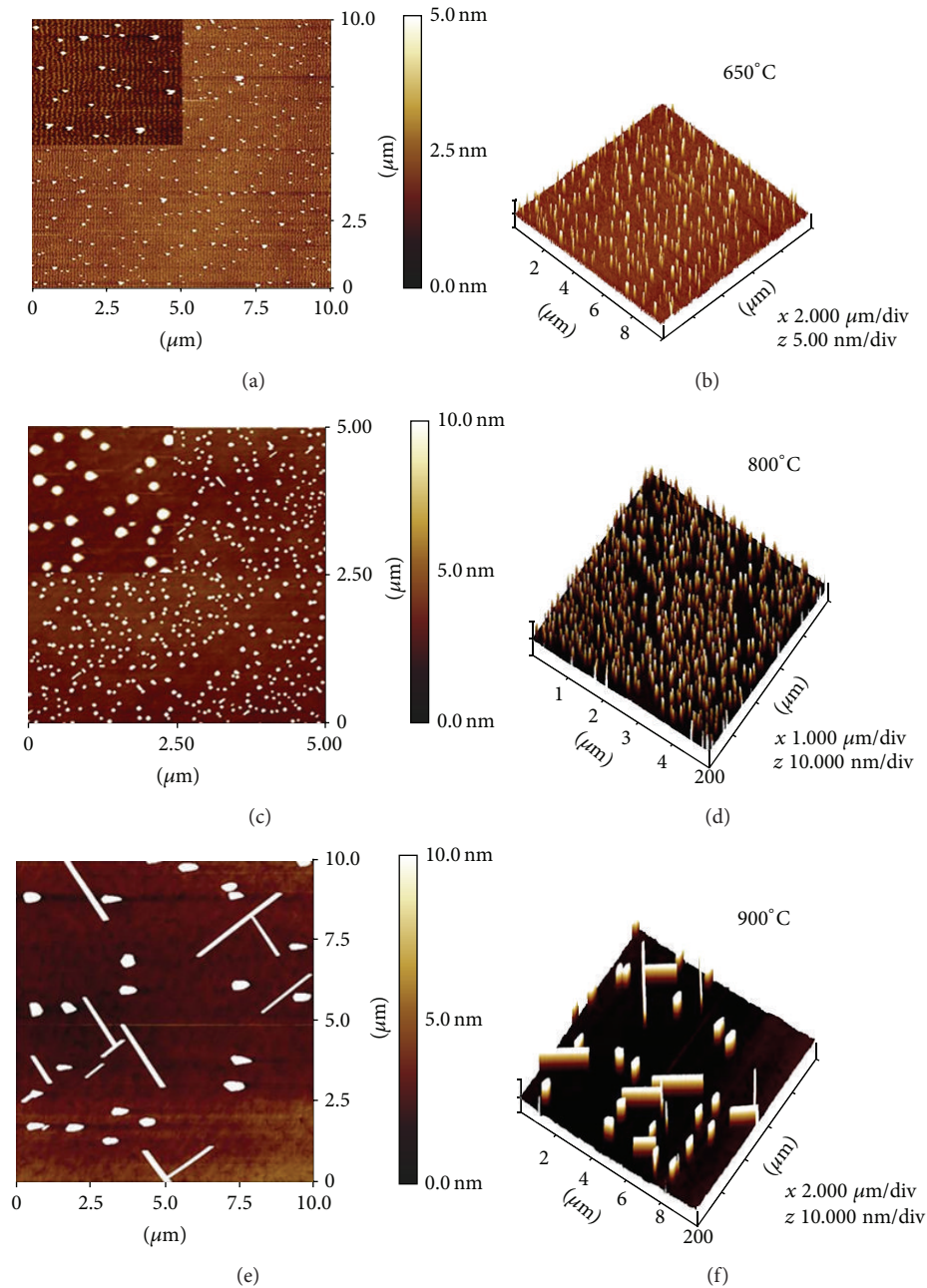


FIGURE 4: AFM images of the epitaxial  $\text{BiFeO}_3$  nanoislands postannealed at ((a), (b))  $650^\circ\text{C}$ , ((c), (d)):  $800^\circ\text{C}$ , ((e), (f)):  $900^\circ\text{C}$  for 1 h. The left AFM images are two-dimensional ones and the right ones are the corresponding 3-dimensional ones. The insets in (a) and (c) are the enlarged AFM images of the local surface areas.

Liu et al. [22] reported the synthesis of single-crystalline BFO nanowires (45–200 nm in diameter) by solvothermal method and measured their magnetic properties by superconducting quantum interference device (SQUID) at room temperature and low temperatures, as shown in Figure 10. Li et al. [35] also synthesized the BFO nanowires by solvothermal method (40–200 nm in diameter and several micrometers in length) and characterized a single BFO nanowire by PFM. The results shows the  $x$  and  $z$ -PFM hysteresis loops which clearly reveals the ferroelectric property of a single BFO nanowire.

The BFO nanowire (with diameter of 20 nm) arrays are also fabricated by template-assisted sol-gel technique [36]. Their ferroelectric and dielectric properties are demonstrated in Figure 11. Figure 11(a) shows the polarization of BFO nanowire arrays as a function of applied electric field about  $600\text{ kV/cm}$  with a frequency ( $\nu$ ) = 10 kHz at room temperature. The observed P-E hysteresis loop exhibits well-saturated rectangular shape due to the presence of less oxygen-related defects and phase purity of the nanowires. The high value of saturation polarization was around  $54\ \mu\text{C/cm}^2$  observed

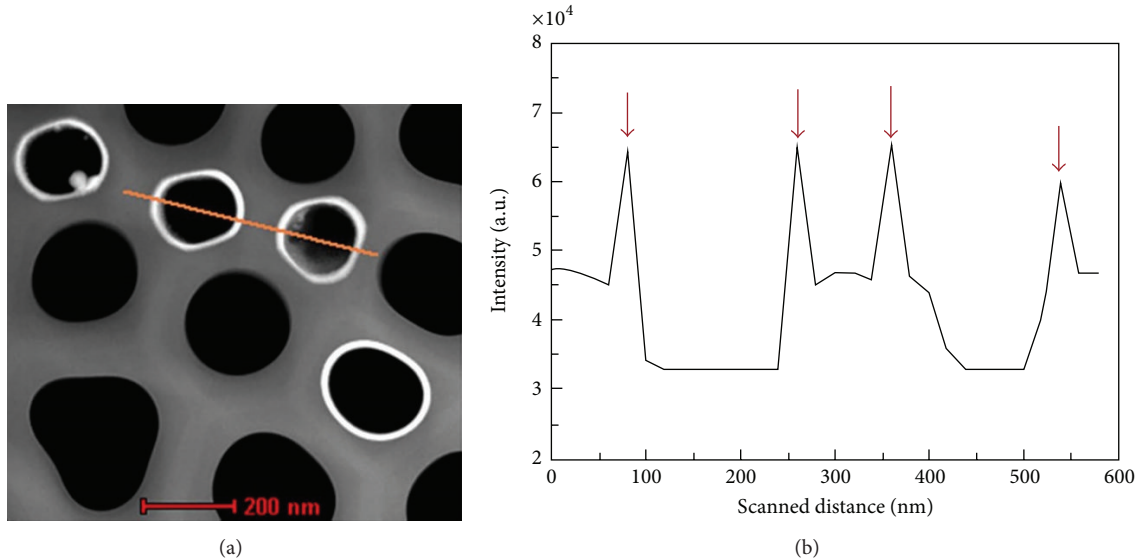


FIGURE 5: (a) STEM image of the BiFeO<sub>3</sub> nanorings, (b) line scan of the intensity distribution of the STEM image contrast of the BiFeO<sub>3</sub> nanorings (the scanned line indicated in (a)).

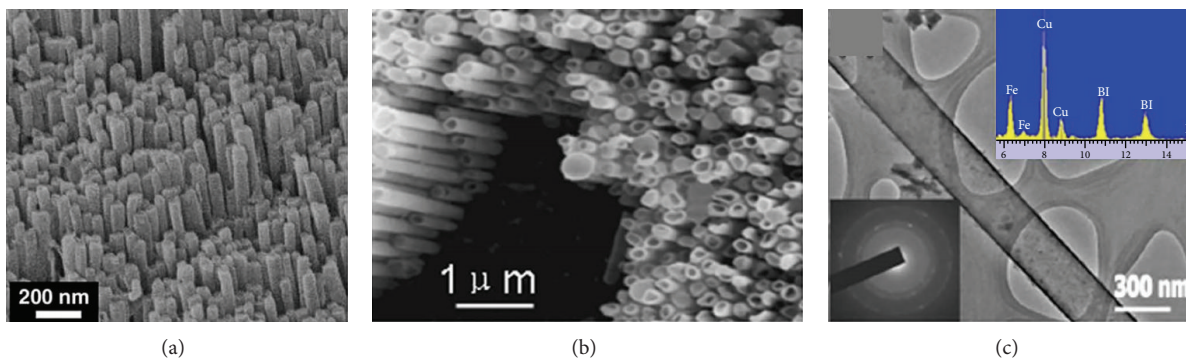


FIGURE 6: (a) SEM image of the BiFeO<sub>3</sub> nanowire array, (b) top-view of the nanochannel porous alumina filled with BiFeO<sub>3</sub> nanotubes, (c) TEM image of an isolated BiFeO<sub>3</sub> nanotube, the left inset shows the corresponding SAED pattern and the right inset shows the EDX spectrum.

at 535 kV/cm applied electric field. Figure 11(b) displays the relative dielectric constant ( $\epsilon$ ) of the BFO nanowire arrays as a function of frequency. A monotonous decrease of dielectric constant and dielectric loss was observed as Maxwell-Wagner type interfacial polarization, and in increasing the frequency, which was ascribed to good agreement with Koops phenomenological theory. The dielectric constant was measured to be as high as 492 at 1 KHz, which was due to space charge polarization resulting from the inhomogeneous dielectric structure. Recently, BFO nanotubes are also being prepared by a template synthesis involving the sol-gel technique [31]. Their ferroelectric and piezoelectric properties were characterized by PFM measurements. The piezoresponse  $d_{33}$  hysteresis loop of an individual BFO nanotube was measured using the conductive atomic force microscope tip applied with a 16.5 kHz ac electric field plus a swept dc voltage, and the result is shown in Figure 12(a). The decrease in  $d_{33}$  at high electric field, as shown in Figure 12(a), is ascribed to a consequence of the field-induced lattice hardening, which

is typical for perovskite piezoelectrics. The significant piezoelectric characteristics illustrate the ferroelectric behavior of the BFO nanotubes. The dielectric constant and dielectric loss of the BFO nanotube arrays were also measured at room temperature as a function of the frequency in the range of  $10^3$ – $10^6$  Hz, as shown in Figure 12(b). Both the dielectric constant and the dielectric loss show a remarkable decrease of up to  $10^3$  Hz and remain fairly constant afterward. The decrease in the dielectric constant with increasing the frequency represents the anomalous dispersion of the dielectric constant at low and intermediate frequencies, which has been explained by the phenomenon of dipole relaxation; while the variation in dielectric loss with frequency represents the relaxation absorption of the dielectrics.

## 5. Applications of BFO Nanostructures

BFO is one of several rare single-phase multiferroic materials that are both ferroelectric and weakly ferromagnetic at

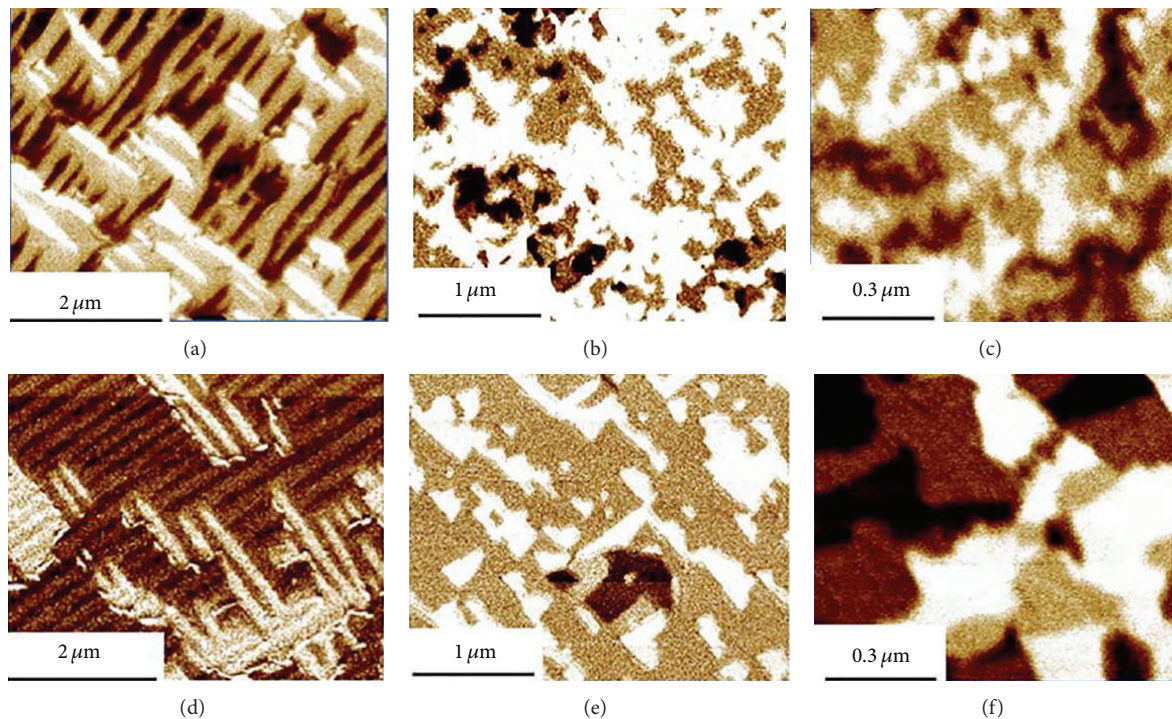


FIGURE 7: In-plane PFM images measured on (a) 120, (b) 15, and (c) 2 nm thick BFO samples on SrTiO<sub>3</sub> and in-plane PFM images measured on (d) 120, (e) 15, and (f) 2 nm thick BFO samples on DySrO<sub>3</sub> substrates.

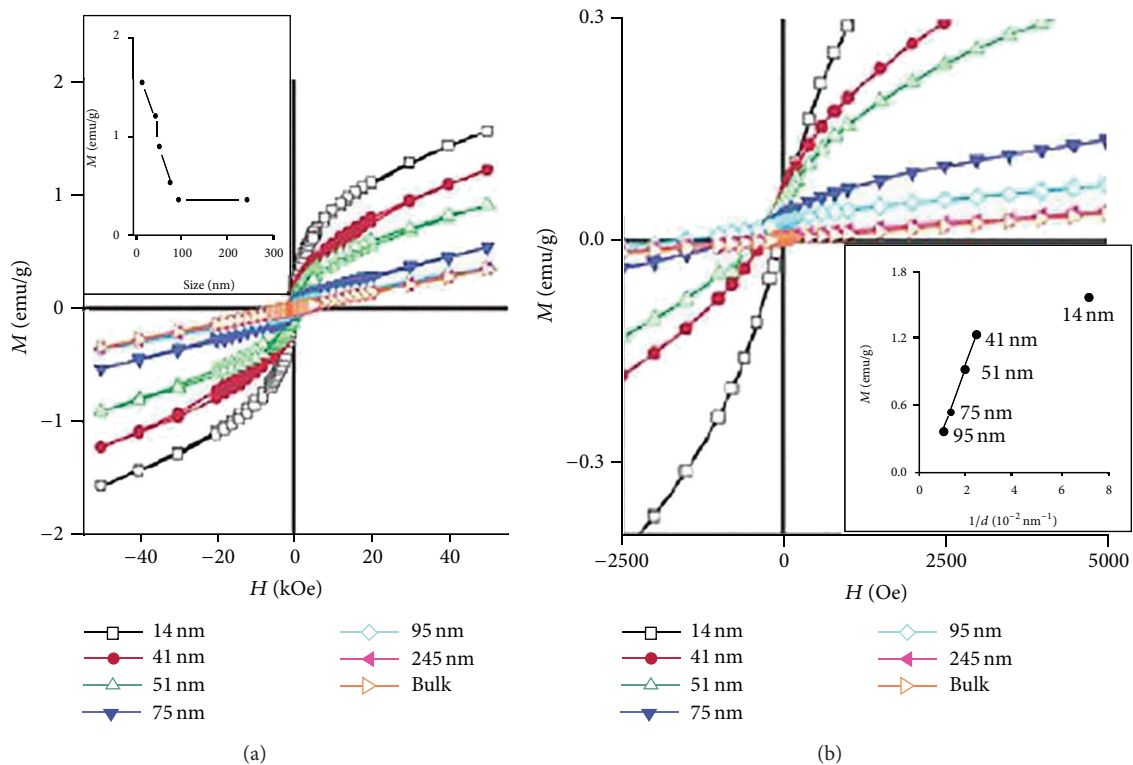


FIGURE 8: (a) Hysteresis loops measured at 300 K for BiFeO<sub>3</sub> nanoparticles with indicated sizes, (b) expanded plots of magnetization of BiFeO<sub>3</sub> nanoparticles with the return branches of the hysteresis loops omitted for clarity.

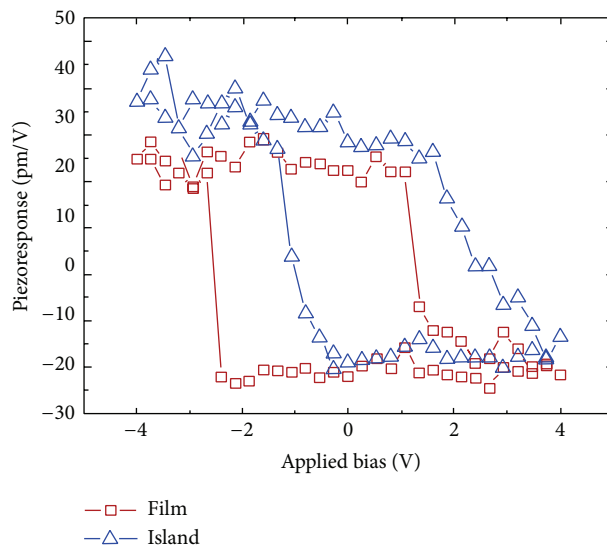


FIGURE 9: Local remanent piezoresponse hysteresis plots as resulting from measurements performed on an island (triangles) and on an area of the parent film (squares).

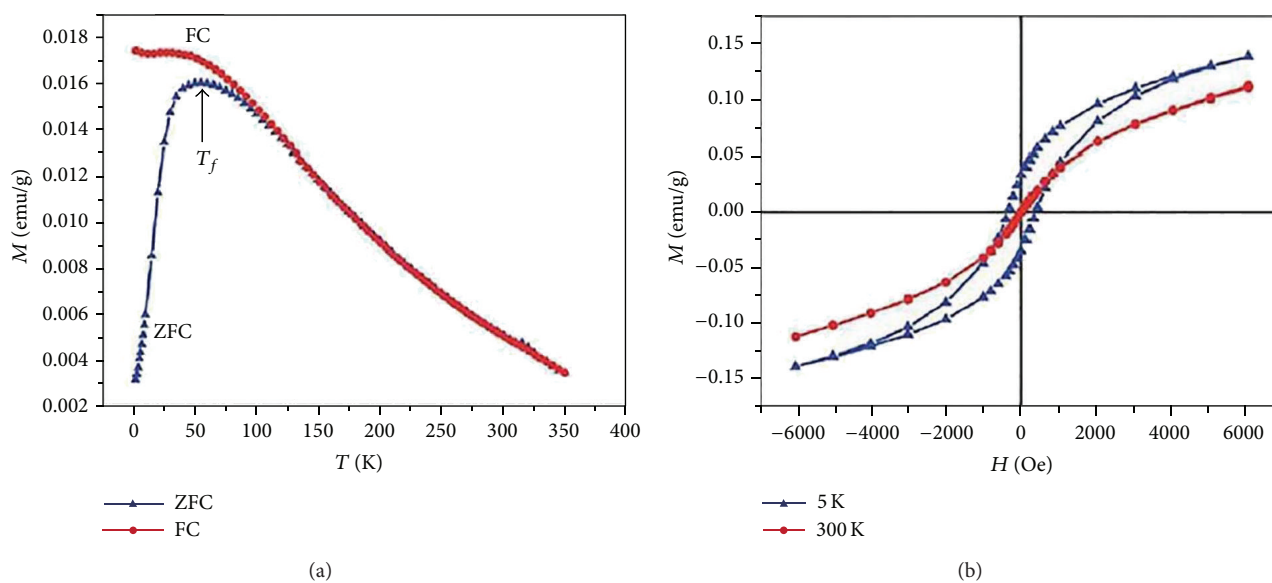


FIGURE 10: (a) Temperature dependence of zero-field-cooled (ZFC) and field-cooled (FC) susceptibility measured in a field of 100 Oe for  $\text{BiFeO}_3$  nanowires, (b)  $M$ - $H$  hysteresis loops for  $\text{BiFeO}_3$  nanowires measured at 5 K and 300 K.

room temperature. Recent studies demonstrate that the BFO nanomaterials have spontaneous polarization enhancement, switchable ferroelectric diode effects, photovoltaic effects, piezoelectric, and THz radiation properties, which have potential applications in the fields of next-generation, lead-free, nondestructive memories, spin valve devices, actuators, and ultrahigh speed telecommunication devices [37].

BFO nanoparticles also exhibit good photocatalytic activities in visible-light region, which can be used as novel visible-light-responsive photocatalysts for degradation of organic compounds. For example, Zhu et al. [28] synthesized spherical perovskite-type single-crystalline BFO nanoparticles with diameters of 10–50 nm by microwave hydrothermal process,

which exhibited efficient photocatalytic activity for the degradation of rhodamine B in aqueous solution under visible-light irradiation. Gao et al. [18] also synthesized BFO nanoparticles, which promoted the degradation rate of methyl orange to a high level under visible-light irradiation. In addition, Yu et al. [38] reported that perovskite-structured  $\text{BiFeO}_3$  nanoparticles also exhibited excellent gas-sensing properties, which were potentially useful for high-quality gas sensors.

Due to the coupling of ferroelectric and antiferromagnetic vectors, reversing the ferroelectric polarization by an external electric field also rotates the antiferromagnetic spins. Chu et al. [39] presented electric-field control of local

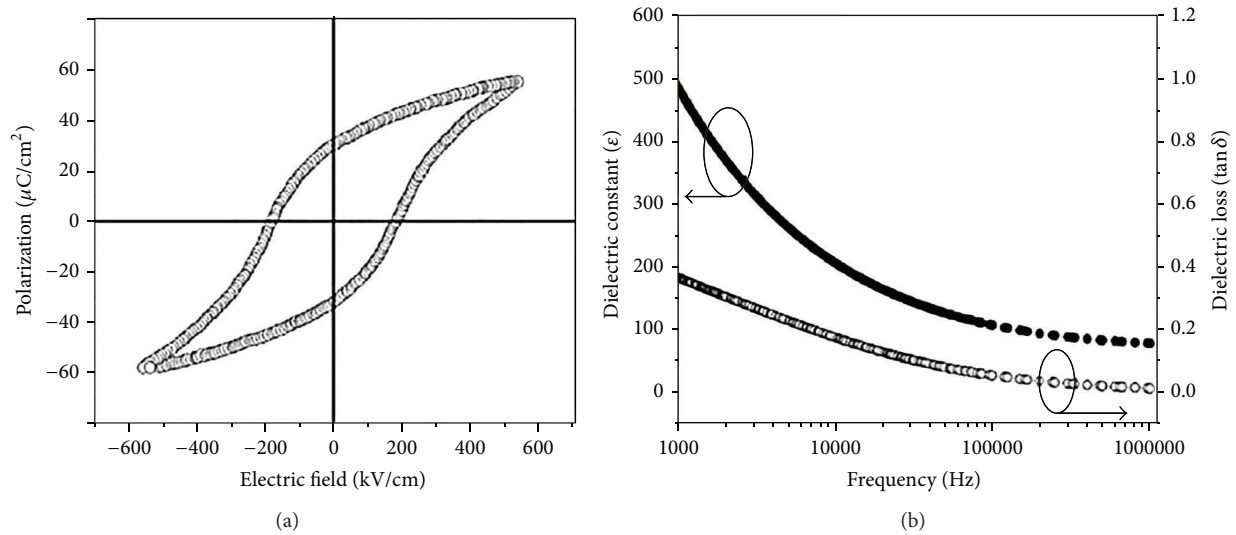


FIGURE 11: (a) Polarization versus applied electric field hysteresis loop, (b) relative dielectric constant and dielectric loss versus the frequency traits of BiFeO<sub>3</sub> nanowires.

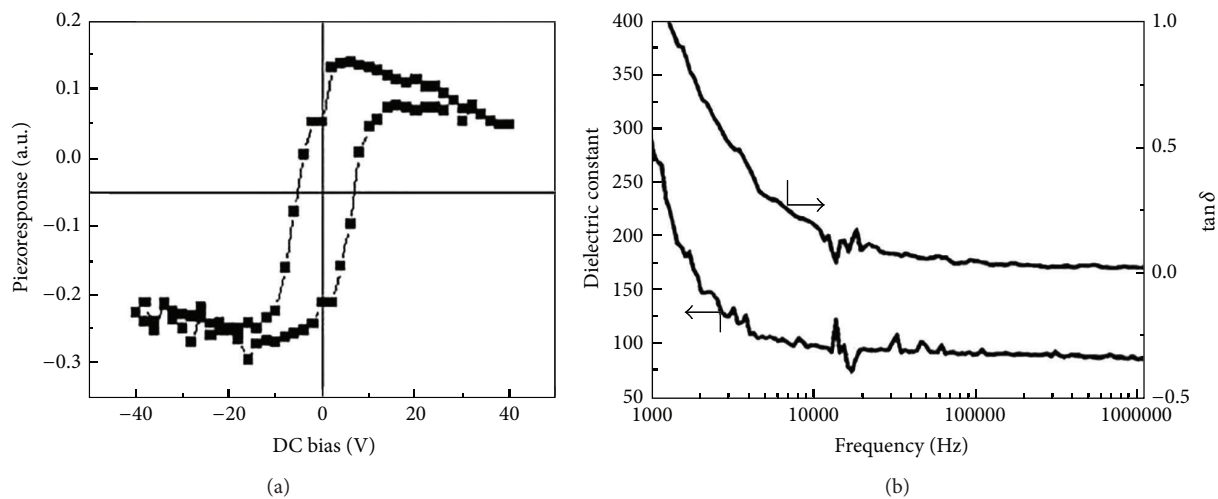


FIGURE 12: (a) Piezoelectric hysteresis loop of a single BiFeO<sub>3</sub> nanotube measured by PFM, (b) dielectric constant and dielectric loss measured at room temperature as a function of the frequency.

ferromagnetism through the coupling between the multiferroic BFO and a ferromagnet (CoFe in their work). They grew heterostructures of Au (2 nm)/CoFe (2.5–20 nm)/BFO (50–200 nm)/SrRuO<sub>3</sub> (25–50 nm) on SrTiO<sub>3</sub> (001)-oriented substrates. When applied an external in-plane electric field, they observed that the average magnetization direction in CoFe the ferromagnet rotates by 90°. The average magnetization direction changes back to the original state when applying the electric field again. If one suggests the original state as the binary signal “0,” the rotated state of the magnetization direction is represented the signal “1.” Therefore, the repeated such heterostructures can be used as essential building blocks to fabricate magnetoelectric random access memory elements.

Due to worldwide energy crisis, the investigation of materials for thin film photovoltaic cells is essential to renewable energy production. The large saturation polarization

( $\sim 90 \mu\text{C}/\text{cm}^2$ ) in BFO thin film and the band gap of BFO ( $E_g \sim 2.67 \text{ eV}$ ) smaller than many other ferroelectric perovskites make BFO the remarkable candidate for the photovoltaic cells. Yang et al. [40] reported photovoltaic devices based on BFO thin films and demonstrated the highest efficiency for the ferroelectric-based photovoltaic. They grew epitaxial ferroelectric BFO thin film by metal-organic chemical vapor deposition on (001)-oriented SrTiO<sub>3</sub> substrates with 50 nm epitaxial SrRuO<sub>3</sub> as bottom electrodes. Figure 13(a) shows a set of polarization-electric field hysteresis loops as a function of the test frequency which reveals a strong diode-like behavior, characterized by a large, directional leakage at negative voltages. Figure 13(b) shows the  $I$ - $V$  curves taken both in dark and under 285 mW/cm<sup>2</sup> white-light illumination which reveals diode-like behavior and a photovoltaic effect of the heterostructure. External quantum efficiency (EQE)

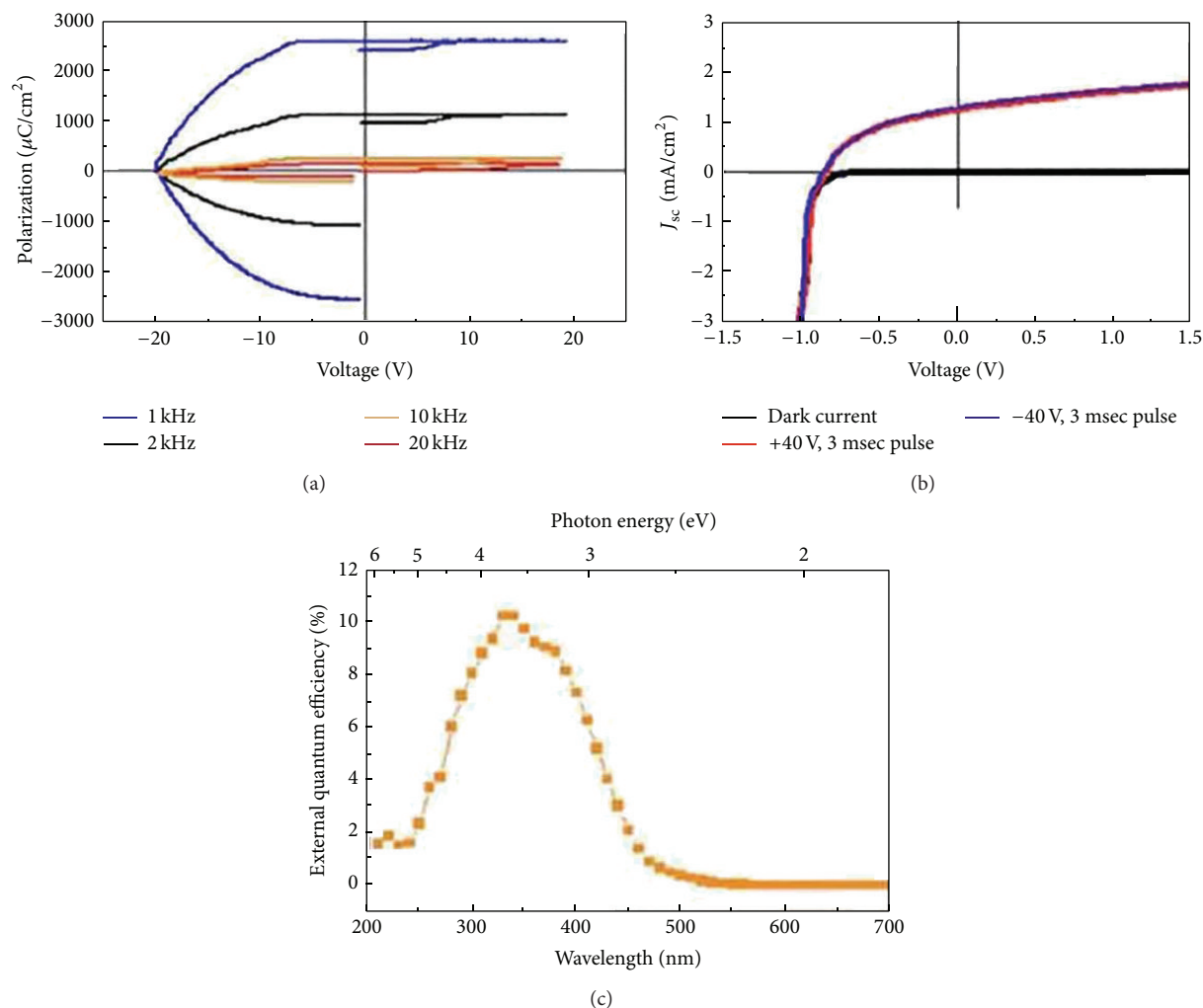


FIGURE 13: (a) Polarization-electric field hysteresis loops at various frequencies reveal diode-like behavior in one direction, (b) light (red and blue) and dark (black curve, running through the origin)  $I$ - $V$  measurements completed at 2.85 suns intensity reveal photovoltaic effects in these device structures. There is no observed change in the light  $I$ - $V$  response upon application of an electric field and (c) average EQE measurements for five different contacts on a single sample reveal efficiencies  $\sim 10\%$  under illumination with band gap light.

measurement is shown in Figure 13(c) which reveals that the maximum conversion efficiency ( $\sim 10\%$ ) is observed when the photon energy is larger than the band gap of BFO and drops off at the shortest wavelength ( $< 325$  nm).

## 6. Conclusions

This paper reviews the recent research progress of low-dimensional BFO nanostructures, including their fabrication, property, structural characterization, and applications. Perovskite-type BFO as one of the few known single-phase multiferroics that possesses ferroelectricity and antiferromagnetism at room temperature. Its low-dimensional nanostructures are much attractive in the applications of multistate storage, magnetoelectric sensor, and spintronic devices. As the feature sizes of the microelectronic enter into nanoscale, there are still some problems that need to be solved in fabrication, characterization, and application of BFO low-dimensional nanostructures. For instance, in BFO nanostruc-

tures there exist quantum size effect, (ferroelectric and magnetoelectric) size effect, and surface/interface effect; all these effects must be considered together from experimental and theoretical researches, which are fundamental to developing the new generation of revolutionary electronic nanodevices. Although the BFO has good ferroelectricity, its weak ferromagnetism is highly required to be enhanced, which could be achieved in low-dimensional nanostructures. Therefore, deeper understanding of the fundamentals of the BFO low-dimensional nanostructures with the development of advanced technology and exploring the coexistence of ferroelectricity and ferromagnetism with strong coupling between them will be the future direction of BFO nanomaterials researches.

## Conflict of Interests

The authors declare that there is no conflict of interests regarding the publication of this paper.

## Acknowledgments

This work was partially supported by National Natural Science Foundation of China (Grant nos. 11174122 and 11134004), National Basic Research Program of China (Grant nos. 2009CB929503 and 2012CB619400), and the open project from National Laboratory of Solid State Microstructures, Nanjing University.

## References

- [1] H. Schmid, "Multi-ferroic magnetoelectrics," *Ferroelectrics*, vol. 162, no. 1, pp. 317–338, 1994.
- [2] B. B. van Aken, J. R. Rivera, H. Schmid, and M. Fiebig, "Observation of ferrotoroidic domains," *Nature*, vol. 449, no. 7163, pp. 702–705, 2007.
- [3] N. A. Spaldin and M. Fiebig, "The renaissance of magnetoelectric multiferroics," *Science*, vol. 309, no. 5733, pp. 391–392, 2005.
- [4] C. Ederer and N. A. Spaldin, "Weak ferromagnetism and magnetoelectric coupling in bismuth ferrite," *Physical Review B: Condensed Matter and Materials Physics*, vol. 71, no. 6, Article ID 060401, 4 pages, 2005.
- [5] C. Ederer and N. A. Spaldin, "Influence of strain and oxygen vacancies on the magnetoelectric properties of multiferroic bismuth ferrite," *Physical Review B*, vol. 71, no. 22, Article ID 224103, 9 pages, 2005.
- [6] M. Kumar and K. L. Yadav, "Study of room temperature magnetoelectric coupling in Ti substituted bismuth ferrite system," *Journal of Applied Physics*, vol. 100, no. 7, Article ID 074111, 4 pages, 2006.
- [7] D. H. Wang, W. C. Goh, M. Ning, and C. K. Ong, "Effect of Ba doping on magnetic, ferroelectric, and magnetoelectric properties in multiferroic BiFeO<sub>3</sub> at room temperature," *Applied Physics Letters*, vol. 88, no. 21, Article ID 212907, 3 pages, 2006.
- [8] T. Zhao, A. Scholl, F. Zavaliche et al., "Electrical control of antiferromagnetic domains in multiferroic BiFeO<sub>3</sub> films at room temperature," *Nature Materials*, vol. 5, no. 10, pp. 823–829, 2006.
- [9] T. Park, G. C. Papaefthymiou, A. J. Viescas, A. R. Moodenbaugh, and S. S. Wong, "Size-dependent magnetic properties of single-crystalline multiferroic BiFeO<sub>3</sub> nanoparticles," *Nano Letters*, vol. 7, no. 3, pp. 766–772, 2007.
- [10] H. Zhang and K. Kajiyoshi, "Hydrothermal synthesis and size-dependent properties of multiferroic bismuth ferrite crystallites," *Journal of the American Ceramic Society*, vol. 93, no. 11, pp. 3842–3849, 2010.
- [11] R. R. Das, D. M. Kim, S. H. Baek et al., "Synthesis and ferroelectric properties of epitaxial BiFeO<sub>3</sub> thin films grown by sputtering," *Applied Physics Letters*, vol. 88, no. 24, Article ID 242904, 3 pages, 2006.
- [12] R. Mazumder, P. S. Devi, D. Bhattacharya, P. Choudhury, A. Sen, and M. Raja, "Ferromagnetism in nanoscale BiFeO<sub>3</sub>," *Applied Physics Letters*, vol. 91, no. 6, Article ID 062510, 3 pages, 2007.
- [13] S. M. Stratulat, X. L. Lu, A. Morelli, D. Hesse, W. Erfurth, and M. Alexe, "Nucleation-induced self-assembly of multiferroic BiFeO<sub>3</sub>-CoFe<sub>2</sub>O<sub>4</sub> nanocomposites," *Nano Letters*, vol. 13, no. 8, pp. 3884–3889, 2013.
- [14] R. Nath, S. Hong, J. A. Klug et al., "Effects of cantilever buckling on vector piezoresponse force microscopy imaging of ferroelectric domains in BiFeO<sub>3</sub> nanostructures," *Applied Physics Letters*, vol. 96, no. 16, Article ID 163101, 3 pages, 2010.
- [15] M. Park, S. Hong, J. A. Klug et al., "Three-dimensional ferroelectric domain imaging of epitaxial BiFeO<sub>3</sub> thin films using angle-resolved piezoresponse force microscopy," *Applied Physics Letters*, vol. 97, no. 11, Article ID 112907, 3 pages, 2010.
- [16] R. Nath, S. Hong, J. A. Klug et al., "Effects of cantilever buckling on vector piezoresponse force microscopy imaging of ferroelectric domains in BiFeO<sub>3</sub> nanostructures," *Applied Physics Letters*, vol. 96, Article ID 163101, 2010.
- [17] J. K. Kim, S. S. Kim, and W. J. Kim, "Sol-gel synthesis and properties of multiferroic BiFeO<sub>3</sub>," *Materials Letters*, vol. 59, no. 29–30, pp. 4006–4009, 2005.
- [18] F. Gao, X. Chen, K. Yin et al., "Visible-light photocatalytic properties of weak magnetic BiFeO<sub>3</sub> nanoparticles," *Advanced Materials*, vol. 19, no. 19, pp. 2889–2892, 2007.
- [19] X.-Z. Chen, Z.-C. Qiu, J.-P. Zhou, G. Zhu, X.-B. Bian, and P. Liu, "Large-scale growth and shape evolution of bismuth ferrite particles with a hydrothermal method," *Materials Chemistry and Physics*, vol. 126, no. 3, pp. 560–567, 2011.
- [20] S. H. Han, K. S. Kim, H. G. Kim et al., "Synthesis and characterization of multiferroic BiFeO<sub>3</sub> powders fabricated by hydrothermal method," *Ceramics International*, vol. 36, no. 4, pp. 1365–1372, 2010.
- [21] Y. Wang, G. Xu, Z. Ren et al., "Mineralizer-assisted hydrothermal synthesis and characterization of BiFeO<sub>3</sub> nanoparticles," *Journal of the American Ceramic Society*, vol. 90, no. 8, pp. 2615–2617, 2007.
- [22] B. Liu, B. Hu, and Z. Du, "Hydrothermal synthesis and magnetic properties of single-crystalline BiFeO<sub>3</sub> nanowires," *Chemical Communications*, vol. 47, no. 28, pp. 8166–8168, 2011.
- [23] L. Zhang, X. Cao, Y. Ma, X. Chen, and Z. Xue, "Polymer-directed synthesis and magnetic property of nanoparticles-assembled BiFeO<sub>3</sub> microrods," *Journal of Solid State Chemistry*, vol. 183, no. 8, pp. 1761–1766, 2010.
- [24] T. J. Park, Y. Mao, and S. S. Wong, "Synthesis and characterization of multiferroic BiFeO<sub>3</sub> nanotubes," *Chemical Communications*, no. 23, pp. 2708–2709, 2004.
- [25] X. Y. Zhang, J. Y. Dai, and C. W. Lai, "Synthesis and characterization of highly ordered BiFeO<sub>3</sub> multiferroic nanowire arrays," *Progress in Solid State Chemistry*, vol. 33, no. 2–4, pp. 147–151, 2005.
- [26] F. Gao, Y. Yuan, K. F. Wang et al., "Preparation and photoabsorption characterization BiFeO<sub>3</sub> nanowires," *Applied Physics Letters*, vol. 89, no. 10, Article ID 102506, 3 pages, 2006.
- [27] A. Morelli, F. Johann, N. Schammelt, D. McGrouther, and I. Vrejoiu, "Mask assisted fabrication of nanoislands of BiFeO<sub>3</sub> by ion beam milling," *Journal of Applied Physics*, vol. 113, no. 15, Article ID 154101, 4 pages, 2013.
- [28] X. H. Zhu, Q. M. Hang, Z. B. Xing et al., "Microwave hydrothermal synthesis, structural characterization, and visible-light photocatalytic activities of single-crystalline bismuth ferric nanocrystals," *Journal of the American Ceramic Society*, vol. 94, no. 8, pp. 2688–2693, 2011.
- [29] Q. M. Hang, X. H. Zhu, Z. J. Tang, Y. Song, and Z. G. Liu, "Self-assembled perovskite epitaxial multiferroic BiFeO<sub>3</sub> nanoislands," *Advanced Materials Research*, vol. 197–198, pp. 1325–1331, 2011.
- [30] J. Zhou, S. Liang, S. Y. Li, Z. D. Liu, Y. Y. Zhu, and X. H. Zhu, "Advances in low-dimensional BiFeO<sub>3</sub> multiferroic nanostructures," *Journal of Chinese Electron Microscopy Society*, vol. 32, no. 6, pp. 504–524, 2013.

- [31] X. Y. Zhang, C. W. Lai, X. Zhao, D. Y. Wang, and J. Y. Dai, "Synthesis and ferroelectric properties of multiferroic BiFeO<sub>3</sub> nanotube arrays," *Applied Physics Letters*, vol. 87, no. 14, Article ID 143102, 3 pages, 2005.
- [32] Y. H. Chu, T. Zhao, M. P. Cruz et al., "Ferroelectric size effects in multiferroic BiFeO<sub>3</sub> thin films," *Applied Physics Letters*, vol. 90, no. 25, Article ID 252906, 3 pages, 2007.
- [33] I. Naumov and A. M. Bratkovsky, "Unusual polarization patterns in flat epitaxial ferroelectric nanoparticles," *Physical Review Letters*, vol. 101, no. 10, Article ID 107601, 4 pages, 2008.
- [34] S. K. Streiffer and D. D. Fong, "Phase transitions in nanoscale ferroelectric structures," *MRS Bulletin*, vol. 34, no. 11, pp. 832–837, 2009.
- [35] S. Li, R. Nechache, C. Harnagea, L. Nikolova, and F. Rosei, "Single-crystalline BiFeO<sub>3</sub> nanowires and their ferroelectric behavior," *Applied Physics Letters*, vol. 101, no. 19, Article ID 192903, 3 pages, 2012.
- [36] G. S. Lotey and N. K. Verma, "Magnetoelectric coupling in multiferroic BiFeO<sub>3</sub> nanowires," *Chemical Physics Letters*, vol. 579, no. 30, pp. 78–84, 2013.
- [37] M. Bibes and A. Barthélémy, "Multiferroics: towards a magnetoelectric memory," *Nature Materials*, vol. 7, no. 6, pp. 425–426, 2008.
- [38] X. L. Yu, Y. Wang, Y. M. Hu, C. Cao, and H. L. Chan, "Gas-sensing properties of perovskite BiFeO<sub>3</sub> nanoparticles," *Journal of the American Ceramic Society*, vol. 92, no. 12, pp. 3105–3107, 2009.
- [39] Y. H. Chu, L. W. Martin, M. B. Holcomb et al., "Electric-field control of local ferromagnetism using a magnetoelectric multiferroic," *Nature Materials*, vol. 7, no. 6, pp. 478–482, 2008.
- [40] S. Y. Yang, L. W. Martin, S. J. Byrnes et al., "Photovoltaic effects in BiFeO<sub>3</sub>," *Applied Physics Letters*, vol. 95, no. 6, Article ID 062909, 3 pages, 2009.

## Research Article

# Enhanced Magnetization of Sol-Gel Synthesized Pb-Doped Strontium Hexaferrites Nanocrystallites at Low Temperature

Shahid M. Ramay,<sup>1</sup> Shahid Atiq,<sup>2</sup> Murtaza Saleem,<sup>3</sup>  
Asif Mahmood,<sup>4</sup> Saadat A. Siddiqi,<sup>5</sup> Shahzad Naseem,<sup>2</sup> Yousef Al-Zeghayer,<sup>4,6</sup>  
Nasser S. Alzayed,<sup>1</sup> and Mohammed Shahabuddin<sup>1</sup>

<sup>1</sup> Department of Physics and Astronomy, College of Science, King Saud University, P.O. Box 800, Riyadh 11421, Saudi Arabia

<sup>2</sup> Centre of Excellence in Solid State Physics, University of the Punjab, Lahore 54590, Pakistan

<sup>3</sup> Department of Physics, School of Science and Engineering (SSE), Lahore University of Management Sciences (LUMS), Lahore 54792, Pakistan

<sup>4</sup> Department of Chemical Engineering, College of Engineering, King Saud University, P.O. Box 800, Riyadh 11421, Saudi Arabia

<sup>5</sup> Interdisciplinary Research Centre in Biomedical Materials (IRCBM), COMSATS Institute of Information Technology, Defence Road, Off Raiwind Road, Lahore 54600, Pakistan

<sup>6</sup> Industrial Catalysts Research Chair, King Saud University, Riyadh 11421, Saudi Arabia

Correspondence should be addressed to Shahid Atiq; [satiq.cssp@pu.edu.pk](mailto:satiq.cssp@pu.edu.pk)

Received 24 January 2014; Revised 1 May 2014; Accepted 3 May 2014; Published 27 May 2014

Academic Editor: Debasis Dhak

Copyright © 2014 Shahid M. Ramay et al. This is an open access article distributed under the Creative Commons Attribution License, which permits unrestricted use, distribution, and reproduction in any medium, provided the original work is properly cited.

Effect of Pb doping on the structural and low temperature magnetic properties of  $\text{SrPb}_x\text{Fe}_{12-x}\text{O}_{19}$  ( $x = 0, 0.1, 0.2, 0.3,$  and  $0.4$ ), synthesized by sol-gel autocombustion technique, has been investigated. The powder samples were sintered at  $800^\circ\text{C}$  for 2 h in order to develop the stable hexagonal phase, characteristic of the  $\text{SrFe}_{12}\text{O}_{19}$  structure. The consequences of Pb substitution (at iron sites) on various structural parameters like lattice constants, unit cell volume, crystallite size, and porosity have been discussed. Fourier transform infrared frequency bands were utilized to determine the formation of tetrahedral and octahedral clusters of M-type ferrites. Hexagonal texture of the grains, a characteristic of the hexagonal crystal structure of  $\text{SrFe}_{12}\text{O}_{19}$ , was refined by Pb substitution. The magnetic properties, determined using a vibrating sample magnetometer, revealed that saturation magnetization decreased, while coercivity was increased with the increase of Pb contents. However, the increased squareness ratio and hence the energy product motivate the utilization of these ferrite compositions where hard magnetic characteristics are required. The increased values of saturation magnetization were observed at reduced temperature of 200 K, attributable to the better spin alignments of individual magnetic moments at low temperature.

## 1. Introduction

M-type hexagonal ferrites belong to immensely valuable class of magnetic materials, with a host of applications ranging from simple permanent magnets used in electric motors to modern day applications, for instance, as radar wave absorbing materials. Owing to its high values of saturation magnetization and coercivity [1], strontium hexaferrite, in particular, is a very important member of this class of magnetic materials, being widely used in telecommunication [2], magneto-optic recording media, microwave devices [3], and electronic industry [4]. Various preparation techniques

like coprecipitation process, molten salt method, solid state reaction method [5], double sintering ceramic technique [6], microwave-induced combustion process, sol-gel based synthesis routes [7], and so forth have been adopted by the researchers to refine the astonishing structural and magnetic properties of these ferrites. However, sol-gel based autocombustion route, being easier, energy efficient, and cheaper, has emerged as a novel technique to prepare single phase strontium hexaferrites. The crystal structure of  $\text{SrFe}_{12}\text{O}_{19}$  is hexagonal which has a great influence on valuable characteristics of these ferrites. One-unit cell of these ferrites is composed of 64 ions that are distributed in such a way that

these form two formula units, each having one spinel S-block and one hexagonal R-block [2]. The  $\text{Fe}^{3+}$  ions are oriented on five different crystallographic sites in the unit cell. These ions are the major cause of magnetism in these ferrites, resulting in net magnetic moment of  $20 \mu_B$  per formula unit [8, 9].

Ferrimagnetic strontium hexaferrites are n-type semiconductor with band gap energy of 0.6 eV. Researchers are attempting to improve the intrinsic properties of these ferrites for innovations. For this purpose, introduction of some divalent or trivalent dopant element and optimization of preparation technique play a vital role. Diamagnetic Pb ions, substituted at Fe sites with spin up, could enhance the hard magnetic characteristics of  $\text{SrFe}_{12}\text{O}_{19}$  when doped stoichiometrically. Hence, it has been understood as a quite suitable dopant choice for these ferrites to improve not only the structural properties but also the magnetic properties [2, 3, 8]. In the present work, we have successfully employed sol-gel based autocombustion technique to prepare the ferrite samples in phase-pure form to investigate the structural and low temperature magnetic properties of Pb-doped strontium hexaferrites for use in devices that work efficiently with high values of coercivity and electrical devices that show minimum energy losses at higher applied frequencies.

## 2. Experimental

Single phase polycrystalline samples with compositions  $\text{SrPb}_x\text{Fe}_{12-x}\text{O}_{19}$  ( $x = 0.0, 0.1, 0.2, 0.3, \text{ and } 0.4$ ) were prepared by a novel sol-gel based autocombustion route. A transparent homogenous solution was obtained by dissolving stoichiometric proportions of analytical grade strontium nitrate (Sigma Aldrich), iron (III) nitrate (Sigma Aldrich), lead (II) nitrate (Sigma Aldrich), and citric acid (Avonchem, UK) in 50 mL of deionized water. The relative molar concentrations of citric acid, used as a fuel, and metal nitrates were in the ratio of 2:1. The solution was placed over a hot plate, positioned in a fume hood. The temperature of the hot plate was gradually increased to  $90^\circ\text{C}$ . The solution was continuously stirred using a magnetic stirrer at 500 rpm, for about 1 h, until it converted into a soft gel. At that instance, the rotator was stopped and the stirrer was removed from the gel. The temperature of the gel was increased in steps up to  $300^\circ\text{C}$ . As the gel was heated at this temperature for about 15 min., it burnt suddenly and vigorously and converted into soft and fluffy powder. The product was grinded to get homogeneously mixed powder samples. All the samples were synthesized using the same procedure and sintered at  $800^\circ\text{C}$  for 2 h in order to get hexagonal ferrite phases. X-ray diffraction (XRD) was used to investigate the crystal structure of the prepared samples. The thermogravimetric/differential (TG/DTA) analysis was performed using EXSTAR SII TG/DTA 7300 analyzer in order to investigate any weight loss of the samples at high temperatures. The powder samples were then pelletized and surface morphology was analyzed using a JSM-6610 Oxford (with EDX attachment) scanning electron microscope (SEM). Energy dispersive X-ray spectroscopy (EDX) was performed to get quantitative analysis of the samples. The formation of chemical bonds in

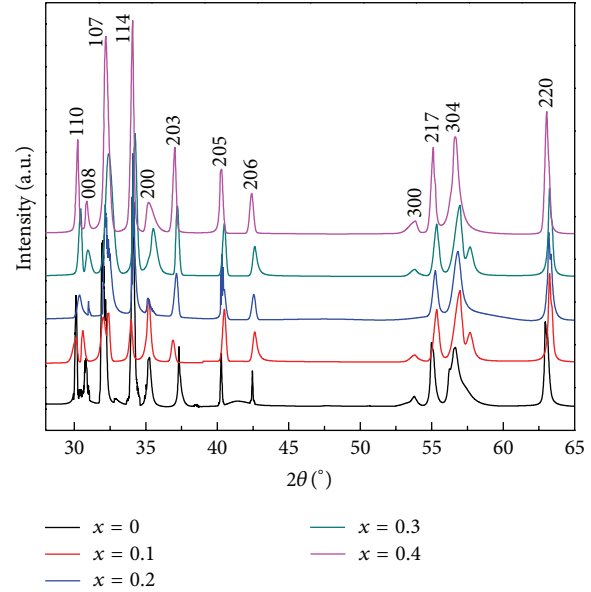


FIGURE 1: X-ray diffraction patterns of  $\text{SrPb}_x\text{Fe}_{12-x}\text{O}_{19}$  ( $x = 0.0, 0.1, 0.2, 0.3, \text{ and } 0.4$ ) sample.

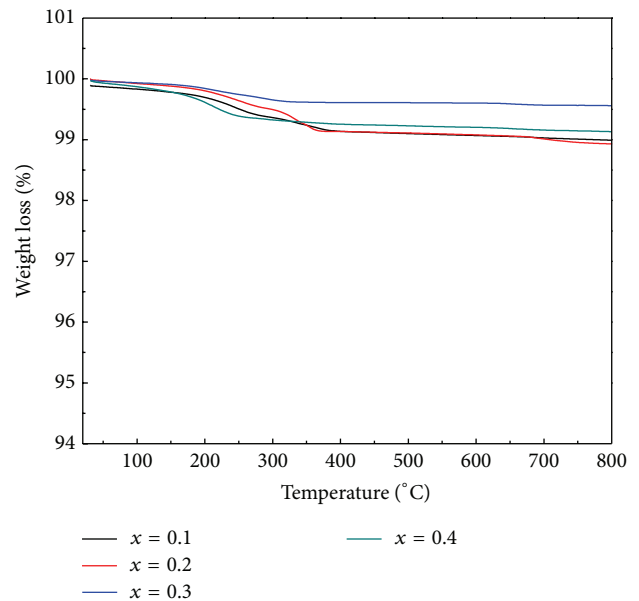


FIGURE 2: TGA spectra of  $\text{SrPb}_x\text{Fe}_{12-x}\text{O}_{19}$  ( $x = 0.1, 0.2, 0.3, \text{ and } 0.4$ ) samples.

the desired crystal phase was confirmed by Fourier transform infrared spectroscopy (FTIR). Magnetic behavior of the samples was analyzed using a 14 Tesla Quantum design PPMS (Physical Properties Measurement System).

## 3. Results and Discussion

Crystal structure of all the prepared samples was determined by X-ray diffraction, following the complete procedure as

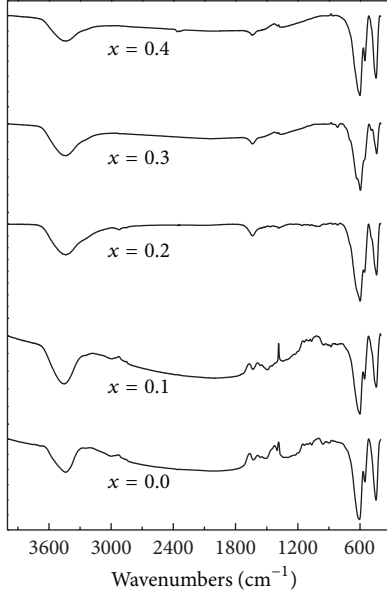


FIGURE 3: FTIR spectra of  $\text{SrPb}_x\text{Fe}_{12-x}\text{O}_{19}$  ( $x = 0.0, 0.1, 0.2, 0.3,$  and  $0.4$ ) samples.

described by Cullity [10]. Data obtained from the diffractometer was plotted. Positions of the diffracted intensities were noted and corresponding values of  $\sin^2\theta$  were evaluated. These values were multiplied by  $1/3, 1/4,$  and  $1/7$  in order to find a repeated number named “A” related to the lattice parameter “a” and wavelength ( $\lambda$ ) of the incident radiation by the relation  $A = \lambda^2/3a^2$ . Using this relation, value of “a” was evaluated for 200 plane. The relation  $\sin^2\theta - A(h^2 + hk + k^2) = Cl^2$  was used to find a parameter, “C” and hence the lattice constant, “c,” using the expression  $C = \lambda^2/4c^2$ .  $hkl$  values corresponding to all the diffracted intensities were determined and the patterns were indexed as shown in Figure 1. The indexing of the patterns revealed that crystal structures of all the samples exhibit characteristic hexagonal structure. In addition, the indexed peaks were also matched with the standard data (ICSD-00-033-1340), which confirmed that samples revealing hexagonal structure consisted of M-type strontium hexaferrites. TGA was performed up to  $800^\circ\text{C}$  with a heating rate of  $20^\circ\text{C}/\text{min}$ . to determine any carbon related species that may be present in the samples due to reaction of  $\text{Sr}^{2+}$  with  $\text{CO}_2$  which may be available from the atmosphere and/or from the decomposition of citric acid. Figure 2 shows the %age weight loss for the four samples from room temperature to  $800^\circ\text{C}$ . The curves reveal a good stability and do not indicate any significant weight loss. Hence, it is inferred that no carbon related species are present in the prepared samples and sintering of samples at  $800^\circ\text{C}$  is sufficient to hinder the formation of  $\text{SrCO}_3$  enabling the  $\text{Sr}^{2+}$  available to stimulate the incorporation of  $\text{Sr}^{2+}$  into strontium hexaferrite matrix [11]. Slight increase in the lattice parameters “a” and “c” was observed that led to a minute increase in the unit cell volume ( $V = 0.866a^2c$ ) as well. The trend might be attributed to the larger ionic

TABLE 1: Values of lattice constants, their axial ratio, unit cell volume ( $V$ ), crystallite size ( $D$ ), bulk density ( $\rho_b$ ), X-ray density ( $\rho_x$ ), porosity ( $P$ ), saturation magnetization ( $M_s$ ), remanence ( $M_r$ ),  $M_r/M_s$ , and coercivity ( $H_c$ ) at  $\text{SrPb}_x\text{Fe}_{12-x}\text{O}_{19}$  ( $x = 0.0, 0.1, 0.2, 0.3,$  and  $0.4$ ).

Parameter	$x = 0.0$	$x = 0.1$	$x = 0.2$	$x = 0.3$	$x = 0.4$
$a$ ( $\text{\AA}$ )	5.8808	5.8856	5.8880	5.8889	5.8911
$c$ ( $\text{\AA}$ )	23.2018	23.2193	23.2297	23.2360	23.2361
$c/a$	3.9453	3.9451	3.9446	3.9457	3.9443
$V$ ( $\text{nm}^3$ )	694.8841	696.5439	697.3042	697.8268	698.3515
$D$ (nm)	27.8971	28.4145	28.8917	29.9115	29.9176
$\rho_b$ ( $\text{g}/\text{cm}^3$ )	2.9124	2.9965	3.1623	3.2817	3.2862
$\rho_x$ ( $\text{g}/\text{cm}^3$ )	4.8167	4.8266	4.8615	4.9075	4.9080
$P$ (%)	39.53	37.92	34.95	33.13	33.04
$M_s$ (emu/g) at 300 K	63.22	57.79	53.16	49.65	41.62
$M_s$ (emu/g) at 200 K	70.77	63.50	60.50	53.93	48.44
$M_r$ (emu/g) at 300 K	33.05	30.62	28.71	25.84	23.66
$M_r$ (emu/g) at 200 K	38.20	34.81	33.65	30.96	28.84
$M_r/M_s$ at 300 K	0.52	0.53	0.54	0.55	0.57
$M_r/M_s$ at 200 K	0.54	0.55	0.56	0.58	0.60
$H_c$ (Oe) at 300 K	2360	3249	4360	5837	6015
$H_c$ (Oe) at 200 K	3104	3471	4322	4915	5282

radius of the substituent,  $\text{Pb}^{2+}$  ( $0.98 \text{\AA}$ ) as compared to the host,  $\text{Fe}^{3+}$  ( $0.49 \text{\AA}$ ). The crystallite sizes of all the samples evaluated using Scherrer’s relation ( $D = k\lambda/\beta\cos\theta$ ,  $k$  is a constant,  $\beta$  is full width at half maximum in radians, and  $\theta$  is diffraction angle in degrees) were increased slightly as the Pb concentration was increased in the series. The bulk density ( $\rho_b$ ) was calculated from the weight and dimensions of the sintered pellets using the relation  $\rho_b = m/\pi r^2 h$ , where  $m$  is the mass,  $r$  is the radius, and  $h$  is the thickness of the samples. X-ray density ( $\rho_x$ ) of the samples was calculated using the relation  $\rho_x = 2M/N_a a^3$  [12], where  $M$  is the molecular weight of the composition,  $N_a$  is Avogadro’s number, and  $a$  is the lattice constant. The bulk and X-ray densities were used to calculate the porosity ( $P = 1 - \rho_b/\rho_x$ ). The values of all these structural parameters have been shown in Table 1. The results reveal that porosity of the samples was decreased as the Pb contents were substituted at the Fe sites in the series of the samples. In other words, the grains became more compact and densified with the Pb substitution which could play a significant role in establishing the structural and magnetic properties.

Figure 3 shows the FTIR spectra of all the prepared samples. In ferrites, the spectroscopically active region lies between  $400 \text{ cm}^{-1}$  and  $800 \text{ cm}^{-1}$  [13]. In our samples, there were sharp and clear peaks at  $600 \text{ cm}^{-1}$ ,  $550 \text{ cm}^{-1}$ , and  $440 \text{ cm}^{-1}$ , corresponding to the characteristics peaks of chemical bonds in  $\text{SrFe}_{12}\text{O}_{19}$  structure [14]. The peak intensity remained almost the same as the amount that Pb dopant

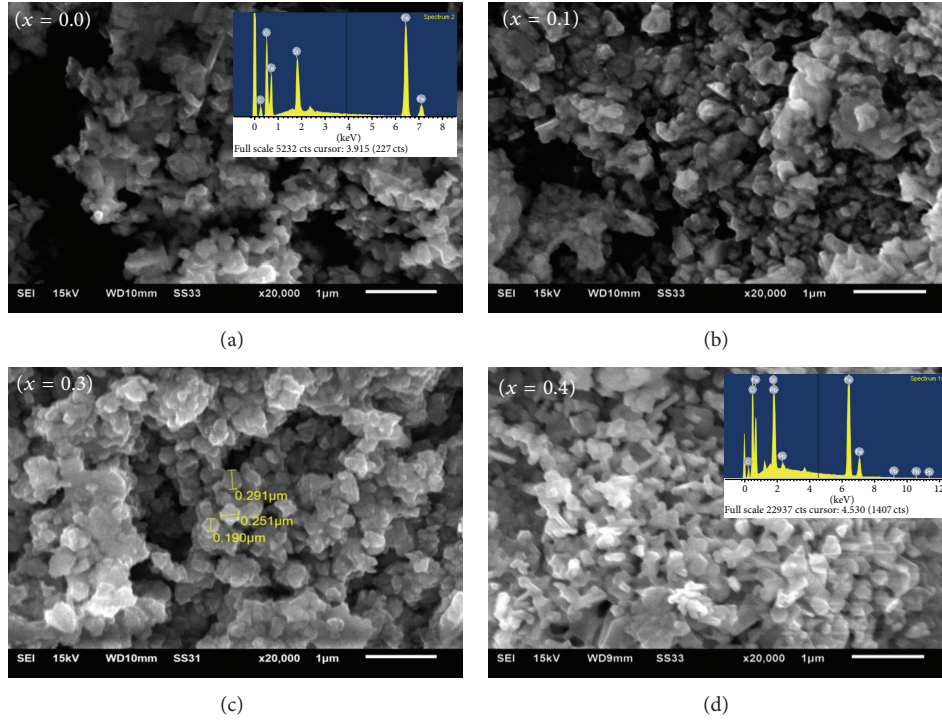


FIGURE 4: SEM micrographs of  $\text{SrPb}_x\text{Fe}_{12-x}\text{O}_{19}$  ( $x = 0.0, 0.1, 0.3,$  and  $0.4$ ) samples.

was increased by in the series, which indicated that Pb could be successfully substituted in a dilute amount at the Fe sites, without disturbing the stoichiometry of the parent hexagonal  $\text{SrFe}_{12}\text{O}_{19}$  structure. With the increase in Pb contents, the chemical polarization of the internal bonds could be shared in the form of Fe-O-Pb and Sr-O-Pb chemical bonds, resulting in compact structures as that of  $\text{SrFe}_{12}\text{O}_{19}$ . The peaks at  $3421\text{ cm}^{-1}$  and  $1639\text{ cm}^{-1}$  exhibit the structure and bending bonds of the surface hydrogen group ( $-\text{OH}$ ) earned from the damped environment [15].

Figure 4 shows the microstructural morphology of the samples obtained using a scanning electron microscope. Figure 4(a) reveals the micrograph of pure  $\text{SrFe}_{12}\text{O}_{19}$  sample indicating that most of the grains are like platelets having sharp grain boundaries. A close look at this image might provide hindsight of the hexagonal texture of the grains, a characteristic of the hexagonal crystal structure of the  $\text{SrFe}_{12}\text{O}_{19}$ . With the substitution of Pb contents at Fe sites, the microstructural morphology of the grains was further refined until at  $x = 0.3$  Pb contents; well defined hexagonal grains were witnessed which were varying in size ranging from  $0.190$  to  $0.291\ \mu\text{m}$ . The uniform grain sizes and homogeneous contrast throughout the focused area confirm that the sample consists of single phase ferrite composition. The shape and compatibility of grains play a vital role in determining the structural and magnetic properties of ferrites [16]. The platelet-like hexagonal texture of ferrites has been investigated as a potential candidate for use in microwave absorbing coatings [17]. The elemental composition of the constituents elicited from EDX, shown in the inset of Figures 4(a) and 4(d), confirms the stoichiometric ratio of the elements in the

prepared samples and the incorporation of Pb at Fe sites. The quantitative data of atomic and percentage composition of elements was in close agreement with the dissolved reactants.

Figure 5 shows the magnetic-hysteresis (M-H) loops of the prepared samples obtained at 300 K. Magnetic parameters like saturation magnetization ( $M_s$ ), remanence ( $M_r$ ), and coercivity ( $H_c$ ) were determined from M-H loops as listed in Table 1. The  $M_s$  and  $H_c$  values as a function of Pb contents have been plotted in Figure 6. The plots reveal that the substitution of Pb contents at A-site of Fe changes the magnetic properties of the ferrite samples in a remarkable way. The  $M_s$  and  $M_r$  values of the ferrite samples were decreased from  $63.22$  to  $41.62\text{ emu/g}$  and  $33.03$  to  $23.66\text{ emu/g}$ , respectively, whereas the  $H_c$  value was increased from  $2360$  to  $6015\text{ Oe}$  with the increase in the Pb contents. However, the  $M_r/M_s$  ratio was observed to increase from  $0.52$  to  $0.57$  in the series, as the decrease in  $M_r$  value is less prominent as the corresponding decrease in the  $M_s$  value, making the later samples in the series more effective, as far as energy product is concerned. The value of  $M_s$  at  $x = 0$  is in close agreement with a recently reported value [18]. The crystal structure has been understood as a critical factor which decides the magnetic behavior of the material. The crystal structure of  $\text{SrFe}_{12}\text{O}_{19}$  has five nonequivalent sublattices with three octahedral (2a, 12k, and 4f), one tetrahedral (4f1), and one trigonal bipyramidal (2b) sites [19]. Among these, three sites (2a, 12k, and 2b) possess upward spin and two sites (4f1 and 4f2) spin downward. Hence, net magnetic moment results due to upward spins. When Pb with a diamagnetic nature is substituted with some of the iron ions, a decrease in the net saturation magnetization is observed which decreases

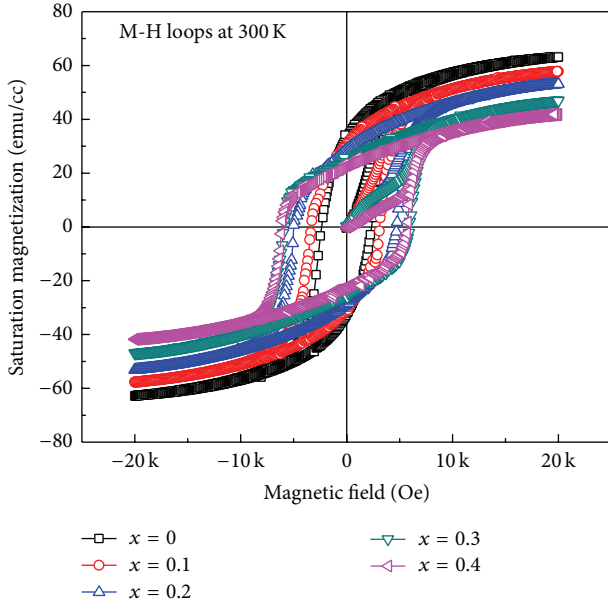


FIGURE 5: M-H loops of  $\text{SrPb}_x\text{Fe}_{12-x}\text{O}_{19}$  ( $x = 0.0, 0.1, 0.2, 0.3,$  and  $0.4$ ) samples at 300 K.

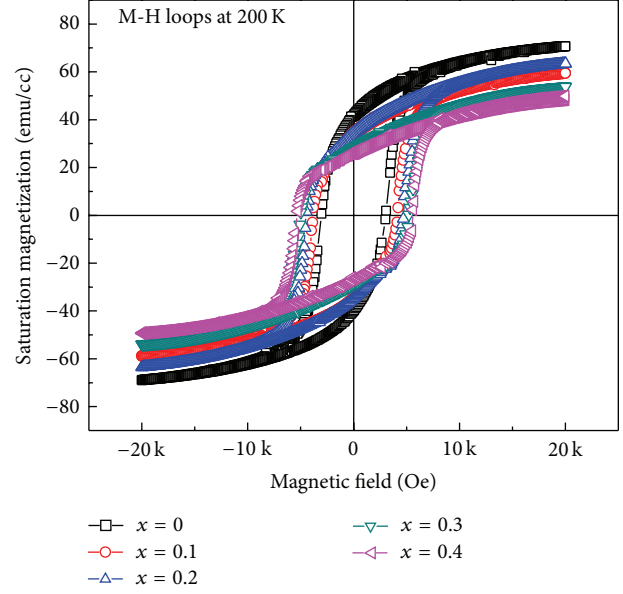


FIGURE 7: M-H loops of  $\text{SrPb}_x\text{Fe}_{12-x}\text{O}_{19}$  ( $x = 0.0, 0.1, 0.2, 0.3,$  and  $0.4$ ) samples at 200 K.

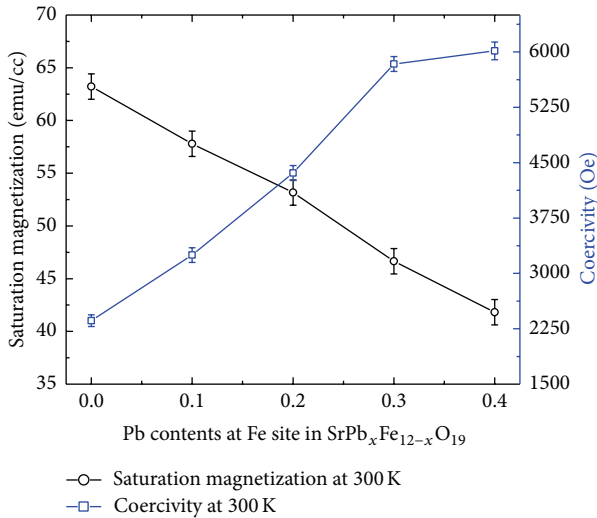


FIGURE 6:  $M_s$  and  $H_c$  as a function of Pb contents at Fe sites in  $\text{SrPb}_x\text{Fe}_{12-x}\text{O}_{19}$  at 300 K.

further as the Pb contents are increased up to  $x = 0.4$ . This decrease in  $M_s$  value could be attributed to the decrease of superexchange interactions among  $\text{Fe}_A^{3+}\text{-O-Fe}_B^{3+}$ , as the substituted ions prefer to occupy the octahedral 12k site which has upward spin [20], followed by 2a and 4f2 sites [19]. Each  $\text{Fe}^{3+}$  ion possesses a magnetic moment of  $5 \mu_B$ . Therefore, an M-type molecule of  $\text{SrFe}_{12}\text{O}_{19}$  possesses a magnetic moment of  $20.6 \mu_B$ . The substitution of a diamagnetic ion at a site with spin up reduces the total magnetic moment of the specimen and hence the  $M_s$  values decrease.

The increase in  $H_c$  with the increase in Pb contents may be described on the basis of Stoner-Wohlfarth relation,  $H_c$

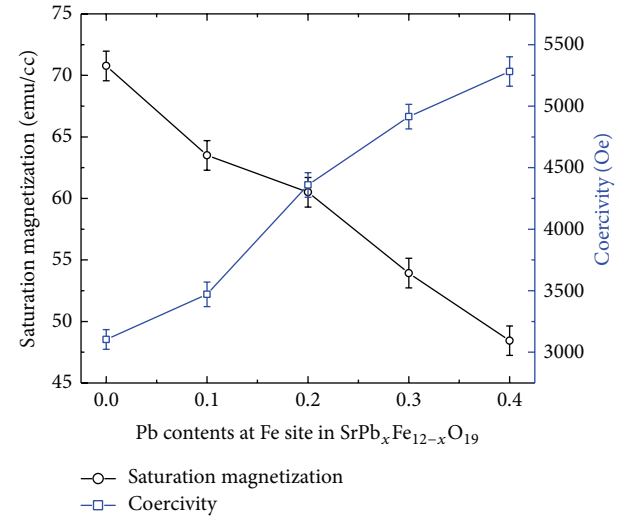


FIGURE 8:  $M_s$  and  $H_c$  as a function of Pb contents at Fe sites in  $\text{SrPb}_x\text{Fe}_{12-x}\text{O}_{19}$  at 200 K.

$= 2K/\mu_0 M_s$ , where  $K$  is magnetocrystalline anisotropy and  $\mu_0$  is permeability of free space ( $= 4\pi \times 10^{-7}$  H/m). Hence, a decrease in  $M_s$  and an increase in  $K$  [21] are the possible factors for an increased value of  $H_c$ .

Figure 7 shows the M-H loops of the samples at 200 K. The  $M_s$  and  $M_r$  values of all the samples increased as compared to their corresponding values at 300 K in the series, with the decrease in temperature, as has been plotted in Figure 8 and listed in Table 1, but decreased with the increase of Pb contents in the series. The increase in  $H_c$  as a function of Pb contents at 200 K (Figure 7) could also be explained as discussed earlier. The increased values of  $M_s$  at 200 K might be described on the basis of Weiss theory of ferromagnetism

[22]. According to this theory, at low temperatures, the thermal activation energy of the magnetic ions reduces which in turn helps the magnetic moments to align more easily in the applied field direction. Therefore, an overall increase in the magnetic moment and hence in the  $M_s$  is observed. The increased squareness ratio ( $M_r/M_s$ ) in this case as well favors the use of these materials for the applications where high energy products are desired.

#### 4. Conclusion

In this paper, the influence of Pb doping on the structural and low temperature magnetic behavior of  $\text{SrPb}_x\text{Fe}_{12-x}\text{O}_{19}$  ( $x = 0, 0.1, 0.2, 0.3,$  and  $0.4$ ) has been investigated systematically. X-ray diffraction analysis of all the samples revealed the hexagonal phase characteristics of the  $\text{SrFe}_{12}\text{O}_{19}$  crystal structure. A slight increase in the lattice constants ( $a$  and  $c$ ) and the unit cell volume was attributed to the larger ionic radii of dopant Pb as compared to the host Fe site. The crystallite size was also increased in the series as the Pb contents were increased. The porosity was decreased from 39.53 to 33.04% in the series making the samples more compact to improve the structural and hence the magnetic properties. FTIR spectroscopy confirmed the metal-oxygen bonds formation in the hexagonal structure of the samples. Surface morphology has been described using SEM images and elemental stoichiometric composition has been found using EDX spectroscopy. Saturation magnetization was found to decrease, while coercivity was increased with the increase of Pb contents in the series at 300 K. When temperature was reduced to 200 K, the saturation magnetization of the relevant samples was increased, credited to the preferred individual spin alignments at low temperature. Remanence was also decreased, but the corresponding effect was less prominent as the  $M_r/M_s$  and consequently the energy product was found to increase, corroborating the use of these ferrite compositions where hard magnetic characteristics are required.

#### Conflict of Interests

The authors declare that they have no conflict of interests regarding the publication of this paper.

#### Acknowledgment

The authors extend their appreciation to the Deanship of Scientific Research at King Saud University for funding the work through the research group project no. RGP-VPP-106.

#### References

- [1] Y.-P. Fu and C.-H. Lin, "Fe/Sr ratio effect on magnetic properties of strontium ferrite powders synthesized by microwave-induced combustion process," *Journal of Alloys and Compounds*, vol. 386, no. 1-2, pp. 222–227, 2005.
- [2] Z. Ullah, S. Atiq, and S. Naseem, "Influence of Pb doping on structural, electrical and magnetic properties of Sr-hexaferrites," *Journal of Alloys and Compounds*, vol. 555, pp. 263–267, 2013.
- [3] I. V. Zavislyak, M. A. Popov, and G. Srinivasan, "A cut-off millimeter wave resonator technique for mapping magnetic parameters in hexagonal ferrites," *Measurement Science and Technology*, vol. 20, no. 11, Article ID 115704, 2009.
- [4] S. Hussain and A. Maqsood, "Structural and electrical properties of Pb-doped Sr-hexa ferrites," *Journal of Alloys and Compounds*, vol. 466, no. 1-2, pp. 293–298, 2008.
- [5] S.-D. Kim and J.-S. Kim, "Magnetic properties of Sr-ferrites synthesized in molten (NaCl + KCl) flux," *Journal of Magnetism and Magnetic Materials*, vol. 307, no. 2, pp. 295–300, 2006.
- [6] S. Hussain and A. Maqsood, "Thermal transport properties of silica added Sr-hexa ferrites as a function of temperature," *Materials Letters*, vol. 62, no. 6-7, pp. 1002–1005, 2008.
- [7] L. You, L. Qiao, J. Zheng, M. Jiang, L. Jiang, and J. Sheng, "Magnetic properties of La-Zn substituted Sr-hexaferrites by self-propagation high-temperature synthesis," *Journal of Rare Earths*, vol. 26, no. 1, pp. 81–84, 2008.
- [8] M. J. Iqbal and S. Farooq, "Extraordinary role of Ce-Ni elements on the electrical and magnetic properties of Sr-Ba M-type hexaferrites," *Materials Research Bulletin*, vol. 44, no. 11, pp. 2050–2055, 2009.
- [9] C. M. Fang, F. Kools, R. Metselaar, G. De With, and R. A. De Groot, "Magnetic and electronic properties of strontium hexaferrite  $\text{SrFe}_{12}\text{O}_{19}$  from first-principles calculations," *Journal of Physics Condensed Matter*, vol. 15, no. 36, pp. 6229–6237, 2003.
- [10] B. D. Cullity, *Elements of X-Ray Diffraction*, Addison-Wesley, 2nd edition, 1978.
- [11] R. M. Garcia, E. R. Ruiz, and E. E. Rams, "Structural characterization of low temperature synthesized  $\text{SrFe}_{12}\text{O}_{19}$ ," *Materials Letters*, vol. 50, no. 2-3, pp. 183–187, 2001.
- [12] J. Smit and H. P. J. Wijn, *Ferrites*, John Wiley & Sons, New York, NY, USA, 1959.
- [13] X. Yang, Q. Li, J. Zhao, B. Li, and Y. Wang, "Preparation and magnetic properties of controllable-morphologies nano- $\text{SrFe}_{12}\text{O}_{19}$  particles prepared by sol-gel self-propagation synthesis," *Journal of Alloys and Compounds*, vol. 475, no. 1-2, pp. 312–315, 2009.
- [14] T. Xie, L. Xu, and C. Liu, "Synthesis and properties of composite magnetic material  $\text{SrCo}_x\text{Fe}_{12-x}\text{O}_{19}$  ( $x = 0-0.3$ )," *Powder Technology*, vol. 232, pp. 87–92, 2012.
- [15] S. Kong, P. Zhang, X. Wen et al., "Influence of surface modification of  $\text{SrFe}_{12}\text{O}_{19}$  particles with oleic acid on magnetic microsphere preparation," *Particuology*, vol. 6, no. 3, pp. 185–190, 2008.
- [16] M. Ahmad, R. Grossinger, M. Kriegisch, F. Kubel, and M. U. Rana, "Characterization of Sr-substituted W-type hexagonal ferrites synthesized by sol-gel autocombustion method," *Journal of Magnetism and Magnetic Materials*, vol. 332, pp. 137–145, 2013.
- [17] J. Xu, H. Zou, H. Li, G. Li, S. Gan, and G. Hong, "Influence of Nd<sup>3+</sup> substitution on the microstructure and electromagnetic properties of barium W-type hexaferrite," *Journal of Alloys and Compounds*, vol. 490, no. 1-2, pp. 552–556, 2010.
- [18] F. S. Jesus, A. M. Bolarin-Miro, C. A. Cortes-Escobedo, R. Valenzuela, and S. Ammar, "Mechanosynthesis, crystal structure and magnetic characterization of M-type  $\text{SrFe}_{12}\text{O}_{19}$ ," *Ceramics International*, vol. 40, no. 3, pp. 4033–4038, 2014.
- [19] S. Singhal, T. Namgyal, J. Singh, K. Chandra, and S. Bansal, "A comparative study on the magnetic properties of  $\text{MFe}_{12}\text{O}_{19}$  and  $\text{MAlFe}_{11}\text{O}_{19}$  ( $M = \text{Sr, Ba}$  and  $\text{Pb}$ ) hexaferrites with different morphologies," *Ceramics International*, vol. 37, no. 6, pp. 1833–1837, 2011.

- [20] M. J. Iqbal, M. N. Ashiq, P. Hernandez-Gomez, and J. M. Munoz, "Synthesis, physical, magnetic and electrical properties of Al-Ga substituted co-precipitated nanocrystalline strontium hexaferrite," *Journal of Magnetism and Magnetic Materials*, vol. 320, no. 6, pp. 881–886, 2008.
- [21] D. Y. Chen, Y. Y. Meng, D. C. Zeng, Z. W. Liu, H. Y. Yu, and X. C. Zhong, "CTAB-assisted low-temperature synthesis of SrFe<sub>12</sub>O<sub>19</sub> ultrathin hexagonal platelets and its formation mechanism," *Materials Letters*, vol. 76, pp. 84–86, 2012.
- [22] P. Weiss, "L'hypothèse du champ moléculaire et la propriété ferromagnétique," *Journal of Physics, Theory Applications*, vol. 6, no. 4, pp. 661–690, 1907.